Università degli Studi dell'Insubria

Department of Science and High Technology

Ph.D. Course in
Chemical and Environmental Sciences
XXXIV Cycle

Curriculum
Environmental Sciences

Ph.D. Thesis

# *Use of Remote Sensing techniques for monitoring the impacts of ground movements on structures and infrastructure*

Supervisor
*Prof. Alessandro Maria Michetti*

Co-Supervisor
*Dr. Olga Mavrouli*

Candidate
*Nicoletta Nappo*
*739472*

Academic Year 2020/2021

*We cannot teach people anything,*
*we can only help them discover it.*

*Galileo Galilei*

# Table of Contents

# List of Figures

Chapter 2

Chapter 3

Chapter 4

## Chapter 5

# List of Tables

Chapter 1

Chapter 2

Chapter 3

Chapter 4

Chapter 5

# Abstract

"*The substantial reduction of disaster risk and losses in lives, livelihoods and health and in the economic, physical, social, cultural and environmental assets of persons, businesses, communities and countries*" is the purpose of the Sendai Framework for Disaster Risk Reduction 2015-2030 adopted by the United Nations in March 2015 (UNDRR, 2021). The priority of the Sendai Framework is "*understanding disaster risk in all its dimensions of vulnerability, capacity, exposure of persons and assets, hazard characteristics and environment*" (UNDRR, 2021). Therefore, it is fundamental to prevent that (natural or anthropogenic) hazards of moderate intensity (e.g., subsidence, landslides) may turn into unforeseen disasters with severe consequences for the community.

In this perspective, this Ph.D. Thesis aims at investigating the impacts of ground movements originated from subsidence and landslides on (historic) buildings and road networks by using remote sensing techniques as satellite-based InSAR and UAV-based photogrammetry, thus enhancing the current knowledge about the cause-effect relationships between the considered hazards and building/road damage.

A standard framework for multi-scale monitoring of subsidence and analysis of related consequences on (historic) buildings is proposed here using multi-temporal and multi-platform InSAR data and local geological and stratigraphic setting. A large-scale multivariate regression model is adopted for mapping areas subjected to ground movements generated by subsidence, where a small-scale building vulnerability analysis can be then performed using damage records and InSAR-derived descriptors of building foundation motions due to subsidence. The proposed framework is applied to the city of Como (northern Italy), thus providing local Governments with an integrated tool for multi-scale monitoring of subsidence-affected areas and preserving the local architectural heritage.

Moreover, this research proposes a semi-automatic procedure combining UAV-based 3D and 2D photogrammetry products to characterize longitudinal and transverse cracks on asphalt road pavements in landslide-affected areas, and rate the road damage severity using quantitative descriptors of pavement quality, such as the International Roughness Index (IRI). This procedure is applied to two road sections selected within the Province of Como (northern Italy) to contribute to the landslide risk management of this territory.

Finally, the challenges arising from the use of remote sensing techniques, as satellite-based InSAR and UAV-based photogrammetry, for monitoring the impacts of subsidence and landslides respectively on buildings and road networks are discussed by presenting two additional case studies: a residential area in the city of Rome (Italy) affected by subsidence, and an asphalt-paved highway interchange in Panagia (Greece) subjected to landslide motions.

This research aims at supporting local Governments or road practitioners in the management of risks related to subsidence and landslides using remote sensing technologies, thus fostering the demand of safe and resilient constructions to mitigate (potential) disasters. The obtained results enhance our understanding of the cause-effect relationships between hazards and constructions (i.e., buildings and roads) and provide ready-to-use tools for building vulnerability analysis and road damage assessment.

The research activities were performed at the University of Insubria (Como, Italy) with secondments at the University of Twente (Enschede, The Netherlands) as part of the Erasmus for Traineeship Programme and the Horizon 2020 PANOPTIS Project (WP5) and at Sapienza University of Rome (Italy) as part of the DPC-ReLUIS 2019-2021 Project (WP6).

# 1. INTRODUCTION

In a changing environment, where disastrous events are becoming more frequent and devastating, it is fundamental to limit their impacts on society, thus preserving human lives, economies, cultural heritages, urban and natural environments.
Among other continents, Europe has been affected by a wide variety of disasters in recent years, such as wildfires (Portugal and Spain, 2017), the collapse of Ponte Morandi (Italy, 2018), the Notre-Dame de Paris fire (France, 2019), storm Gloria (Spain and France, 2020), Petrinja earthquake (Croatia, 2020), Gjerdrum landslide (Norway, 2020), Samos-Izmir earthquake (Greece and Turkey, 2020), South Moravia tornado (Czech Republic, 2021), and floods (e.g., Germany, Belgium, Netherlands, Italy, 2021) just to mention a few. The biggest disaster (in terms of human losses) seen in European history is the COVID-19 pandemic that killed more than a million people across the world, overwhelming national healthcare systems, disrupting public life and generating a major shock to economies (European Commission, 2021). Besides this exceptional circumstance, other geophysical, hydrological, meteorological and climatological events that hit the world in these years have reminded us of the importance of risk prevention and mitigation strategies. The European Environment Agency (EEA) estimated that about 63% of economic losses in the years 1980-2017 resulted from meteorological (e.g., storms) and hydrological events (e.g., floods and mass movements), while 85% of fatalities were caused by heatwaves (EEA, 2021).

During the 2015 Third United Nations (UN) World Conference on Disaster Risk Reduction (WCDRR), the UN General Assembly endorsed the Sendai Framework for Disaster Risk Reduction (2015-2030) that, in addition to the Paris Agreement on Climate Change and the Sustainable Development Goals among others, advocates for "*The substantial reduction of disaster risk and losses in lives, livelihoods and health and in the economic, physical, social, cultural and environmental assets of persons, businesses, communities and countries*" (UNDRR, 2021). "*The Sendai Framework defines four priorities: 1) Understanding disaster risk; 2) Strengthening disaster risk governance to manage disaster risk; 3) Investing in disaster*

*risk reduction for resilience; and 4) Enhancing disaster preparedness for effective response and to "Build Back Better" in recovery, rehabilitation and reconstruction*" (UNDRR, 2021).
A successful disaster management strategy is based on the application of risk reduction and prevention policies to mitigate existing risks, enhance the resistance and resilience of constructions and societies, reduce hazard-related losses, and prevent future disasters. To achieve these goals, prospective (i.e., to avoid the development of new risks), corrective (i.e., to remove or reduce already existing risks) and compensatory activities (i.e., to strengthen social and economic resilience) can be undertaken (UNDRR, 2021).
In this framework, disaster risk assessment is of fundamental importance to determine the nature and extent (in terms of location, intensity, frequency and probability) of the impacting hazard, assess the exposure and vulnerability (physical, social, economic or environmental) of the affected system, and evaluate the effectiveness of prevailing and alternative coping capacities to probable risk scenarios (UNDRR, 2021).

Hazards may be *natural* (when predominantly caused by natural processes), *anthropogenic* (when induced or influenced by human activities) or *socio-natural* (when derived by a combination of natural and anthropogenic factors) and can occur as single or multiple events eventually triggering additional cascading effects (UNDRR, 2021). The Sendai Framework differentiates five categories of hazards (i.e., biological, environmental, geological or geophysical, hydrometeorological and technological) based on the processes and phenomena that originate them. Geological or geophysical hazards encompass both internal earth activities (e.g., earthquakes, tectonic motions, volcanic emissions) and surficial ground movements (e.g., subsidence, landslides) of natural (e.g., land or slope instability) or anthropogenic origin (e.g., underground excavations, collapse of mineworks).

Subsidence is the lowering or sinking of the topographic surface (Galloway and Burbey, 2011) that can involve areas of various spatial distribution (at large or small-scale) evolving in different time frames (from few days to several years) with consequent variable velocity of movement (ISPRA, 2021). Natural factors that mainly trigger subsidence in lowland, coastal and delta areas are the soil sediment compaction due to lithostatic loads (e.g., D'Amico et al., 2020; Del Ventisette et al., 2015) and the variations of the groundwater level (e.g., Botey i Bassols et al., 2021; Bozzano et al., 2015; Galloway and Burbey, 2011). Soils composed of continuous layers of compressible fine-grained material with (organic) clay and peat are prone to subside because characterized by high compressibility in both primary and secondary consolidation stages (Den Haan and Kruse, 2006; Nicodemo et al., 2020; Peduto et al., 2017c; Stramondo et al., 2008). Anthropogenic activities, such as groundwater overexploitation (e.g., de Wit et al., 2021; Herrera et al., 2009; Tosi et al., 2013), tunnelling (e.g., Antonielli et al., 2021; Kontogianni and Stiros, 2020; Milillo et al., 2018; Scoular et al., 2020) or extensive urbanization in susceptible areas (e.g., Rosi et al., 2016; Solari et al., 2016; Tosi et al., 2002), may further worsen the ground sinking. In urban areas, subsidence often derives from the combination of both natural and anthropogenic causes (e.g., Ferrario et al., 2015a; Mohamadi et al., 2019; Nappo et al., 2020; Pratesi et al., 2016; Solari et al., 2016).

Landslides are defined as "*the movement of a mass of rock, debris or earth along a slope*" (Cruden, 1991) occurring under the primary effect of gravitational forces. Other terms, such as *slope movement, mass movement* and *mass wasting*, are sometimes adopted in literature to describe "*denudational processes whereby soil or rock is displaced along the slope*" (van Westen, 1993). However, *landslide* is the most widely accepted term. Common triggers of slope movements are intense rainfall (e.g., Dai and Lee, 2001; Guzzetti et al., 2007; Segoni et al., 2018), rapid snowmelt (e.g., Kawagoe et al., 2009; Krogli et al., 2018; Naudet et al., 2008), variations in the groundwater content (e.g., Cascini et al., 2010a; Corominas et al., 2005; van Asch et al., 2009), seismic activity (e.g., Keefer, 2002; Martino and Scarascia Mugnozza, 2005; Tanyas et al., 2017; Valagussa et al., 2018; Yin et al., 2009; Zhang et al., 2019), volcanic activity (e.g., Ancochea et al., 2010; Crosta et al., 2005; Hurlimann et al., 2000), anthropogenic modifications (e.g., Jaboyedoff et al., 2016; Jones et al., 2021) or any combination of these factors (Schster and Wieczorek, 2002). Given their complexity, various landslide classification methods have been proposed over time based on the mechanics of movement, type of material, presence of water/ice in the soil, speed of movement, triggering mechanisms and state of activity (e.g., Blong, 1973; Cruden and Varnes, 1996; Hungr et al., 2014; Hutchinson, 1988; Skempton, 1953; Varnes, 1978). To the present day, the classification system proposed by Varnes (1978), then revised by Cruden and Varnes (1996) and Hungr et al. (2014), is still the most adopted. This system (Tab. 1.1) classifies the landslides according to the mechanism of movement, material involved, state of activity and velocity of movement.

***Table 1.1.*** *Landslide classification proposed by Varnes et al. (1978) and modified by Cruden and Varnes (1996) and Hungr et al. (2014).*

| Mechanism of movement | Material | State of activity | | Velocity of movement | |
|---|---|---|---|---|---|
| Fall | Rock | Active | | Extremely rapid | > 5 m/sec |
| Topple | Debris | Reactivated | | Very rapid | > 3 m/min |
| Rotational slide | Earth | Suspended | | Rapid | > 1.8 m/hr |
| Translational slide | | Inactive | Dormant | Moderate | > 13 m/month |
| Spread | | | Abandoned | Slow | > 1.6 m/year |
| Flow | | | Stabilized | Very slow | > 16 mm/year |
| Complex | | | Relict | Extremely slow | < 16 mm/year |

When structures (e.g., buildings) and infrastructures (e.g., roads, railways, pipelines) are built in areas affected by subsidence or landslides, either at large or small scale, they may suffer from vertical (absolute or differential) settlements, horizontal movements and relative rotations at their foundation depth causing damage of various severity on the superstructure (Bjerrum, 1967, 1963; Boscardin and Cording, 1989; Burland et al., 1977; Burland and Wroth, 1974; Skempton and MacDonald, 1956). Therefore, the assessment of consequences as part of vulnerability analysis of (infra)structures exposed to subsidence or landslides is of primary importance to understand the risk (potentially) affecting a community and support governments in strengthening prevention and mitigation measures (Fell et al., 2008). Performing such analysis requires a good knowledge of i) the geological setting of the investigated area, ii) the geometric characteristics and damage severity of the affected construction, and iii) the rate of movement experienced by the construction during the monitoring time frame.

During the last decades, diverse remote sensing techniques based on space- or air-borne platforms have been adopted to monitor (infra)structures subjected to subsidence and/or landslides, thus overcoming the spatial and temporal limitations of traditional monitoring practices (e.g., GNSS, geodetic levelling, inclinometers). These systems can indeed rapidly examine large areas at affordable costs and acquire precise data with sub-centimetric accuracy (e.g., Lissak et al., 2020; Niethammer et al., 2012; Nex and Remondino, 2014; Wasowski and Bovenga, 2014).

Space-borne Interferometric Synthetic Aperture Radar (InSAR) techniques can be applied to reconstruct the deformation pattern of buildings (e.g., Bianchini et al., 2015; Borrelli et al., 2018; Ezquerro et al., 2020; Herrera et al., 2010; Nicodemo et al., 2020; Peduto et al., 2015, 2017a, 2017c, 2019), bridges (e.g., Peduto et al., 2018; Ponzo et al., 2021), roads (e.g., Bozzano et al., 2018; Ferlisi et al., 2020a; Nappo et al., 2019) and railway embankments (e.g., Peduto et al., 2017b) affected by subsidence or landslides. Archive SAR images are available at high resolution (in C-band) from dismissed (e.g., ERS 1&2, Envisat, Radarsat 1) or currently operative missions (e.g., Sentinel-1, Radarsat 2), and at very high resolution (in X-band) from other satellite constellations (e.g., Cosmo-SkyMed, TerraSAR-X) spanning a time frame of almost 30 years.

Air-borne Unmanned Aerial Vehicles (UAV) have been introduced in recent years to capture high resolution RGB, thermal or infrared images of selected targets in the nadir or oblique directions (Giordan et al., 2020; Nex and Remondino, 2014; Remondino et al., 2017). RGB images are then matched to reconstruct photogrammetric 3D point cloud models via Structure from Motion (SfM) algorithm, and used to monitor slope instabilities (e.g., Cardenal et al., 2019; Fazio et al., 2019; Gomez and Purdie, 2016; Mayr et al., 2018; Stumpf et al., 2013), assess post-disaster building damage (e.g., Cusicanqui et al., 2018; Duarte et al., 2017; Fernandez Galarreta et al., 2015; Giordan et al., 2018; Nex et al., 2019; Vacca et al., 2017), and more recently detect distress on road pavements (e.g., Inzerillo et al., 2018; Saad and Tahar, 2019; Tan and Li, 2019).

## 1.1 Objectives of the research

The present Ph.D. Thesis develops from the necessity of "*understanding disaster risk in all its dimensions of vulnerability, capacity, exposure of persons and assets, hazard characteristics and environment*" (Sendai Framework - UNDRR, 2021). Therefore, it is fundamental to prevent that (natural or anthropogenic) hazards of moderate intensity (e.g., subsidence, landslides) may turn into unforeseen disasters with severe consequences for the community.

In this perspective, remote sensing techniques as satellite-based InSAR and UAV-based photogrammetry are applied in this research to assess the impacts of ground movements originated from subsidence and landslides on (historic) buildings and road networks, thus enhancing the current knowledge about the cause-effect relationships between the considered hazards and building/road damage. Standard and semi-automatic procedures using InSAR and UAV-based photogrammetry techniques are refined or established for routine monitoring of (infra)structures in vulnerable areas. The objective is facilitating the adoption of advanced technologies for local Governments to strengthen the management of risks related to subsidence and landslides impacting on urban areas and road infrastructure, thus fostering prevention and mitigation measures at different scales of analysis.

This research specifically covers two topics: i) the use of InSAR for multi-scale monitoring of subsidence in urban areas, and ii) the use of UAV for detection and classification of landslide-induced damage on asphalt-paved roads.

### 1.1.1 InSAR for multi-scale monitoring of subsidence in urban areas

Although InSAR techniques are widely applied in subsidence studies (for an overview, see Solari et al., 2018; Tomàs et al., 2014), standard procedures embedding such technology to manage the subsidence risk in urban areas are still limited (e.g., Peduto et al., 2015). This research aims at filling this gap by proposing a framework for the multi-scale monitoring of subsidence and analysis of related consequences on (historic) buildings based on the joint use of multi-temporal and multi-platform InSAR data and local geological and stratigraphic setting. The main contribution is the preliminary investigation at large scale of the correlations between subsidence predisposing factors (e.g., compressible soil layers, groundwater level) and InSAR-derived ground measurements, thus determining the areas where the observed movements could be likely attributed to subsidence (Nappo et al., 2020). Unlikely previous works that adopted thresholds on the InSAR velocity or displacement records to discretize stable from unstable areas (e.g., Ezquerro et al., 2020; Peduto et al., 2015, 2017c), a multivariate regression model is used in this research to interpret the spatial pattern of subsidence at large scale. This step allows determining areas where small scale vulnerability analyses of (historic) buildings can be then performed using all InSAR records (i.e., without prior thresholding of the data) to measure subsidence-induced displacements (Nappo et al., 2021a).

The proposed framework is applied to the city of Como (northern Italy) at large and small scale, thus providing local Governments with an integrated tool for monitoring subsidence-affected areas (Nappo et al., 2020) and preserving the local architectural heritage (Nappo et al., 2021a).

### 1.1.2 UAV for road damage detection and classification in landslide areas

Vulnerability analyses of road networks subjected to landslides are still limited. They usually adopt visual inspections to assess the road pavement condition (e.g., Ragnoli et al., 2018) and rate the severity of pavement damage in levels based on the intensity of the impacting hazard (e.g., velocity, differential displacement) (e.g., Ferlisi et al., 2020a; Mavrouli et al., 2019; Nappo et al., 2019). Although pavement distress catalogues (e.g., AASHO, 1962; ANAS, 2004; ASTM, 2020) describe the typologies and common causes of damage on asphalt road pavements, they do not recommend any numerical proxy for distress characterization or severity classification (Inzerillo et al., 2018; Ragnoli et al., 2018). Quantitative indicators based on the pavement roughness, skid resistance and bearing capacity are only used for the routine assessment of road pavement quality in the framework of Pavement Management System (PMS) (e.g., George et al., 1989; Tan and Li, 2019), but they are not adopted for damage severity classification in road vulnerability analyses. Therefore, methods to quantitatively detect and classify the extent and severity of landslide-induced damage on asphalt-paved roads are still lacking. To this aim, this research proposes a semi-automatic procedure combining UAV-based 3D and 2D photogrammetry products to characterize longitudinal and transverse cracks on asphalt road pavements in landslide-affected areas, and rate the road damage severity using quantitative descriptors of pavement quality, such as the International Roughness Index (IRI) (Nappo et al., 2021b). The objective is assisting road maintenance agencies to rapidly and safely inspect road infrastructure exposed to landslides. The proposed procedure is applied to two road sections selected in the Province of Como (northern Italy), thus contributing to the landslide risk management of this territory (Nappo et al., 2021b).

## 1.2 Development of the research

The research presented in this Ph.D. Thesis was performed at the University of Insubria (Como, Italy) with secondments at the University of Twente (Enschede, The Netherlands) as part of the Erasmus for Traineeship Programme and the Horizon 2020 PANOPTIS Project (WP5) and at Sapienza University of Rome (Italy) as part of the DPC-ReLUIS 2019-2021 Project (WP6).

## 1.3 Structure of the Thesis

This Ph.D. Thesis is organised as follows.

*Chapter 1* introduces the Thesis illustrating the objectives and development of the research.

*Chapter 2* provides a theoretical background on remote sensing techniques, InSAR and UAV, then recalls the fundamentals of vulnerability analysis, and finally reviews the current practices in the assessment of buildings and road damage in areas respectively subjected to subsidence and landslides.

*Chapter 3* presents the framework for the multi-scale monitoring of subsidence and analysis of related consequences on (historic) buildings based on the use of multi-platform InSAR data with specific application to the city of Como (N Italy).

*Chapter 4* illustrates the semi-automatic procedure combining UAV-based 3D and 2D photogrammetry products to detect and classify longitudinal and transverse cracks on asphalt road pavements in landslide-affected areas, here tested for the Province of Como (N Italy).

*Chapter 5* discusses the challenges in i) using InSAR measurements for monitoring buildings affected by subsidence in Rome (Italy), and ii) applying UAV-based products to detect road pavement distress on strategic infrastructure affected by landslides in Panagia (Greece).

*Chapter 6* concludes this Thesis by discussing the achieved objectives and future perspectives.

The contents presented in Chapters 3 and 4 have been published in *Remote Sensing* – MDPI, *International Journal of Disaster Risk Reduction* and *Engineering Geology* international journals. The contents of Chapter 5 are partially based on a manuscript (in preparation) to be submitted to *Sustainability* – MDPI, and partially on the *Linee guida per l'utilizzo dei dati interferometrici satellitari ai fini dell'interpretazione del comportamento strutturale delle costruzioni* (DPC-ReLUIS, 2021) to which the author contributed.

# 2. USE OF INSAR AND UAV FOR CONSEQUENCE ANALYSIS: A LITERATURE REVIEW

The analysis of consequences induced on (infra)structures by ground movements originated from subsidence and landslides is a fundamental step of disaster risk management (Fell et al., 2008). It comprises i) the collection of information about the investigated (infra)structure, the affecting hazard and the geological setting of the area (Remondo et al., 2005; van Westen et al., 2004), and ii) the assessment of the physical vulnerability of exposed constructions and their repair/replacement cost (e.g., Ferlisi et al., 2020a; Mavrouli et al., 2019; Nappo et al., 2019; Peduto et al., 2017a).

The geometry, construction material, foundation type, loads, and age of the analysed (infra)structures can be derived from archive data (e.g., cartographic data, original construction projects) or web repositories. Field investigations are essential to assess the damage pattern and maintenance status of the construction, and collect material to retrieve hydrogeological, geotechnical and stratigraphic information, in case they are not available from previous campaigns. The intensity of the affecting hazard can be described as its destructiveness (e.g., volume, kinetic energy, velocity, total or differential displacement) depending on the typology of occurring event (e.g., Corominas et al., 2014; Fell et al., 2008).

The movements generated by subsidence and landslides can be monitored via traditional systems (e.g., GNSS, borehole extensometers, inclinometers, geodetic levelling, tiltmeter) that provide precise and reliable measurement of the ground motion (e.g., Baldi et al., 2009; Bitelli et al., 2020; Hu et al., 2019; Uhlemann et al., 2016; Wang et al., 2015), but are expensive and difficult to install in wide regions (Solari et al., 2018). To overcome such limitations, space-borne and air-borne remote sensing techniques, such as InSAR and UAV-based photogrammetry, can be alternatively adopted to monitor (infra)structures affected by subsidence or landslides (e.g., Giordan et al., 2020; Lissak et al., 2020; Raspini et al., 2017; Tomàs et al., 2014; Wasowski and Bovenga, 2014).

Taking advantage from the InSAR capability of collecting precise measurements of ground surface movements at large and small scale in long time frames, these techniques are nowadays largely implied for monitoring land subsidence (e.g., Bèjar-Pizarro et al., 2016; Bozzano et al., 2018; Cigna et al., 2012; Del Ventisette et al., 2013, 2015; Herrera et al., 2009; Pratesi et al., 2016; Solari et al., 2016; Stramondo et al., 2008) and its effects on (historic) buildings (e.g., Bru et al., 2013; Ferlisi et al., 2020b; Herrera et al., 2010; Karila et al., 2013; Nicodemo et al., 2020; Peduto et al., 2017c). To the author's knowledge, few multi-scale frameworks for subsidence monitoring have been proposed adopting InSAR data (e.g., Ezquerro et al., 2020; Peduto et al., 2015), and none of them suggested the use of multivariate regression models for zoning subsidence-affected urban areas.

Although InSAR techniques could be used also for vulnerability analyses of road networks exposed to landslides (e.g., Ferlisi et al., 2020a; Nappo et al., 2019), these studies lack in a quantitative description of the road pavement damage. Attempts to automatically detect distress on asphalt-paved roads using computer vision algorithms and UAV-based products have been emerging in recent years (e.g., Inzerillo et al., 2018; Saad and Tahar, 2019; Tan and Li, 2019), but these studies still do not characterize or rate the severity of road pavement damage induced by landslides.

After briefly recalling what remote sensing techniques are (Section 2.1), this Chapter reviews the fundamentals of InSAR (Section 2.2) and UAV (Section 2.3). Then, methods for subsidence and landslide vulnerability analysis are summarised in Section 2.4. Building damageability criteria adopted in subsidence vulnerability analyses are reported in Section 2.5. Road damage typologies, their severity classification in landslide studies and methodologies for pavement quality assessment and damage detection are reviewed in Section 2.6.

## 2.1 Remote sensing techniques

"*Remote sensing is the process of acquiring information about objects or areas from a distance without making physical contact with the target, typically from aircraft or satellites*" (NASA, 2021; NOAA, 2021). Depending on the type of remote sensor, these instruments can record reflected and/or emitted electromagnetic energy (i.e., waves) with different wavelengths and frequencies (ESA, 2021; NASA, 2021). Sensors that operate with their own source of energy are defined as *active* and usually operate in the microwave band of the electromagnetic spectrum, such as radars, altimeters and scatterometers (ESA, 2021; NASA, 2021). When they rely on a natural source of energy (e.g., the Sun) bounced by the target, the remote sensors are defined as *passive*; these sensors usually operate in the visible, infrared and thermal infrared bands of the electromagnetic spectrum (ESA, 2021; NASA, 2021).

Figure 2.1 shows the difference between satellites' active sensors (e.g., radar) that can acquire data in all-weather and night-and-day conditions, and passive sensors (e.g., optical) that depend on the weather and sunlight.

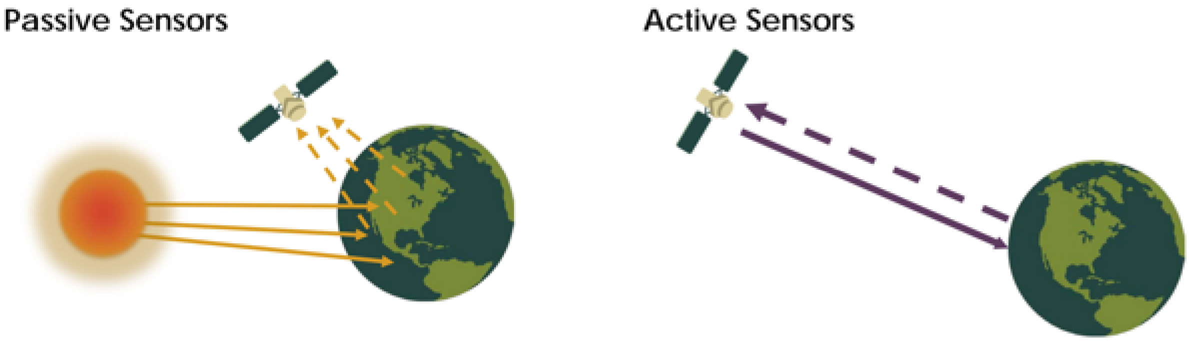

***Figure 2.1.*** *Schematic diagram of active and passive sensors mounted on satellites (credits: NASA Applied Remote Sensing Training Program; source: NASA, 2021).*

## 2.2 Fundamentals of InSAR

This Section presents the basic concepts of Synthetic Aperture Radar (SAR) data and the available satellites carrying SAR sensors. Then, the principles of Interferometric Synthetic Aperture Radar (InSAR) techniques and processing algorithms are briefly summarised.

### 2.2.1 SAR systems

A *Synthetic Aperture Radar* (SAR) is an active radar sensor typically mounted on aircrafts or spacecrafts that emits an electromagnetic signal (i.e., pulse) in the microwave spectrum. The pulse is sent towards a target that, according to its reflectivity and constitutive material, absorbs or reflects the signal. The backscattered pulse is then received by the radar sensor and converted into a SAR image. The advantage of these systems is the capability of acquiring images almost globally, independently from an external illumination source, as the Sun, and in any weather condition (Bamler et al., 1998; Franceschetti and Lanari, 1999).

The SAR sensors adopted for monitoring the Earth's surface are mounted on satellites moving along a near-polar orbit at an altitude ranging from 500 to 800 km above the Earth's surface. The trajectory from north to south pole is called *ascending orbit*, while that from south to north is called *descending orbit*. While orbiting around the globe, the SAR sensor illuminates an area on the Earth's surface called *antenna footprint* in *azimuth* (i.e., x coordinate) and *range* (i.e., y coordinate) SAR reference system (Fig. 2.2). The pulses are sent along the radar beam's *line of sight* (LOS) in *L-band* (1-2 GHz, ~24 cm wavelength), *C-band* (5-6 GHz, ~6 cm wavelength) and *X-band* (8-12 GHz, ~3 cm wavelength) (Mosconi et al., 2010). When the pulse is backscattered to the sensor, it carries *amplitude* and *phase* information. The amplitude is the energy of the microwave signal that may differ for the emitted and backscattered pulses, depending on the material properties of the target. Typically, urban areas have strong backscattered radiations and are seen as bright pixels of the SAR image, while targets with low amplitude are seen as dark pixels (Ferretti et al., 2007). The phase is a parameter depending on the cyclicity of the electromagnetic signals represented by sinusoidal waves of period $(-\pi, +\pi)$. The phase difference between emitted and backscattered signals allows estimating the altitude or movement of the target (Ferretti et al., 2007).

The SAR images are acquired with an angle between the LOS and the nadir direction, called *incidence angle*, that varies in a range of 20-50° depending on the sensor. This acquisition geometry may induce distortions in the SAR image, called *foreshortening*, *layover*, and *shadowing* (Franceschetti and Lanari, 1999). Foreshortening generates when the terrain slope is close to the incidence angle, almost perpendicular to the LOS, so that a SAR pixel represents a larger area than other pixels. When the terrain slope exceeds the incidence angle, signals from different targets are overlaid and summed, thus generating the layover effect. Finally, the shadowing effects are due to areas not illuminated by the radar pulse.

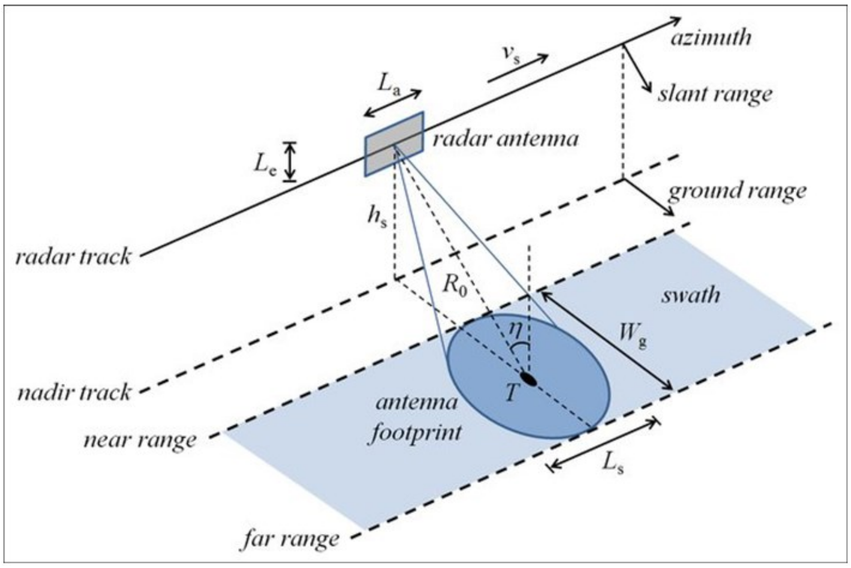

***Figure 2.2.*** *Schematic illustration of the SAR acquisition geometry (modified from Martone, 2019).*

Several satellites carrying SAR sensors are available nowadays, either for historical analyses or real-time monitoring. They differ in the frequency of emitted signal (i.e., X-band, C-band and L-band), the size of illuminated scene (i.e., swath) and the revisiting time (i.e., the number of days between two acquisitions).

### 2.2.2 SAR Interferometry

The standard Interferometric Synthetic Aperture Radar (InSAR) technique exploits the phase difference between two SAR acquisitions over the same area and with slightly different positions of the satellite carrying the sensor to extract distance information about Earth's topography (ESA, 2021).

By co-registering two SAR images, the phase variations between $-\pi$ to $+\pi$ can be converted into an *interferogram* where *fringes* represent the signal changes of a certain area (ESA, 2021; TRE-Altamira, 2021). Interferometric fringes depend on the *coherence* of the interferogram indicating the similarity of the radar signal between SAR images and ranging between 0 (no similarity) and 1 (same phase). Sources of decorrelation (i.e., low coherence) are typically vegetation, construction sites, erosion and rapid movements (Ferretti et al., 2007). To extract the interferometric phase ($\Delta\varphi$) from an interferogram, discontinuities need to be removed via phase unwrapping algorithms (Constantini, 1998).

The interferometric phase ($\Delta\varphi$) can be expressed as the sum of four contributions: topography, atmosphere, target displacement and decorrelation effects. Assuming that the decorrelation effects are negligible and knowing the interferometric phase, the target displacement maps are obtained by subtracting the topographic and atmospheric contributions, respectively computed from a Digital Terrain Model (DTM) and weather forecast (Ferretti et al., 2007). This approach is called Differential Interferometry (DInSAR).

The single interferogram approach constrains the detection of displacements in the specific time frame between the two considered SAR acquisitions. To estimate the displacements over longer periods, advanced interferometric (A-DInSAR) techniques exploiting stacks of SAR images have been developed. The first method, called Permanent Scatterers Interferometry (PSInSAR)[1], was introduced in 1999 (Ferretti et al., 2000, 2001). By generating multiple interferograms from a stack of (about 20-25) SAR images, coherent radar targets, called

---

[1] The terms Permanent Scatterer and Permanent Scatterer Interferometry (PSInSAR) are patented by the Polytechnic University of Milan (POLIMI, Italy).

Permanent Scatterers (Ferretti et al., 2001) because of their high reflectivity and phase stability, can be identified over the entire observation period, thus obtaining ground deformation time series measuring displacements with millimetric accuracy (Ferretti et al., 2001). Typical objects with good reflectivity and stable signal, called Persistent Scatterers (PS), are buildings, metallic objects, pylons, antennae and exposed rocks (Fig. 2.3). Other A-DInSAR techniques for PS detection are the Interferometric Point Target Analysis (IPTA; Werner et al., 2003), the Stanford Method for Persistent Scatterers (StaMPS; Hooper et al., 2004, 2008, 2012), and the Persistent Scatterer Pairs (PSP-DIFSAR; Costantini et al., 2008, 2009).

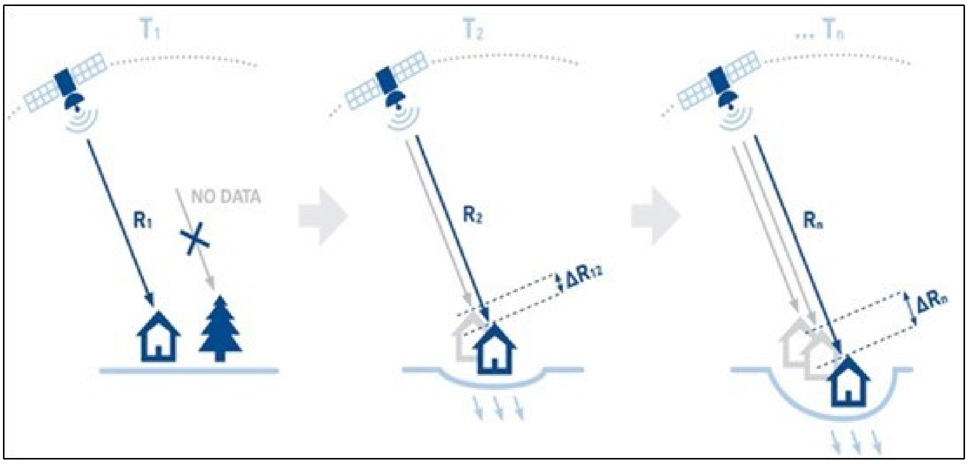

***Figure 2.3.*** *Schematic InSAR data acquisition on Persistent Scatterers (source: TRE-Altamira, 2021).*

To improve the capability of InSAR in detecting deformations in non-cultivated or desert areas with moderate coherence due to low reflectivity, techniques to identify spatially Distributed Scatterers (DS) have been developed. The Small BAseline Subset (SBAS) approach (Berardino et al., 2002) is based on the combination of several interferograms obtained from SAR images acquired with small spatial and temporal baselines (i.e., with small differences between acquisition geometries and short revisiting times). The SBAS algorithm allows to minimise the decorrelation effects and maximise the number of coherent targets per pixel, thus obtaining the deformation pattern of large areas with accuracy of 1-2 mm/year on the target velocity. The SqueeSAR algorithm (Ferretti et al., 2011) is an advancement of the PSInSAR and is based on the simultaneous identification of Permanent and Distributed Scatterers.

For a review of InSAR processing techniques, please refer to Crosetto et al. (2016), Pepe and Calò (2017), and Ho Tong Minh et al. (2020).

### 2.2.3 InSAR products

The A-DInSAR processing algorithms reconstruct the deformation history of a set of sparse points (Fig. 2.4), named Persistent Scatterers (PS) or Point Targets (PT), that depends temporally on the first acquired image and is, therefore, referred to a specific time interval. The measures are also spatially relative to a reference point, which is usually chosen in a stable area (e.g., on bedrock) to reduce the decorrelation effects that may influence the quality of the results. For each PS, its displacement time series along the sensor's line of sight (LOS), mean annual LOS velocity, geographic coordinates and height are provided. The quality of each measure is given by its coherence and standard deviation. Each PS represents an area on the Earth's surface of dimensions varying according to the spatial resolution of each sensor (e.g., 5x20 m for ERS 1&2 and Envisat, 3x3 m for Cosmo-SkyMed and 15x4 m for Sentinel-1).

To facilitate the post-processing of InSAR products in GIS software, the PS data are provided in form of a shapefile (.shp) and an ASCII text file to the end-users.

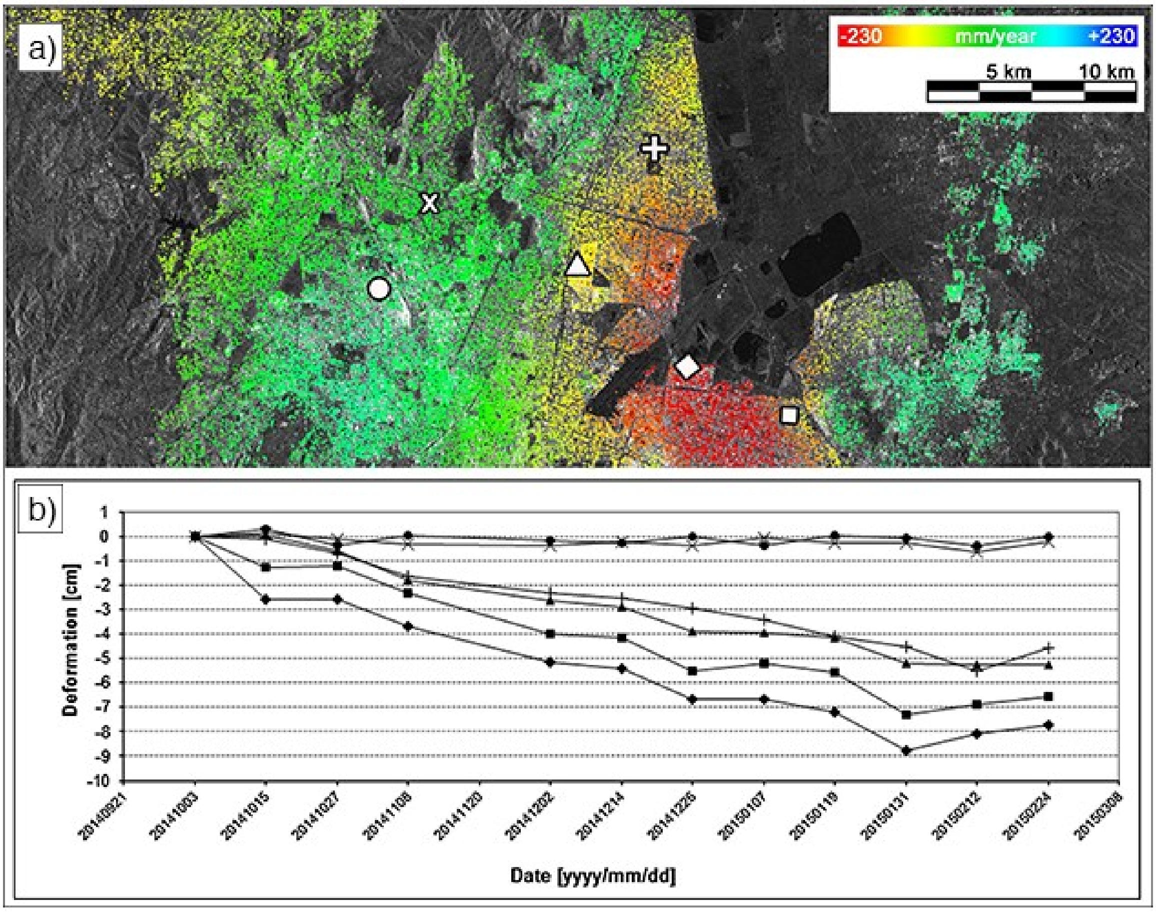

***Figure 2.4.*** *Example of a) LOS velocity map reconstructed from Sentinel-1 SAR images of Mexico City, and b) LOS displacement time series of six PS (modified from Crosetto et al., 2016).*

## 2.3 Unmanned Aerial Vehicles (UAV)

Unmanned Aerial Vehicles (UAV), commonly also called drones, are aircrafts carrying their payload, sensors, navigation and power systems that can be operated remotely by a human pilot or autonomously by an onboard computer (Giordan et al., 2020; Nex and Remondino, 2014). These aircrafts can be equipped with RGB digital, multispectral or thermal cameras and LiDAR sensors operating in the nadir or oblique directions for rapid and low-cost data acquisitions over wide areas aimed at real-time condition assessment, routine monitoring and quick responses after natural and/or anthropic disasters (Giordan et al., 2020; Nex and Remondino, 2014; Schnebele et al., 2015; Stocker et al., 2017).

Fixed-wing, rotorcraft, and vertical take-off and landing (VTOL) aerial vehicles are currently available (Greenwood et al., 2019 – Fig. 2.5).

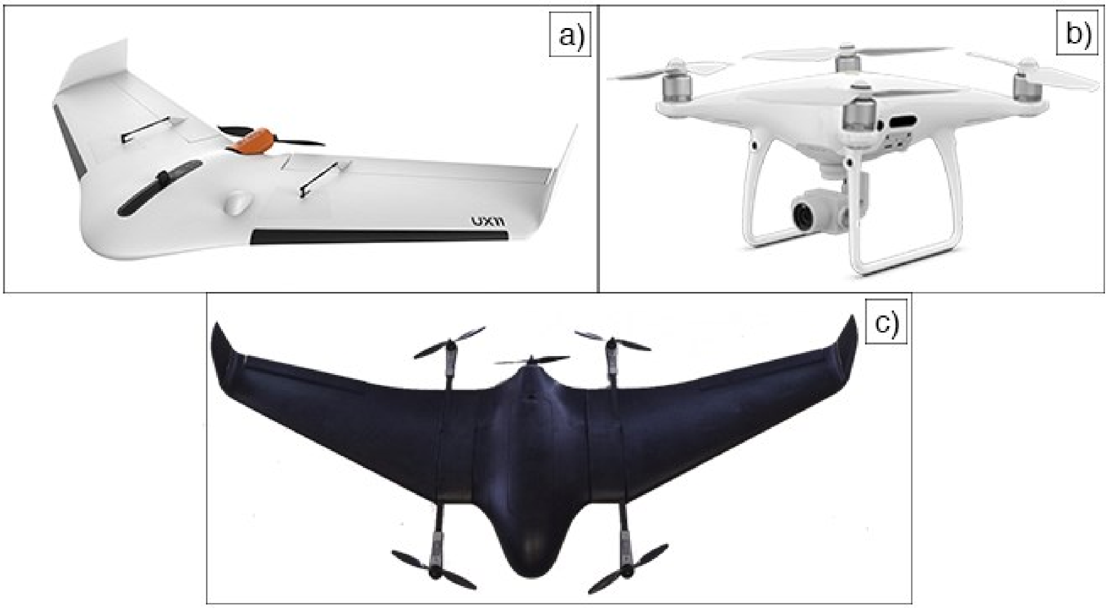

***Figure 2.5.*** *Examples of a) fixed-wing DelairUX11 (source: Delair, 2021), b) quadrotor DJI Phantom 4 Pro V2.0 (source: DJI, 2021) and c) VTOL Delta-quad Pro (source: Vertical Technologies, 2021).*

Fixed-wing UAV (e.g., Fig. 2.5a) resemble traditional aircrafts and can rapidly cover long distances, thus rendering them suitable for mapping applications (Greenwood et al., 2019). Multirotor UAV (e.g., Fig. 2.5b) have rotating propellers attached to their body assuring steadiness and flexibility in movements, thus being ideal for precise and close-range surveying of complex 3D features (Greenwood et al., 2019). VTOL aircrafts (e.g., Fig. 2.5c) can be considered as a combination between fixed-wing and multirotor UAV (Byun et al., 2016;

Ozdemir et al., 2014) taking off and landing vertically and flying horizontally, thus acquiring information of both vertical and horizontal objects. Fixed-wing and multirotor UAV are preferred for their relatively low cost, operating capabilities in different environments and transportability due to their weight generally being below 30 kg (Giordan et al., 2020).

Crucial for the correct application of UAV-based products is the flight and data acquisition planning, which depends on the technical characteristics of the sensor mounted on the UAV (e.g., focal length, ISO range and image size of the camera), the operational capability of the aircraft (e.g., duration of the battery, max speed, positioning accuracy, maximum distance from the ground control station, operating temperature range) and the surveyed target (Giordan et al., 2020; Nex and Remondino, 2014).

Finally, national and/or international regulations apply for the safe use of UAV that may require insurance coverage, Permission for Commercial Operations (PfCO) and Private Impact Assessment (PIA) among others (ICAO, 2021; ENAC, 2021; Stocker et al., 2017).

## 2.4 Vulnerability analysis

The vulnerability of (infra)structures to natural hazards can be quantitatively represented by fragility and/or vulnerability curves. The construction typology, damage pattern and hazard intensity parameter are necessary input data to derive such curves (Saeidi et al., 2009, 2013). Fragility curves are used to express the physical vulnerability of a construction system in probabilistic terms (Mavrouli et al., 2014; Peduto et al., 2017a). They express the conditional probability of reaching or exceeding a specific level of damage severity as a function of the hazard intensity measure (IM) (e.g., Ferlisi et al., 2020a, 2020b; Fotopoulou and Pitilakis, 2013; Mavrouli et al., 2014; Nappo et al., 2021a; Negulescu and Foerster, 2010; Negulescu et al., 2014; Peduto et al., 2017a, 2018; Saeidi et al., 2009, 2013; Wiebe and Cox, 2014), and are computed as:

$$(2.1) \quad P(Damage \geq D_i) = \Phi\left[\frac{1}{\beta} ln\left(\frac{IM}{\overline{IM}}\right)\right]$$

where $D_i$ is the level of damage severity, Φ is the standard normal cumulative distribution function, β and $\overline{IM}$ are respectively the dispersion and the median of the IM for each $D_i$.

The vulnerability curves express the relationship between average severity of (infra)structure damage and the hazard intensity measure (IM) on a scale between 0 (no loss) and 1 (total loss)

(Budetta et al., 2016; Corominas et al., 2014; Ferlisi et al., 2020a; Galli and Guzzetti, 2007; Mavrouli et al., 2014; Peduto et al., 2017a, 2018; Saeidi et al., 2009; van Westen, 2013; Winter et al., 2016). According to Lagomarsino and Giovinazzi (2006), these curves can be computed as:

$$\mu_D = c_1[c_2 + tanh(c_3 \cdot IM + c_4)] \tag{2.2}$$

where $\mu_D$ is the average damage severity, $tanh$ is the tangent of the hyperbolic regression function, and $c_{(1,2,3,4)}$ are coefficients determined from the regression model.

## 2.5 Building damage assessment in subsidence-affected areas

Ground movements originated by subsidence can induce absolute and/or differential settlements, angular distortions and relative rotations to the foundation system of a building that may result in damage on the superstructure, when the foundation cannot accommodate such movements (Bjerrum, 1963,1967; Boscardin and Cording, 1989; Burland and Wroth, 1974; Burland et al., 1977; Skempton and MacDonald, 1956).

The damage observed on the superstructure is related to the intrinsic building characteristics (e.g., construction material, foundation typology, age) and the hazard intensity (e.g., Ferlisi et al., 2020a; Nappo et al., 2021a; Peduto et al., 2017a, 2017c; Saeidi et al., 2009, 2013). The severity of damage can be evaluated via analytical methods, based for instance on the (elastic) beam theory modelling the global behaviour of a building (Boscardin and Cording, 1998; Burland and Wroth, 1974; Timoshenko, 1957), or empirical methods derived from the assessment of damage patterns on a consistent number of sample buildings (e.g., Burland and Wroth, 1974; Saeidi et al., 2009; Zhang and Ng, 2005).

The typology and severity of building damage can be evaluated via visual in situ inspections of structural and non-structural elements. Subsidence typically causes (almost) vertical, oblique and arc-shaped cracks (Bjerrum, 1963, 1967; Boscardin and Cording, 1989; Burland and Wroth, 1974; Burland et al., 1977; Skempton and MacDonald, 1956). The pattern of these fractures depends on the construction typology (i.e., concrete, masonry or stones), the foundation system (i.e., shallow or piles), the affected element (e.g., pillars, walls, beams, etc.), and the finishing (e.g., with or without plaster) (e.g., Nappo et al., 2021a; Nicodemo et al., 2017; Peduto et al., 2017c, 2019). For each building, the typology, geometry (i.e., extent, inclination), location (e.g., façade, pillar, roof, decorative elements, etc.) and aperture (i.e., width, dislocation) of cracks can be determined on the field.

According to Burland et al. (1977), the approximate crack width (w) can be used to classify the severity of building damage in: negligible ($w < 0.1$ mm), very slight ($w < 1$ mm), slight ($w < 5$ mm), moderate ($5 < w < 15$ mm), severe ($15 < w < 25$ mm), and very severe ($w > 25$ mm). Once field surveys are performed, the information collected for each building can be stored in factsheets and used for future assessment of the damage evolution (e.g., Nappo et al., 2021a; Peduto et al., 2017c).

## 2.6 Road damage assessment in landslide-affected areas

Ground movements induced by landslides can compromise the serviceability and efficiency of linear transportation networks causing damage to their pavement (Ferlisi et al., 2020a; Mavrouli et al., 2019; Nappo et al., 2019, 2021b; Postance et al., 2017). This Section reviews the typologies of asphalt road damage and their associated causes as reported in pavement distress catalogues (e.g., AASHO, 1962; ANAS, 2004; ASTM, 2020), the current practices in classifying road damage severity in landslide vulnerability analyses, the indices used to assess the quality of asphalt road pavements under usual stress conditions, and the advancements in (automatic) detection of road pavement distress.

### 2.6.1 Types of asphalt road damage

Asphalt-paved roads are subjected to vehicle loading, weathering, environmental effects (e.g., tree roots expansion), and ground and slope instabilities that determine cracking, distortion and disintegration (Tab. 2.1) of the surficial asphalt layer (AASHO, 1962; ANAS, 2004; ASTM, 2020; Nappo et al., 2021b). Longitudinal and transverse cracks, depressions and upheavals of the road pavement are typically caused by ground/slope instabilities (Ferlisi et al., 2020a; Mavrouli et al., 2019; Nappo et al., 2019, 2021b; Peduto et al., 2020). However, Nappo et al. (2021b) demonstrated that differentiating between causes of damage on asphalt road pavements is not straightforward due to the synergistic action of multiple factors impacting on the road pavement and adjacent assets (e.g., ditch, curbs, retaining wall, etc.).

***Table 2.1.*** *Types and causes of damage on asphalt road pavements (modified from AASHO, 1962; ANAS, 2004; ASTM, 2020; Nappo et al., 2021b).*

| Class of damage | Typology of damage | Associated cause |
|---|---|---|
| Cracking | Fatigue cracking (alias alligator cracks) | Traffic loading<br>Insufficient pavement thickness |
| | Block cracking | Shrinkage of the pavement |
| | Longitudinal and transverse cracking | Shrinkage of the pavement<br>Poor construction joints<br>Local settlements |
| | Edge cracking | Lack of support at the pavement edge |
| | Reflection cracking | Poor construction materials |
| | Slippage cracking | Traffic loading<br>Vehicle motion |
| Distortion | Rutting | Lack of subgrade compaction<br>Poor asphalt mixture<br>Insufficient pavement thickness |
| | Shoving | Poor asphalt mixture |
| | Depression (alias bird-bath) | Local settlement<br>Poor construction materials |
| | Upheaval | Frosting of the asphalt pavement<br>Poor asphalt mixture<br>Local settlement |
| Disintegration | Ravelling | Water infiltration<br>Traffic loading<br>Poor asphalt mixture |
| | Potholes | Poor asphalt mixture |

### 2.6.2 Classification of road damage severity

The severity of road pavement damage is commonly described as function of the affecting hazard using qualitative or quantitative approaches (Nappo et al., 2021b). Qualitatively, the damage severity can be classified according to the blockage of the road infrastructure (from partial to total interruption), the number of casualties and/or the repair costs to restore the pavement functionality (Donnini et al., 2017; Petrucci and Gullà, 2010; Winter, 2019). Quantitative methods classify the damage in different severity levels based on the landslide velocity and/or (differential) displacement rates associated to the damage patterns (Ferlisi et al., 2020a; Mansour et al., 2011; Mavrouli et al., 2019; Nappo et al., 2019). However, these classification criteria do not consider the intrinsic features (e.g., roughness) of the asphalt road pavement in rating the landslide-induced damage severity (Nappo et al., 2021b).

### 2.6.3 Asphalt road pavement quality indices

The International Roughness Index (IRI), the Pavement Condition Index (PCI) and the Pavement Serviceability Index (PSI) are indicators of the structural and operational performance of asphalt road pavements based on their roughness, skid resistance, bearing capacity, traffic loading and pavement aging (George et al., 1989; Hatmoko et al., 2019; Nappo et al., 2021b; Pawar et al., 2018; Ragnoli et al., 2018; Tan and Li, 2019). These indices are adopted in road maintenance practices to rate the infrastructure condition and plan interventions, but without considering the typology, extent and severity of pavement distress or the effects of ground/slope instabilities on the road pavements (Nappo et al., 2021b).

The International Roughness Index (IRI) defines the deviation of the longitudinal profile of the road pavement in its current condition from a reference planar surface representing the design condition of the infrastructure (ASTM, 2015). Zak (2016) demonstrated that the road roughness usually obtained from laser profilers (ANAS, 2004; ASTM, 2015) can be equally computed from a 3D point cloud representing the road surface.

### 2.6.4 Advancements in road damage detection

The road pavement damage is traditionally assessed via visual inspections aimed at determining the overall quality of the infrastructure, with the disadvantages of subjective interpretations and time-consuming surveys (Coenen and Golroo, 2017; Gharaibeh and Lindholm, 2014; Inzerillo et al., 2018; Nappo et al., 2021b; Ragnoli et al., 2018; Wang et al., 2019). Digital technologies and computer vision algorithms are progressively replacing manual inspections. Terrestrial or Mobile Laser Scanners (TLS or MLS) and Unmanned Aerial Vehicles (UAV) are nowadays common in commercial and industrial practice for rapid acquisitions and/or mapping of different components of the roadway transport systems (Inzerillo et al., 2018; Ragnoli et al., 2018 – Tab. 2.2). TLS acquires the 3D spatial coordinates of points on the road surface by measuring the distance between the target and the device that emits the laser pulse (Vosselman and Maas, 2010). MLS reconstructs the 3D model of a road by acquiring single or multiple scans of the investigated target from a moving vehicle (Ragnoli et al., 2018; Schnebele et al., 2015). Fixed-wing, rotorcraft, and VTOL types of UAV (Greenwood et al., 2019) are often equipped with RGB digital or video cameras with different pixel resolutions acquiring images of the road infrastructure in the nadir or oblique directions (Nex and Remondino, 2014).

***Table 2.2.*** *Overview of the use of Terrestrial and Mobile Laser Scanner (TLS and MLS) and Unmanned Aerial Vehicles (UAV) in road-related studies.*

| Instrument | Reference |
|---|---|
| TLS | (Akgul et al., 2017; Alhasan et al., 2017; Chang et al., 2005; Ouyang and Xu, 2013) |
| MLS | (De Blasiis et al., 2020; Kumar et al., 2015; Gavilan et al., 2011; Guan et al., 2015; Hervieu and Soheilian, 2013; Van Der Horst et al., 2019) |
| UAV | (Cardenal et al., 2019; Kim et al., 2015; Nappo et al., 2021b; Saad and Tahar, 2019; Tan and Li, 2019) |
| TLS and UAV | (Inzerillo et al., 2018) |

When the two-dimensional (2D) UAV images are acquired with an appropriate overlapping (e.g., 80% - Giordan et al., 2020; Nex and Remondino, 2014), they can be processed with photogrammetric algorithms to reconstruct high-resolution 3D point clouds of the investigated road. These models are composed by a set of 3D points identified by their (x, y, z) coordinates that contain (geometric) information implicitly represented by the spatial arrangement of the 3D points (Hackel et al., 2016; Weinmann et al., 2013). In their raw form, point clouds need to be processed by typically constructing spherical, cylindrical or circular neighbourhoods around each 3D point and calculating their invariant moment to retrieve geometric features and classify large sets of unorganized points (Maas and Vosselman, 1999; Weinmann et al., 2013). These features describing the geometric relations between 3D points are selected according to the aim of the study, since some of them may result redundant or irrelevant (Weinmann et al., 2013). The reconstruction of such 3D models of the road surface facilitates the (automatic) detection of pavement damage with centimetric accuracy (Nappo et al., 2021b; Remondino et al., 2017). Alternatively, 2D UAV images can be processed with computer vision algorithms (e.g., edge detectors, convolutional neural network, deep learning) to detect fractures on the road surface (e.g., Cubero-Fernandez et al., 2017; Kim et al., 2015; Oliveira and Correia, 2013; Powell and Satheeshkumar, 2017; Puan et al., 2007).

To the author's knowledge, a combination of 2D images and 3D models have been used exclusively to identify distress on un-paved rural roads (Zhang and Elaksher, 2012), but not to detect and classify road pavement damage in landslide areas.

# 3. INSAR FOR MULTI-SCALE MONITORING OF SUBSIDENCE: THE CASE OF COMO (N ITALY) [2]

The city of Como is naturally prone to subside at a rate of few mm/year because built on a sequence of more than 70 m of unconsolidated Late Pleistocene to Holocene silty and clay sediments at the southwest shore of Lake Como in northern Italy (Comerci et al., 2007; Ferrario et al., 2015a; Nappo et al., 2020, 2021a).

Since the founding of the city in 59 BC, anthropogenic activities have amplified the rate of subsidence inducing non-negligible damage to (historic) buildings and roads in the urban area (Nappo et al., 2021a; Polcari et al., 2019). During the I century BC, ancient Romans deeply modified the morphology of the valley that, at the time, was marshy with sandy and gravelly deposits transported by two local streams, named Cosia and Valduce (Ferrario et al., 2015b; Martinelli et al., 2019). Romans culverted these streams confining them at the east and west borders of the new-born city of Como and reshaped the coastline reclaiming more land towards the lake. Later, between 1950 and 1970, the extensive extraction of water from a deep confined aquifer (Comerci et al., 2007), land reclamation and urban sprawl caused a tenfold increase in the subsidence rate of the city up to 20 mm/year along the lakeshore (Ferrario et al., 2015a; Nappo et al., 2020). The anthropogenically amplified subsidence caused severe damage to infrastructure and historic buildings of the city centre (Bajni et al., 2019; Comerci et al., 2007; Nappo et al., 2021a; Polcari et al., 2019). Therefore, after numerous reports of damage in the urban area of Como, in 1976 the Municipality of Como established a scientific and technical commission (called “Commissione Subsidenza”) to investigate the causes of ground lowering in the valley and assess the consequences of subsidence on (infra)structures (Comune di Como, 1980). The commission collected levelling measurements dated 1928-1979 and borehole samples to assess the hydrogeological, geotechnical and stratigraphic setting of the valley; and also performed the first damage survey of the city of Como in 1975 (Comune di Como, 1980). Once the information was evaluated, the commission stated that i) the natural subsidence affecting the basin of Como was due to highly compressible silty and clay sediments with poor

---

[2] The contents of this Chapter are based on Nappo et al. (2020) and Nappo et al. (2021a).

mechanical properties, ii) the groundwater and Lake Como levels influenced the rate of natural subsidence, iii) the anthropogenic subsidence had a rapid development since the early 50s and then decreased in 1975–1979 with velocities up to 10 mm/year in few locations, and iv) the ground settlements affecting the buildings were significant but almost homogeneous at the basin scale; therefore, they could not establish any correlation between structural damage and subsidence at the single building scale (Comune di Como, 1980; Ferrario et al., 2015a; Nappo et al., 2021a). After the investigations of the Commissione Subsidenza, the water extraction from the deep aquifer was ceased and the compressible soil layers experienced a slight recovery between 1980 and 1997 (Comerci et al., 2007). Then, the Municipality of Como commissioned (in 1996) and began (in 2004) the construction of fixed and movable bulkheads, detention tanks, and jet grouting barriers along the lakefront (Bajni et al., 2019), aiming at mitigating the occasional flooding that the city still experiences (Ferrario et al., 2015a; Nappo et al., 2020). The execution of such anti-flooding facilities altered the groundwater regime of the valley once again, thus determining the suspension of the construction site in 2011 (Nappo et al., 2020). In July 2020, the Lombardy Region administrating the construction site on Lake Como announced in a press conference the resumption of works, which are expected to be completed by 2023.

Although the very detailed knowledge of Como geological framework and landscape evolution (Bini 1987, 1993, 1996; Bini and Castelletti, 1986; Castelletti and Orombelli, 1986), hydrogeological setting (Apuani et al., 2000; Beretta et al., 1986), archaeology (Caniggia, 1968; Ferrario et al., 2015b; Luraschi, 1987; Uboldi, 1993), active tectonics (Livio et al., 2011; Michetti et al., 2012; Sileo et al., 2007), post-Last Glacial Maximum evolution (Comerci, 2004; Comerci et al., 2007; Martinelli et al., 2019), hydrogeological (Ferrario et al., 2015a) and geotechnical (Bajni et al., 2019) models of the subsoil, a standard procedure to efficiently manage subsidence risk in the city of Como is still lacking.

Therefore, with application to the case of Como, this research proposes a multi-scale framework to monitor the subsidence at large (i.e., basin) scale and analyse the small scale consequences induced on (historic) buildings by exploiting multi-platform InSAR measurements from 1992 to 2019 and the deep knowledge of the geological and stratigraphic setting of the city of Como (Nappo et al., 2020, 2021a). First, a multivariate regression analysis was performed at basin scale to establish what combination of natural (i.e., compressible soils and piezometric level) and anthropogenic (e.g., the diversion of the local streams) factors most likely determines subsidence in the study area, and investigate the relationships between subsidence predisposing factors (SPF) and InSAR-derived ground movements (Nappo et al., 2020). The interpretation of the spatial pattern of subsidence in the basin of Como allowed determining areas where the InSAR signal can be mostly attributed to the ground movements rather than other natural and/or anthropogenic influences, such as the Como historic centre (Nappo et al., 2020). This also allowed giving new insights on areas where further (geological) investigations are needed to properly interpret the InSAR measurements as ground movements originated by subsidence. Then, the vulnerability of the buildings in Como historic centre (named "Città murata") was assessed by coupling the InSAR-derived subsidence intensity measure and the severity of building damage determined in-situ (Nappo et al., 2021a). The correlation between subsidence-related intensity (SRI) and building damage severity was investigated by testing two parameters (i.e., differential settlement and relative rotation) representing the movement at building foundation depth, thus generating empirical fragility curves as a first attempt of vulnerability analysis in the city of Como (Nappo et al., 2021a).

This research aimed at providing the first integrated tool for subsidence risk management and preservation of the architectural heritage of the city of Como (Nappo et al., 2020, 2021a).

## 3.1 Hydrogeological, stratigraphic and geotechnical setting

The city of Como extends for about 37 km$^2$ at the southwestern shores of the lambda-shaped Lake Como (also called "Lario") in northern Italy (Fig. 3.1a). The Lake currently occupies a Pleistocene bifurcated glacial valley at an elevation varying from 197 to 210 m above sea level (a.s.l.) (Nappo et al., 2020). The SW branch of the Lake, called "Como branch", is hydrologically closed since ca. 18 thousand years (kyr) ago, thus being a perfect sedimentary trap for fine-grained (organic) lacustrine and palustrine deposits with high sedimentation rates (Ferrario et al., 2015a; Nappo et al., 2020). The inhabited area of the city of Como lies on a NW-SE oriented alluvial plain (Fig. 3.1b) drained by the Cosia and Valduce streams, whose riverbeds are currently culverted in the town underground (Nappo et al., 2020, 2021a). The plain is bordered by steep mountains composed of Mesozoic pelagic carbonates (i.e., Medolo Group – Early Jurassic) to the NE, and deep-sea fan conglomerates (i.e., Gonfolite Group – Oligo-Miocene) to the SW (Nappo et al., 2020, 2021a). The Gonfolite Group includes a thick sequence of conglomerates (i.e., Como and Villa Olmo Conglomerates) on top of sandstones and mudstones (i.e., Chiasso Formation) (Nappo et al., 2020). The trace of a regional backthrust (named "Gonfolite backthrust" – Fig. 3.1b) is concealed in the valley subsurface (Bernoulli et al., 1989; Sileo et al., 2007). During the Quaternary, the morphology of the basin was re-shaped by the erosional and depositional activity of glaciers (Bini, 1987; Michetti et al., 2014a, b; Rossi et al., 1991), thus determining the high heterogeneity of Como lithostratigraphic and geotechnical setting (Bajni et al., 2019; Ferrario et al., 2015a; Nappo et al., 2021a – Fig. 3.1c).

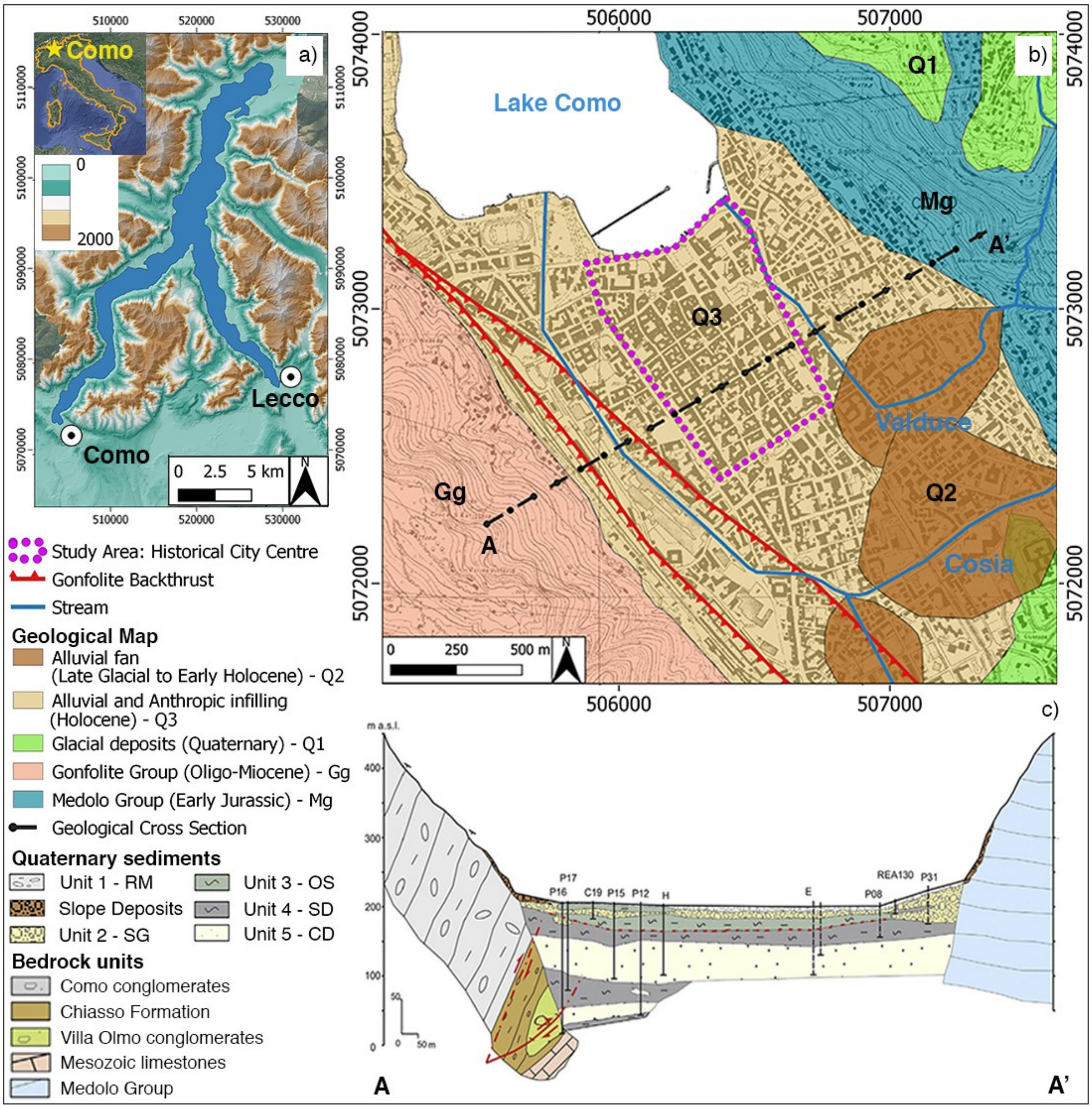

*__Figure 3.1.__ Modified from Nappo et al. (2020, 2021a). a) Location of the city of Como in N Italy at the SW shore of the Lake Como. b) Simplified geological map of the hydrologically closed basin of Como (modified after Michetti et al., 2014a). c) Geological cross section of the basin of Como (modified after Ferrario et al., 2015a). Reference system: WGS84/UTM zone 32N.*

Although only the upper ca. 180 m of the late Pleistocene to Holocene sedimentary sequence could be explored during drilling campaigns (Ferrario et al., 2015a), the three-dimensional sedimentary architecture of the Como basin is composed as follows (Ferrario et al., 2015a; Nappo et al., 2020, 2021a): i) heterogeneous reworked materials with archaeological remains (Unit 1 - RM) of maximum thickness varying from 10 m in the lakeshore area to 3 m moving SE; ii) alluvial sands and gravels up to 15–24 m (Unit 2 - SG); iii) palustrine organic and highly compressible silts (Unit 3 - OS) with sandy (Unit 3a) or clayey facies (Unit 3b) reaching their maximum thickness of 30 m in the centre of the basin and gradually decreasing up to 2 m at the margins; iv) glaciolacustrine sediments with dropstones up to 40–60 m (Unit 4 - SD) and v) coarser proximal deposits up to 80–100 m (Unit 5 - CD) with spatial distribution similar to Unit 3 - OS. Silty and highly compressible sub-units were also observed within the anthropogenic sediments along the lakeshore (Ferrario et al., 2015a; Nappo et al., 2020, 2021a).

Figure 3.2 shows an example of a typical stratigraphic sequence in the basin of Como with geotechnical parameters obtained via in-situ Standard Penetration Tests (SPT), Lefranc Permeability Tests (LPT), Cone Penetration Tests (CPT) and laboratory tests (Bajni et al., 2019; Comerci et al., 2007; Ferrario et al., 2015a).

The hydraulic gradients in the city of Como have been studied in detail since the 1970s by the "Commissione Subsidenza" (Comune di Como, 1980). Successive studies demonstrated that the groundwater of the basin of Como flows towards the lake, which represents the local base level (Bajni et al., 2019, Comerci et al., 2007; Ferrario et al., 2015a). Seasonal fluctuations of ca. 1.5 m of the piezometric level were also recorded in the proximity of the lake, with a decreasing trend moving towards SE (Ferrario et al., 2015a; Nappo et al., 2020, 2021a). Maximum variations of 0.5 m of the piezometric level were recorded 300 m far from the lakeshore (Ferrario et al., 2015a).

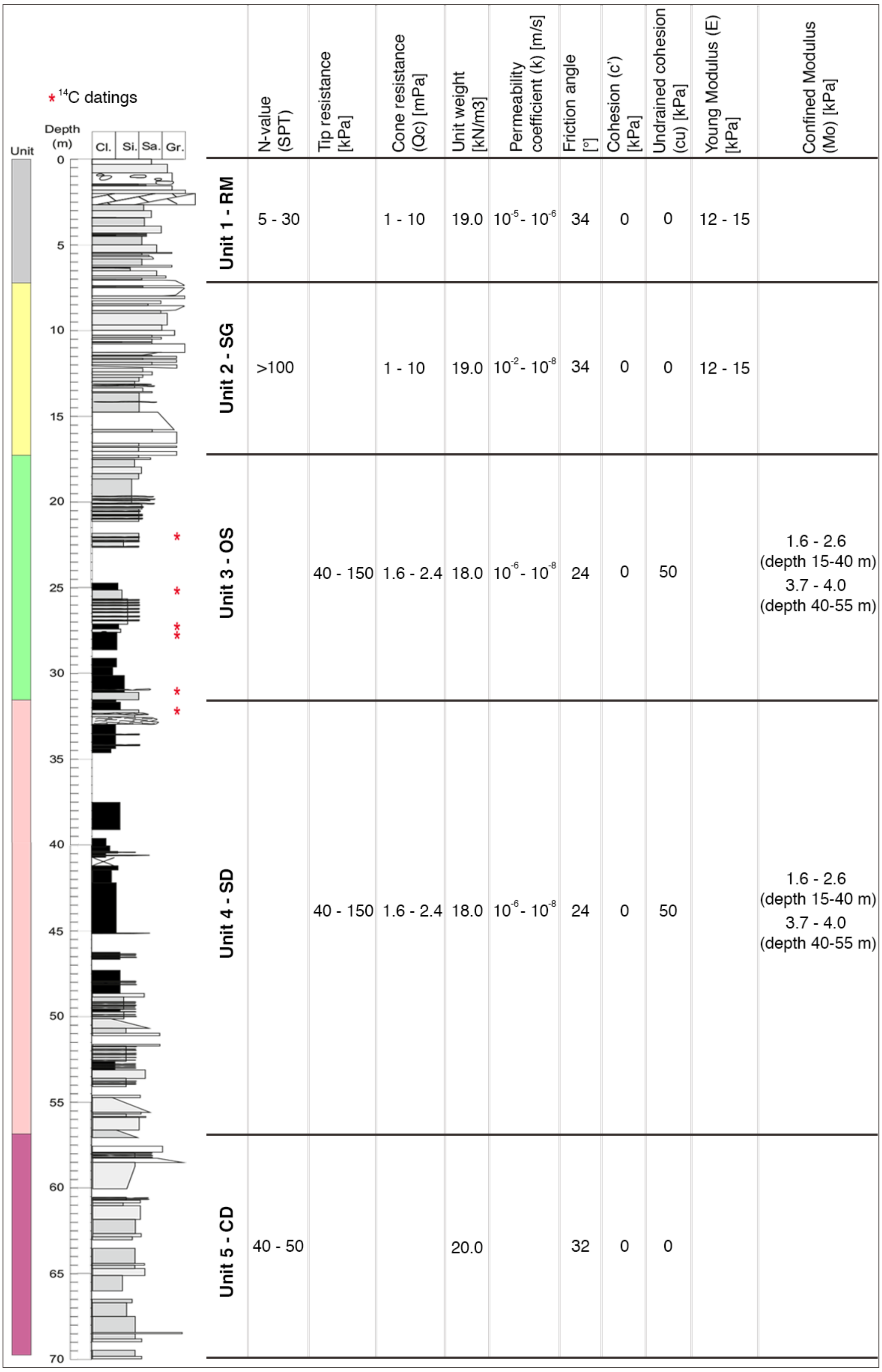

| Unit | N-value (SPT) | Tip resistance [kPa] | Cone resistance (Qc) [mPa] | Unit weight [kN/m3] | Permeability coefficient (k) [m/s] | Friction angle [°] | Cohesion (c') [kPa] | Undrained cohesion (cu) [kPa] | Young Modulus (E) [kPa] | Confined Modulus (Mo) [kPa] |
|---|---|---|---|---|---|---|---|---|---|---|
| Unit 1 - RM | 5 - 30 | | 1 - 10 | 19.0 | $10^{-5}$ - $10^{-6}$ | 34 | 0 | 0 | 12 - 15 | |
| Unit 2 - SG | >100 | | 1 - 10 | 19.0 | $10^{-2}$ - $10^{-8}$ | 34 | 0 | 0 | 12 - 15 | |
| Unit 3 - OS | | 40 - 150 | 1.6 - 2.4 | 18.0 | $10^{-6}$ - $10^{-8}$ | 24 | 0 | 50 | | 1.6 - 2.6 (depth 15-40 m)<br>3.7 - 4.0 (depth 40-55 m) |
| Unit 4 - SD | | 40 - 150 | 1.6 - 2.4 | 18.0 | $10^{-6}$ - $10^{-8}$ | 24 | 0 | 50 | | 1.6 - 2.6 (depth 15-40 m)<br>3.7 - 4.0 (depth 40-55 m) |
| Unit 5 - CD | 40 - 50 | | | 20.0 | | 32 | 0 | 0 | | |

***Figure 3.1.*** *Modified from Nappo et al. (2020). Example of a borehole profile of the basin of Como with Cl (clay), Sl (silts), Sa (sand) and Gr (gravel) particles and geotechnical parameters of the stratigraphic units (modified after Ferrario et al., 2015a).*

## 3.2 Materials

The data collected for the large scale multivariate regression (Nappo et al., 2020) and small scale vulnerability analyses (Nappo et al., 2021a) of the city of Como can be divided into three main categories: i) ancillary data, ii) InSAR data, and iii) building features.

### 3.2.1 Ancillary data

A topographic map (Carta Tecnica Regionale - CTR Lombardia) at a 1:10,000 scale (Fig. 3.3) and a digital terrain model (DTM) with 5 m spatial resolution were collected from the web repository of the Lombardia region (Geoportale Regione Lombardia, 2021).

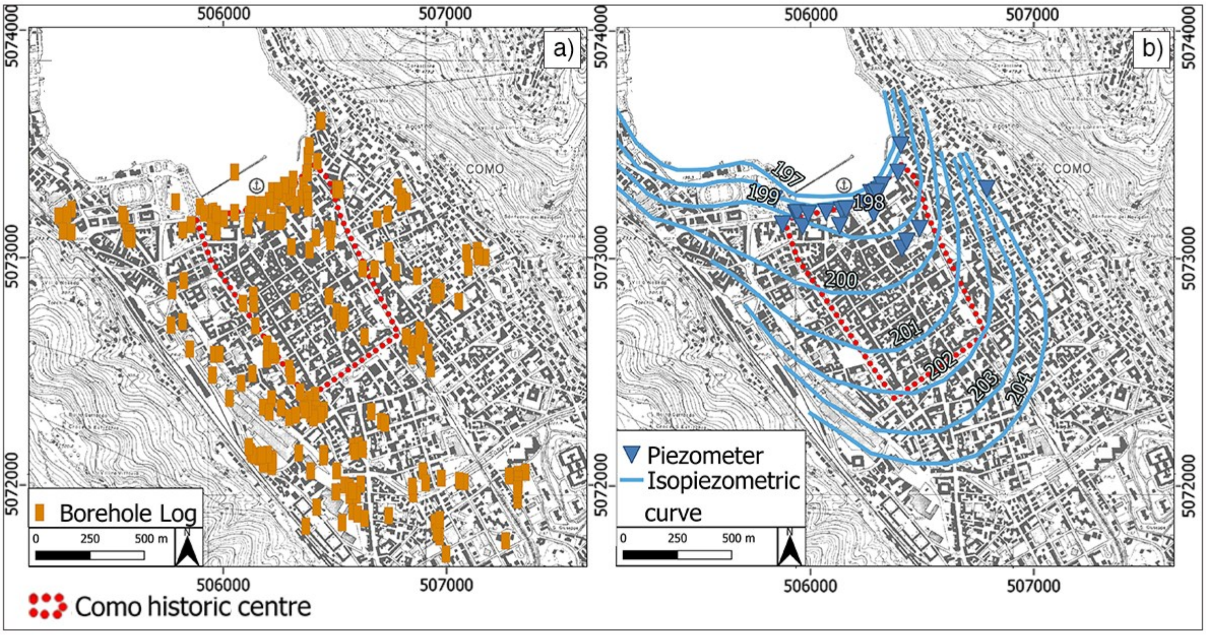

*Figure 3.2. Modified from Nappo et al. (2021a). Topographic map (Carta Tecnica Regionale - CTR) superimposed with a) borehole logs compiled by the University of Insubria (modified from Ferrario et al., 2015a and Nappo et al., 2020), and b) municipal piezometer network and isopiezometric curves (modified after Comune di Como, 1980; Ferrario et al., 2015a and Bajni et al., 2019). The red dotted line remarks the Como historic centre (i.e., "Città murata"). Reference system: WGS84/UTM zone 32N.*

The records of 261 borehole logs at different depths (Fig. 3.3a) obtained since the 1950s during drilling campaigns for public and private projects (e.g., building construction, water extraction, restoration of the Como lakefront) were collected from the repository of the University of Insubria (Ferrario et al., 2015a; Nappo et al., 2020, 2021a).

The depth of the phreatic water table in the basin of Como was measured until 2015 via 28 piezometers of the municipal piezometer network (Fig. 3.3b). Due to the lack of recent records of the groundwater depth in the basin, the mean level of the surficial aquifer was used here as an indicator of the piezometric level of the basin of Como (Bajni et al., 2019; Ferrario et al., 2015a; Nappo et al., 2020, 2021a). This level was represented via the isopiezometric curves reconstructed by the Commissione Subsidenza (Comune di Como, 1980 – Fig. 3.3b), as already proposed in literature (Bajni et al., 2019; Ferrario et al., 2015a; Nappo et al., 2020, 2021a).

### 3.2.2 InSAR data

A first set of InSAR sparse points (i.e., PS) derived from the European C-band ERS 1&2 (April 1992 – December 2000) and Envisat (July 2003 – July 2010) missions in ascending and descending orbits (Fig. 3.4 a and b) was supplied by the Italian Ministry of Environment, Land and Sea Protection via the "Piano Straordinario di Telerilevamento" (MATTM, 2010). The stack of 102 images from ERS 1&2 and 103 from Envisat was processed via E-geos PSP-DIFSAR technique (Constantini et al., 2008, 2009), and provided in form of PS with coherence greater than 0.6.

Then, an additional stack of 167 X-band Single Look Complex (SLC) SAR images acquired by the Italian Cosmo-SkyMed (CSK) mission in Strip-map mode from June 2010 to July 2019 along the descending orbit was requested to the Italian Space Agency (ASI). The granted SAR images were processed via multi-baseline Interferometric Point Target Analysis (IPTA) approach developed in the framework of GAMMA software (Wegmuller and Werner, 1997; Werner et al., 2003). Multi-look factor of 5 by 5 was applied to reduce the speckle noise and obtain 10 m pixel spacing as the ~10 m TINITALY Digital Elevation Model (DEM) that was used to remove the topographic contribution from the interferometric phase. The Goldstein filtering (Goldstein and Werner, 1998) and the minimum cost flow unwrapping algorithms (Costantini, 1998) were then applied to the data. An advantage of the IPTA approach is the possibility to find scatterers in low-coherence areas, thus filling spatial gaps in the deformation maps (Stramondo et al., 2008; Werner et al., 2003). This allowed setting the coherence threshold at 0.4 (Costantini, 1998) and include more interferometric image pairs in the analysis. Then, the interferograms with large atmospheric artefacts or unwrapping errors were discarded, and the remaining ones sampled by Singular Value Decomposition (SVD) analysis, thus

obtaining the set of PS shown in Figure 3.4c. Figure 3.4d shows the distribution of the standard deviation of PS obtained from processing CSK data.
A bedrock site located in the southern part of the basin of Como (i.e., Camerlata) was selected as the reference point for all InSAR analyses (Nappo et al., 2020, 2021a – Fig. 3.4).

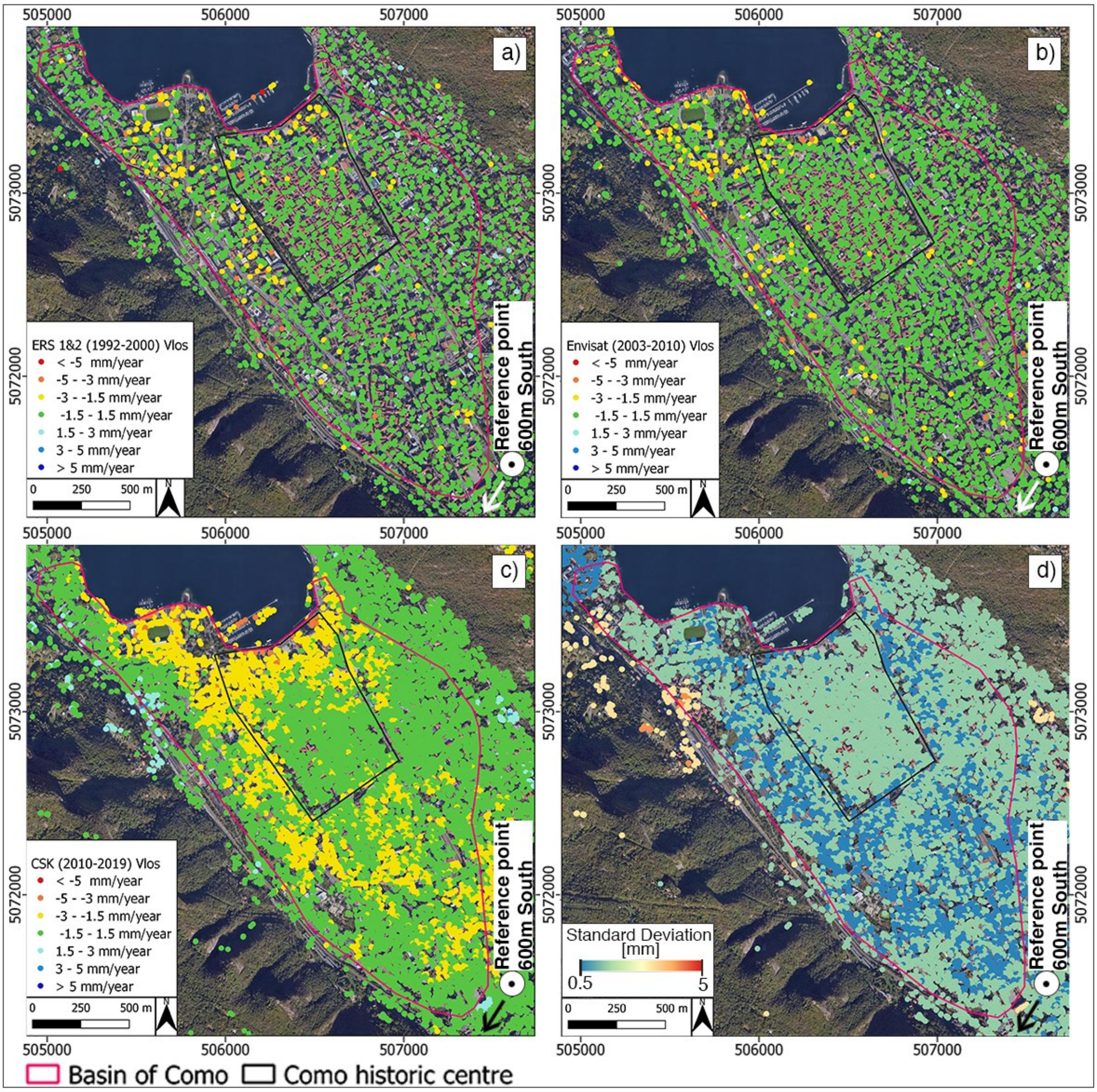

*Figure 3.3. Modified from Nappo et al. (2020, 2021a). Persistent Scatterers (PS) derived from a) ERS 1&2 (1992–2000) and b) Envisat (2003–2010) ascending and descending orbits, and c) CSK (2011-2019) descending orbit. The PS are represented according to seven LOS velocity classes. d) Standard deviation of CSK IPTA results. Reference system: WGS84/UTM zone 32N.*

Further details of ERS 1&2, Envisat and CSK missions and products are reported in Table 3.1.

***Table 3.1.*** *Modified from Nappo et al. (2020, 2021a). Details of exploited SAR missions and products.*

| **SAR Mission** | **ERS 1&2** | | **Envisat** | | **Cosmo-SkyMed** |
|---|---|---|---|---|---|
| Operator | European Space Agency (ESA) | | European Space Agency (ESA) | | Italian Space Agency (ASI) |
| Wavelength and frequency ($\lambda$) | C-band<br>$\lambda = 5.6$ cm | | C-band<br>$\lambda = 5.6$ cm | | X-band<br>$\lambda = 3.1$ cm |
| Revisiting time | 35 days | | 35 days | | 16 days |
| Acquisition geometry | Ascending | Descending | Ascending | Descending | Descending |
| Observation period | From 22/07/1995 to 20/08/2000 | From 30/04/1992 to 03/12/2000 | From 06/07/2003 to 04/07/2010 | From 11/04/2004 to 04/07/2010 | From 21/06/2010 to 08/07/2019 |
| Number of images | 25 | 77 | 50 | 53 | 167 |
| Number of PS | 848 | 2166 | 1826 | 2263 | 18,375 |
| Average density of PS (PS/km$^2$) | 53 | 135 | 114 | 141 | 1143 |
| Standard deviation ($\sigma$) | 0.88 | 0.81 | 0.70 | 0.72 | 1.05 |

### 3.2.3 Buildings features

The historic centre of the city of Como, called "Città murata" because surrounded by Roman walls, hosts 600 buildings of different typologies (Carta Tecnica Regionale – CTR). Most of them are masonry buildings (528 out of 600), some others are in reinforced concrete (57 out of 600) and a few are in stones (15 out of 600) (Nappo et al., 2021a). The buildings' geometric and structural information (i.e., volume, number of floors, construction material and year of construction) were collected from the web repository of the Municipality of Como (SiT, 2021) (Nappo et al., 2021a).

Figure 3.5 shows the buildings of Como historic centre distinguished by construction material and year of construction.

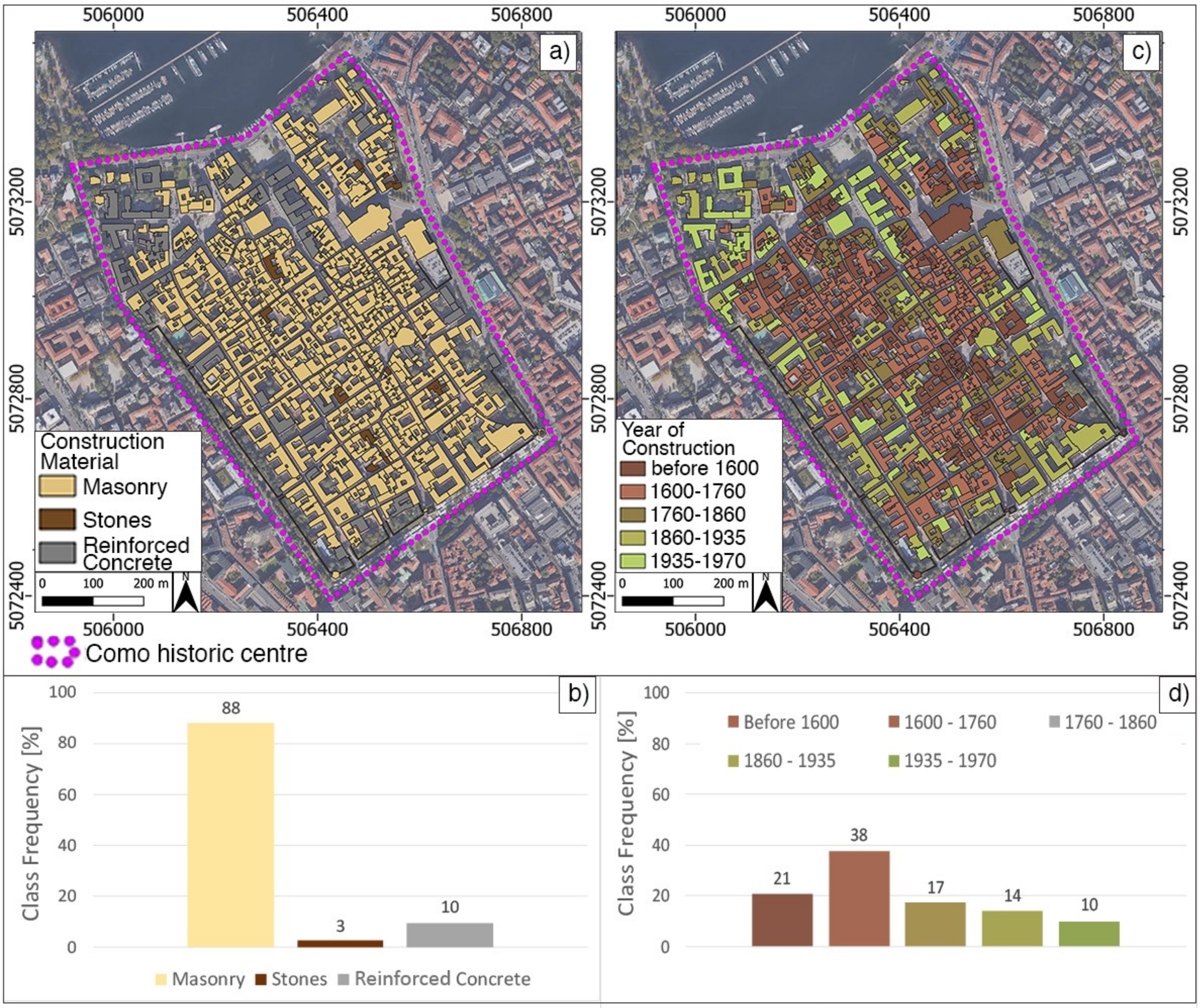

***Figure 3.4.*** *Modified from Nappo et al. (2021a). Classification of the 600 buildings of the Como historic centre according to their a) - b) construction material, and c) - d) year of construction. Reference system: WGS84/UTM zone 32N.*

As for the buildings' foundation system, this was not mentioned in such repository (SiT, 2021). Therefore, considering the construction practices of the buildings' fabrication epoch, the structures were assumed as resting on shallow foundations with a maximum depth of 4 m, thus intercepting only the Unit 1 – RM lithology (Nappo et al., 2021a).

Field investigations in the historic centre of Como were performed in June 2019 to evaluate the typology, geometry, location and aperture of fractures affecting the buildings. The classification of building damage severity was adapted from Burland et al. (1977), thus distinguishing negligible (w < 0.1 mm), very slight (w < 1 mm), slight (w < 5 mm) and moderate (w > 5 mm) severity levels (Fig. 3.6), here respectively denominated as D1, D2, D3 and D4 (Nappo et al., 2021a).

*Figure 3.5. Modified from Nappo et al. (2021a). Building damage severity classification adapted from Burland et al. (1977): a) negligible (w < 0.1 mm - D1); b) very slight (w < 1 mm - D2); c) slight (w < 5 mm - D3); d) moderate (w > 5 mm - D4). Field investigations were performed in June 2019.*

## 3.3 Methodology

The multi-scale investigation of subsidence in the city of Como was performed in two phases, as illustrated in Figure 3.7.

*Phase I* consists of a multivariate regression analysis at basin scale aimed at determining the correlations between subsidence predisposing factors (SPF) and InSAR-derived ground movements in the basin of Como, thus interpreting the spatial pattern of subsidence in the city (Nappo et al., 2020). In *Phase II*, the vulnerability of buildings in Como historic centre is assessed by investigating the relationship between the building damage severity and the subsidence-related intensity (SRI) parameter (i.e., differential settlement and relative rotation) derived from InSAR records, and generating empirical fragility curves (Nappo et al., 2021a).

The availability of C-band (i.e., ERS 1&2 and Envisat) and X-band (i.e., CSK) InSAR data allowed performing the regression analysis at basin scale (*Phase I*) using the C-band data referred to the years 1992-2010, and the vulnerability analysis at building scale (*Phase II*) with the X-band motion records from 2010 to 2019. Indeed, the higher resolution of CSK data allows more precise observations on single buildings compared to ERS 1&2 and Envisat, which are preferred instead for large scale analyses and subsidence mapping (e.g., Del Ventisette et al., 2013; Peduto et al., 2015).

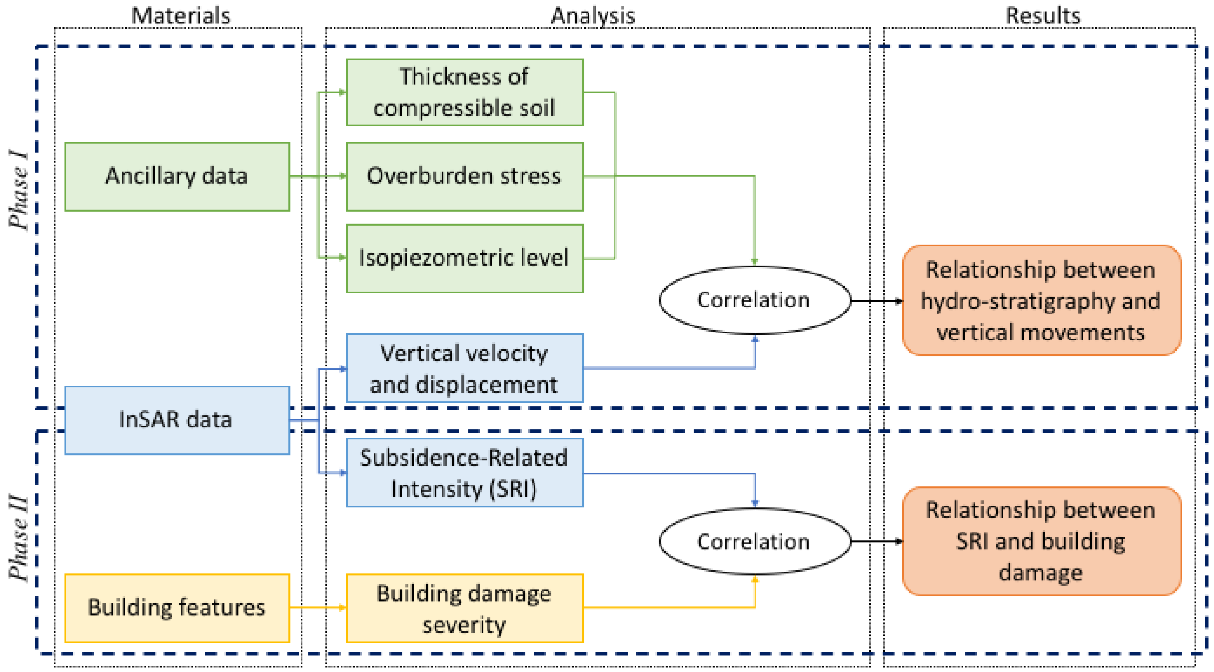

***Figure 3.7.*** *Modified from Nappo et al. (2020, 2021a). Schematic flowchart of the adopted methodology.*

### 3.3.1 Preliminary steps

Aiming at detecting the ground movements induced by subsidence in the city of Como, a slope map was derived from the DTM to extrapolate the flat area of the basin (steepness < 5°) and discard the Persistent Scatterers (PS) recorded on slopes steeper than 5° (Nappo et al., 2020). For each PS, the horizontal (i.e., East-West) and vertical components ($v_{EW}$ and $v_z$ respectively) of the LOS velocity were computed as suggested by Cascini et al. (2010b, 2013):

$$(3.1) \quad v_{EW} = v_{LOS}/(-\sin\vartheta \cdot \cos\alpha_s) \quad \text{and} \quad v_z = v_{LOS}/\cos\vartheta$$

where $v_{LOS}$ (mm/year) is the PS velocity recorded along the LOS direction; $\vartheta$ is the LOS incidence angle; and $\alpha_s$ is the angle between the azimuth and the north direction. Considering the vertical movements predominant in a flat subsiding area, like the basin of Como, the $v_{EW}$ could be neglected from further analyses (e.g., Nappo et al., 2020, 2021a; Peduto et al., 2015).

Then, the LOS and vertical cumulative displacements ($\delta_{cum}$ and $\delta_z$, respectively) of each PS were computed as:

$$(3.2) \quad \delta_{cum} = \delta_{last} - \delta_{first} \quad \text{and} \quad \delta_z = \delta_{cum}/cos\vartheta$$

where $\delta_{last}$ and $\delta_{first}$ are respectively the last and first measure of the PS displacement time series. These equations allow considering different distributions of the displacements over time, rather than simply linear (Nappo et al., 2021a).

### 3.3.2 *Phase I* – Multivariate regression analysis at large-scale

In *Phase I*, the subsidence predisposing factors (SPF) known to be affecting the basin of Como (i.e., thickness of compressible stratigraphic units, overburden stress and piezometric level) were obtained from the borehole logs and isopiezometric curves (Nappo et al., 2020, 2021a). Specifically, the thickness of Unit 1 – RM and Unit 3 – OS were extracted, and the overburden stress ($\sigma_v$) imposed on Unit 3 – OS at depth z (m) was computed as (Nappo et al., 2020):

$$(3.3) \quad \sigma_v = \int \gamma \cdot T_n \cdot dz$$

where $\gamma$ is the soil unit weight (N/m$^3$) and $T_n$ is the thickness (m) of the n-th stratigraphic unit. Then, the SPF were interpolated via Empirical Bayesian Kriging (EBK; Krivoruchko, 2012), and the InSAR $v_z$ obtained beforehand from ERS 1&2 (1992-2000) and Envisat (2003-2010) via Ordinary Kriging (Wackernagel, 1995) using an interpolation cell of 30x30 m. Different interpolation algorithms allowed considering different densities and spatial distributions of the input datasets (Nappo et al., 2020, 2021a). EBK with a power semivariogram type was preferred for sparse and heterogeneous boreholes data (Fig. 3.3a); while the high variability of InSAR data (Fig. 3.4) was better modelled by Ordinary Kriging with spherical semivariogram type (Nappo et al., 2020, 2021a).

Afterwards, a bivariate correlation analysis based on the Pearson's correlation coefficient (PCC) was performed to determine the (linear) dependency among SPF, which could be null (PCC < |0.25|), weak (|0.25|< PCC < |0.50|), moderately strong (|0.50|< PCC < |0.75|) or strong (|0.75|< PCC < |1|). Also, the correlation between InSAR $v_z$ and SPF was assessed to advise for a linear or nonlinear regression modelling. A further check was performed via the Farrar–

Glauber test (F-G test; Farrar and Glauber, 1967) to detect multicollinearity among SPF that could bias the regression model.

Linear and nonlinear regression analyses were conducted to evaluate the correlation between InSAR $v_z$ and SPF, respectively dependant and independent variables (Nappo et al., 2020). The first simulation was performed with a bivariate model, while the successive ones with multivariate models obtained by progressively implementing the number of independent variables (Nappo et al., 2020). The generalized linear model (GLM; Nelder and Wedderburn, 1972) with Gaussian probability distribution of the predicted variable and identity link function between InSAR $v_z$ and SPF was adopted for the linear regression analysis via the equation:

$$(3.4) \qquad y(x) = \beta_0 + \sum \beta_i x_i$$

where y(x) is the predicted InSAR $v_z$; $\beta_0$ is the parametric component of the linear predictors; $\beta_i$ (i = 1,…, n) are the unknown regression coefficients explaining the relationship between dependent and independent variables; and $x_i$ (i = 1,…, n) are the predictors (i.e., SPF).

The nonlinear regression was performed via generalized additive model (GAM; Wood, 2010) that gives more flexibility to the analysis via the equation:

$$(3.5) \qquad y(x) = \beta_0 + \sum s(x_i)$$

where $s(x_i)$ is a nonparametric smooth function representing the nonlinearity between the predicted $v_z$ and the predictors (i.e., SPF).

The performance of GLM and GAM was evaluated via adjusted R-squared (adj-$R^2$) and Akaike Information Criterion (AIC), thus determining the model that better represents the correlation between InSAR $v_z$ and SPF (Nappo et al., 2020).

### 3.3.3 *Phase II* – Building vulnerability analysis at small-scale

The CSK-derived PS data referred to years from 2010 to 2019 were exploited in *Phase II* to compute the differential settlements and relative rotations potentially experienced by the buildings of Como historic centre in the investigated time frame. To this aim, the building polygons extracted from the topographic map (Carta Tecnica Regionale – CTR) were first enlarged with a 2-m buffer to account for InSAR geolocation and topographic errors, and then intersected with the CSK PS map (Nappo et al., 2021a). For each building, the differential settlement (Δ) and relative rotation (θ), here used as descriptors of subsidence-related intensity (SRI), were computed as (e.g., Nappo et al., 2021a; Peduto et al., 2019; Zhang and Ng, 2005):

$$(3.6) \quad \Delta = |\delta_{z,max} - \delta_{z,min}| \quad \text{and} \quad \theta = \Delta/L$$

where $\delta_{z,max}$ and $\delta_{z,min}$ (mm) are respectively the maximum and minimum vertical settlements experienced by a building; and $L$ (m) is the distance between settling PS. The scheme of the SRI calculation is shown in Figure 3.8.

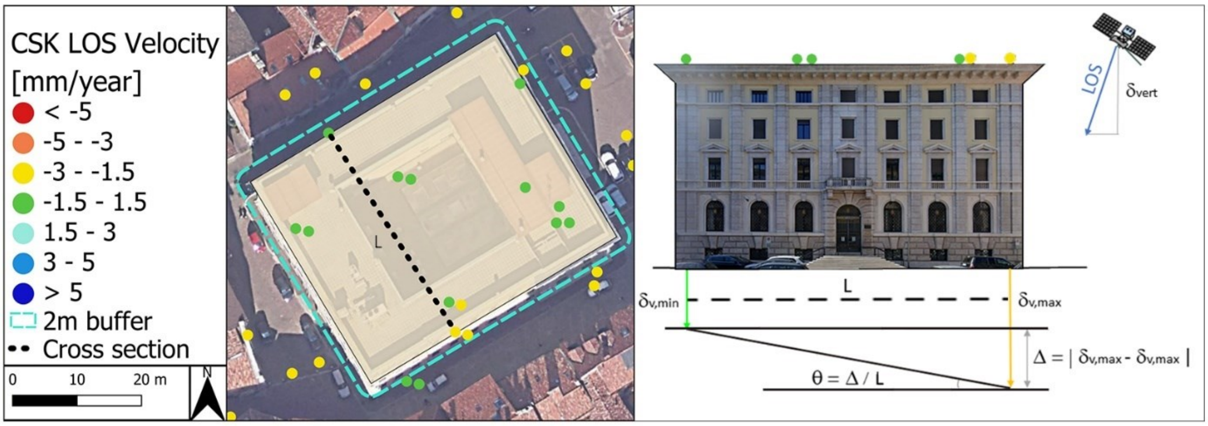

***Figure 3.6.*** *Modified from Nappo et al. (2021a). Scheme of the SRI calculation. Example of a masonry building in Como historic centre.*

For this research, the settlements computed via Equations 3.6 were assumed to occur at the buildings' foundation depth, thus disregarding both compressive and tensile strain that may affect the superstructure (Nappo et al., 2021a; Peduto et al., 2019).

Both SRI parameters were then correlated to the buildings' damage severity levels via fragility curves (Eq. 2.1), thus assessing the conditional probability for a building to reach or exceed a certain damage severity for a given SRI value (Nappo et al., 2021a).

## 3.4 Results

This paragraph illustrates the results of the multivariate regression (*Phase I*) and vulnerability analyses (*Phase II*) aimed at investigating the effects of subsidence in the city of Como, respectively at basin (i.e., large) and city-centre (i.e., small) scale.

### 3.4.1 The multivariate regression analysis at large-scale (*Phase I*)

The interpolations of ERS 1&2 (1992-2000) and Envisat (2003-2010) $v_z$ and SPF (i.e., thickness of Unit 1 – RM and Unit 3 – OS, overburden stress and piezometric level) are shown in Figure 3.9.

In both analysed time frames, the highest vertical velocity (~10 mm/year) is recorded in the Cosia stream delta area (i.e., the NW sector of the basin – Fig. 3.9a and b). This sector is characterized by a thickness of ~3 m of Unit 1 – RM (Fig. 3.8c) and ~25 m of Unit 3 – OS (Fig. 3.9d), average overburden stress of 300 N/m$^2$ (Fig. 3.9e), and piezometric level varying between 197 and 202 m a.s.l. (Fig. 3.9f). The lakeshore area also shows high vertical velocity (~5 mm/year - Fig. 3.9a and b) where Unit 1 – RM and Unit 3 – OS respectively reach 10 m and 20 m thickness (Fig. 3.9c and d), the overburden stress is 200–300 N/m$^2$ (Fig. 3.9e), and the piezometric level is 197-199 m a.s.l. (Fig. 3.9f).

Tables 3.2 and 3.3 show the results of the two bivariate correlation analyses based on Pearson's correlation coefficient (PCC). As already demonstrated by other authors (e.g., Bajni et al., 2019; Ferrario et al., 2015a), the piezometric level has a moderately strong correlation with the thickness of Unit 1 – RM and Unit 3 – OS (Tab. 3.2). A similar correlation resulted also between the piezometric level and InSAR $v_z$ (Tab. 3.3), thus remarking the need to check for multicollinearity.

However, when performing the Farrar-Glauber test, collinearity was not detected among variables, thus suggesting a nonlinear correlation between SPF and InSAR $v_z$. To further verify this relationship, all combinations of SPF were tested to predict InSAR $v_z$ via GLM (Tab. 3.4) and GAM (Tab. 3.5).

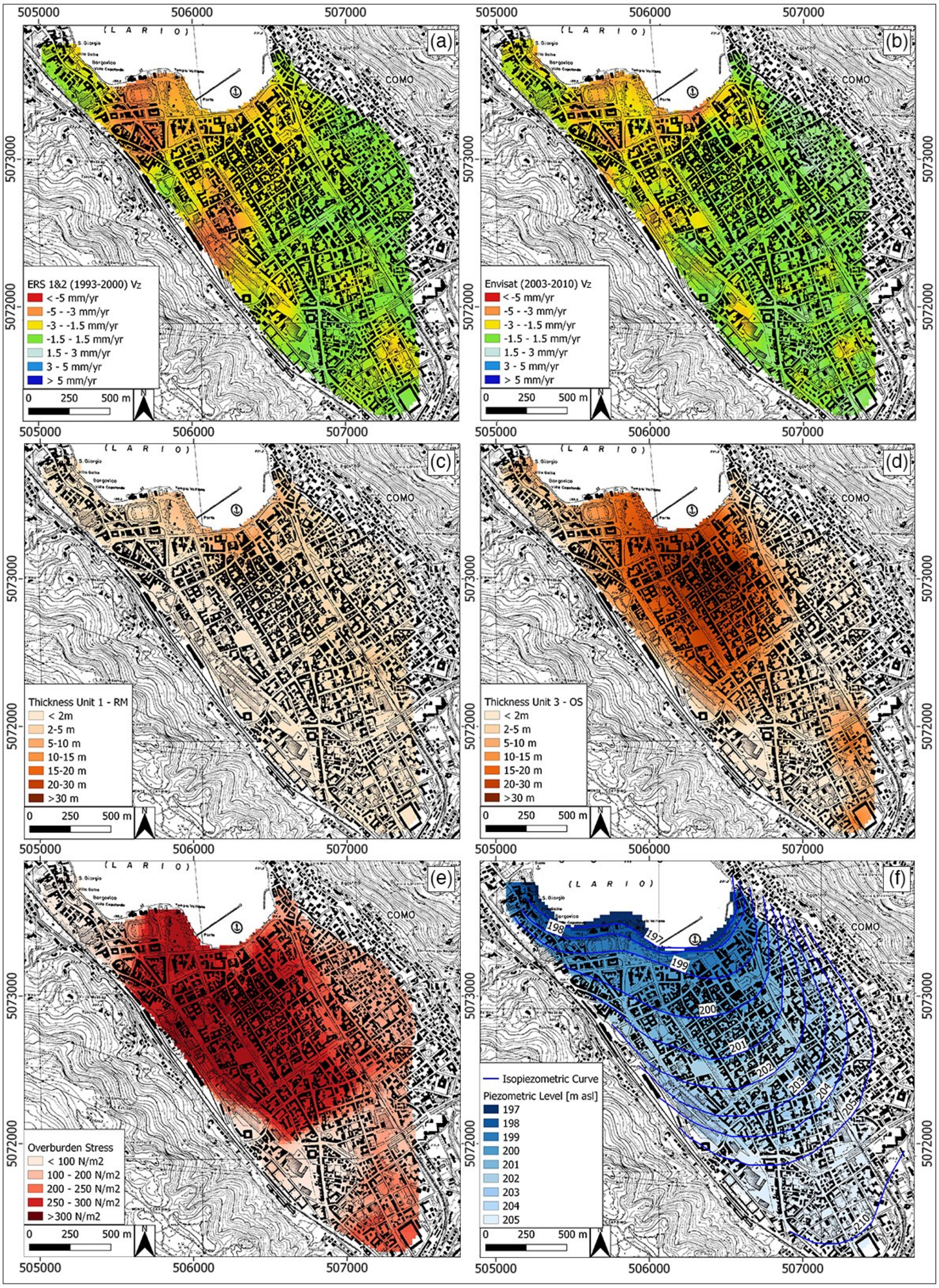

***Figure 3.7.*** *Modified from Nappo et al. (2020). Interpolation of a) ERS 1&2 (1992–2000) and b) Envisat (2003–2010) vertical velocity ($v_z$) via Ordinary Kriging. Interpolation of c) thickness of Unit 1 – RM, d) thickness of Unit 3 - OS, e) overburden stress ($\sigma_v$) and f) piezometric level via Empirical Bayesian Kriging (EBK). Blue curves represent the mean level of the surficial aquifer (i.e., isopiezometric curves) of the basin of Como (modified from Ferrario et al., 2015a). Reference system: WGS84/UTM zone 32N.*

***Table 3.2.*** *Modified from Nappo et al. (2020). Correlation matrix of the subsidence predisposing factors (SPF) based on Pearson's Correlation Coefficient (PCC).*

| | PCC and type of correlation | | | | | | | |
|---|---|---|---|---|---|---|---|---|
| | **Thickness of Unit 1 – RM** | | **Thickness of Unit 3 – OS** | | **Overburden stress ($\sigma_v$)** | | **Piezometric level** | |
| **Thickness of Unit 1 – RM** | | | 0.35 | Weak | 0.32 | Weak | -0.55 | Moderately Strong |
| **Thickness of Unit 3 – OS** | 0.35 | Weak | | | 0.25 | Weak | -0.62 | Moderately Strong |
| **Overburden stress ($\sigma_v$)** | 0.32 | Weak | 0.25 | Weak | | | -0.13 | Null |
| **Piezometric level** | -0.55 | Moderately Strong | -0.62 | Moderately Strong | -0.13 | Null | | |

***Table 3.3.*** *Modified from Nappo et al. (2020). PCC correlation analysis between InSAR $v_z$ and SPF.*

| | **ERS 1&2 (1992-2000)** | | **Envisat (2003-2010)** | |
|---|---|---|---|---|
| | PCC and type of correlation | | PCC and type of correlation | |
| **Thickness of Unit 1 – RM** | -0.16 | Null | -0.29 | Weak |
| **Thickness of Unit 3 – OS** | -0.52 | Moderately Strong | -0.44 | Weak |
| **Overburden stress ($\sigma_v$)** | -0.28 | Weak | -0.17 | Null |
| **Piezometric level** | 0.62 | Moderately Strong | 0.63 | Moderately Strong |

***Table 3.4.*** *Modified from Nappo et al. (2020). Summary of the tested linear regression models (M) via GLM with their respective adjusted R-squared (adj-$R^2$) and Akaike Information Criterion (AIC) values. Significance codes of p-values: *** = 0; ** = 0.001; * = 0.01; . = 0.05.*

| | $\beta_0$ | **Thickness of Unit 1 – RM** | **Thickness of Unit 3 – OS** | **Overburden stress ($\sigma_v$)** | **Piezometric level** | **adj-$R^2$** | **AIC** |
|---|---|---|---|---|---|---|---|
| | | | **ERS 1&2 (1992-2000)** | | | | |
| **M.1** | *** | * | *** | | | 0.27 | 10860 |
| **M.2** | *** | *** | *** | *** | | 0.30 | 10615 |

| | | | | | | | |
|---|---|---|---|---|---|---|---|
| **M.3** | *** | *** | *** | *** | *** | 0.52 | 8327 |
| **M.4** | *** | *** | *** | | *** | 0.46 | 9035 |
| **M.5** | *** | | | *** | *** | 0.42 | 9439 |
| | | | **Envisat (2003-2010)** | | | | |
| **M.1** | *** | *** | *** | | | 0.22 | 9251 |
| **M.2** | *** | * | *** | *** | | 0.22 | 9248 |
| **M.3** | *** | * | *** | *** | *** | 0.42 | 7386 |
| **M.4** | *** | *** | *** | | *** | 0.41 | 7484 |
| **M.5** | *** | | | *** | *** | 0.41 | 7491 |

***Table 3.5.*** *Modified from Nappo et al. (2020). Summary of the tested nonlinear regression models (M) via GAM with their AIC value. Significance codes of p-values: *** = 0; ** = 0.001; * = 0.01; . = 0.05.*

| | $\beta_0$ | **Thickness of Unit 1 – RM** | **Thickness of Unit 3 – OS** | **Overburden stress ($\sigma_v$)** | **Piezometric level** | **AIC** |
|---|---|---|---|---|---|---|
| | | | **ERS 1&2 (1992-2000)** | | | |
| **M.1** | *** | *** | *** | | | 9954 |
| **M.2** | *** | *** | *** | *** | | 9271 |
| **M.3** | *** | *** | *** | *** | *** | 7025 |
| **M.4** | *** | *** | *** | | *** | 8218 |
| **M.5** | *** | | | *** | *** | 9191 |
| | | | **Envisat (2003-2010)** | | | |
| **M.1** | *** | *** | *** | | | 8207 |
| **M.2** | *** | *** | *** | *** | | 9736 |
| **M.3** | *** | *** | *** | *** | *** | 6052 |
| **M.4** | *** | *** | *** | | *** | 6529 |
| **M.5** | *** | | | *** | *** | 7199 |

Based on the adjusted R-squared (adj-R$^2$) and the Akaike Information Criterion (AIC) (Tab. 3.4 and 3.5), the InSAR $v_z$ resulted to be predicted more accurately as a function of all SPF (i.e., thicknesses of Unit 1 – RM and Unit 3 – OS, overburden stress and piezometric level), whose statistical significance is determined by the p-values (Nappo et al., 2020). From the comparison of regression results obtained via GLM and GAM for both ERS 1&2 and Envisat, the AIC decreases when passing from linear to nonlinear regression, thus suggesting that greater flexibility in fitting the predictors (i.e., SPF) via GAM allows a better performance of the statistical model (Nappo et al., 2020).

The spatial distribution of regression residuals of the best fitted GAM (i.e., M.3 in Tab. 3.5) was then plotted in Figure 3.10 to verify the effectiveness of this regression model in representing the relationship between InSAR $v_z$ and SPF in the considered time frames (i.e., 1992-2000 and 2003-2010). Regression residuals are given by the difference between observed and predicted values and can express overestimations (when the residual value is < 0), perfect fit (when = 0) or underestimation (when > 0).

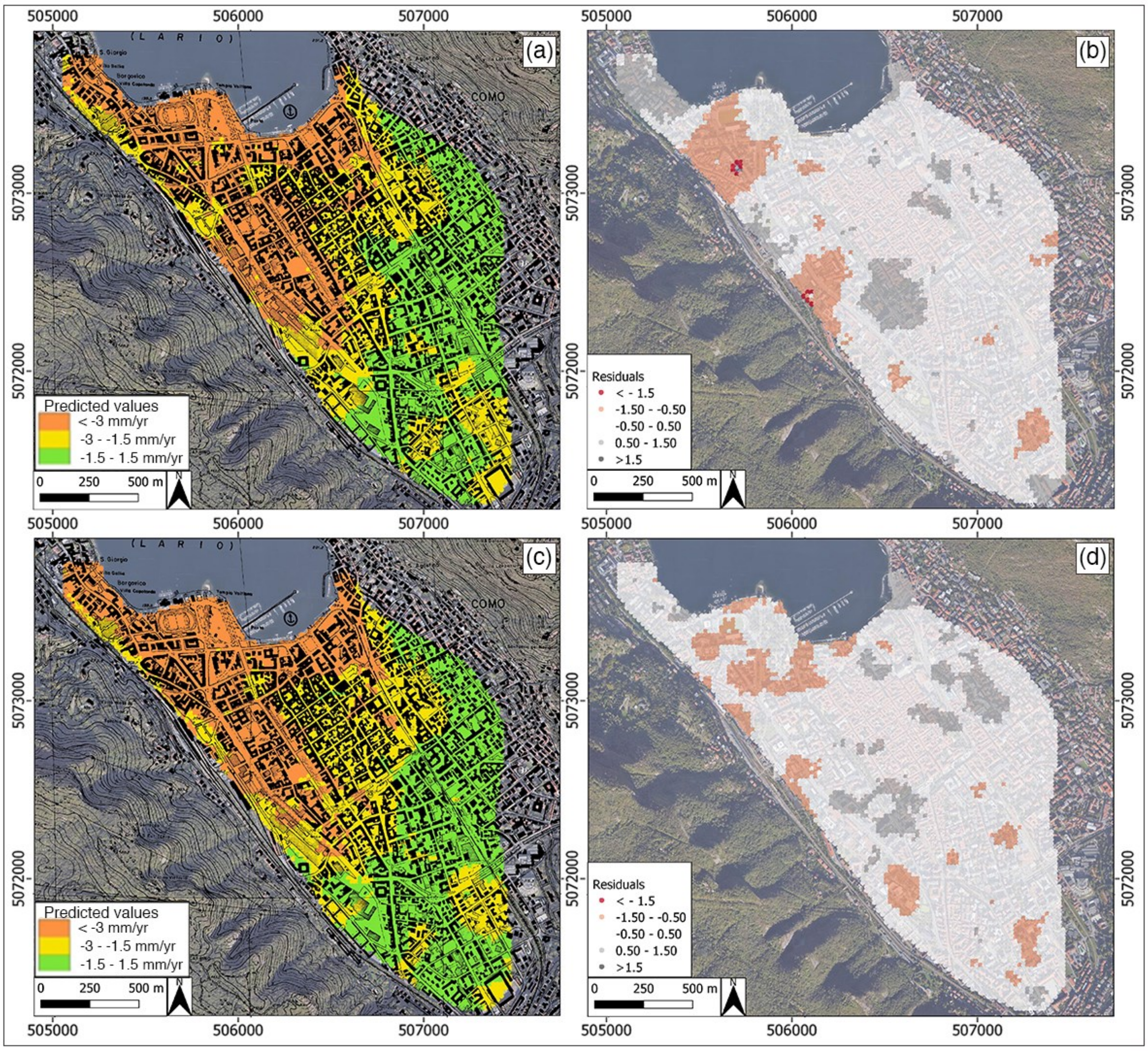

*__Figure 3.8.__ Modified from Nappo et al. (2020). Predicted values and regression residuals resulting from the GAM modelling of a) - b) ERS 1&2 (1992–2000) and c) - d) Envisat (2003–2010). Reference system: WGS84/UTM zone 32N.*

The residuals obtained from the best performing GAM (i.e., M.3 in Tab. 3.5) of the basin of Como are small and unstructured (Fig. 3.10). They show that 70% of the vertical velocity ($v_z$) recorded from ERS 1&2 (1992-2000) and Envisat (2003-2010) can be effectively explained via GAM using the SPF (i.e., thicknesses of Unit 1 – RM and Unit 3 – OS, overburden stress and piezometric level) as predictors (Nappo et al., 2020).
Some uncertainties persist in the Cosia stream delta area (i.e., the NW sector of the basin – Fig. 3.10), characterised by the anthropogenic culverting of the Cosia stream and the recent (Late Pliocene to Late glacial) activity of the Gonfolite backthrust (Livio et al., 2011; Michetti et al., 2014a, 2014b; Sileo et al., 2007) that could influence the ground movements detected by InSAR. To test these hypotheses, the distance from Cosia stream and the distance from the Gonfolite backthrust were introduced into the regression model as additional predictors. Although the GAM results improved of about 50% (AIC equal to 5802 for ERS 1&2 and 3336 for Envisat predictions) with respect to the previous analyses (Tab. 3.5) when considering the distance from Cosia stream, and of about 20% (AIC equal to 6813 for ERS 1&2 and 4663 for Envisat predictions) when introducing the distance from Gonfolite backthrust, the spatial distribution of regression residuals remained almost unchanged, thus suggesting that other causes may influence the InSAR $v_z$ in the NW sector of the basin (Nappo et al., 2020). Also, a model combining both variables could not be tested due to the collinearity between these new predictors (Nappo et al., 2020).

Despite the uncertainties, the multivariate regression analysis at large-scale allowed mapping the areas in the city of Como where the InSAR-derived movements can be most likely attributed to subsidence, such as the Como historic centre, and the areas where further (geological) investigations are needed before reliably performing a building vulnerability analysis, such as the NW sector of the basin.

### 3.4.2 The building vulnerability analysis at small-scale (*Phase II*)

Figure 3.11 shows the damage severity map (Fig. 3.11a) and the frequency distribution of damage severity classes (from D1 to D4 – Fig. 3.11b) of the 600 buildings surveyed in the Como historic centre in June 2019. The 66% of the buildings (i.e., 394 out of 600) resulted to be damaged, while the remaining 34% was labelled as “No Damage” because the facades showed no evidence of damage or were recently maintained (Nappo et al., 2021a). Once the topographic map had been overlaid with the CSK PS map and the subsidence-related intensity (SRI) parameters (i.e., differential settlement Δ and relative rotation $\theta$) computed via Equations 3.6, the surveyed buildings were classified also according to their Δ values (Nappo et al., 2021a – Fig. 3.11c and d). With this classification, 75% of the buildings (i.e., 449 out of 600) showed non-negligible differential settlements, here distinguished in four classes: Δ < 3 mm, 3 < Δ < 5 mm, 5 < Δ < 10 mm, and Δ > 10 mm (Nappo et al., 2021a).

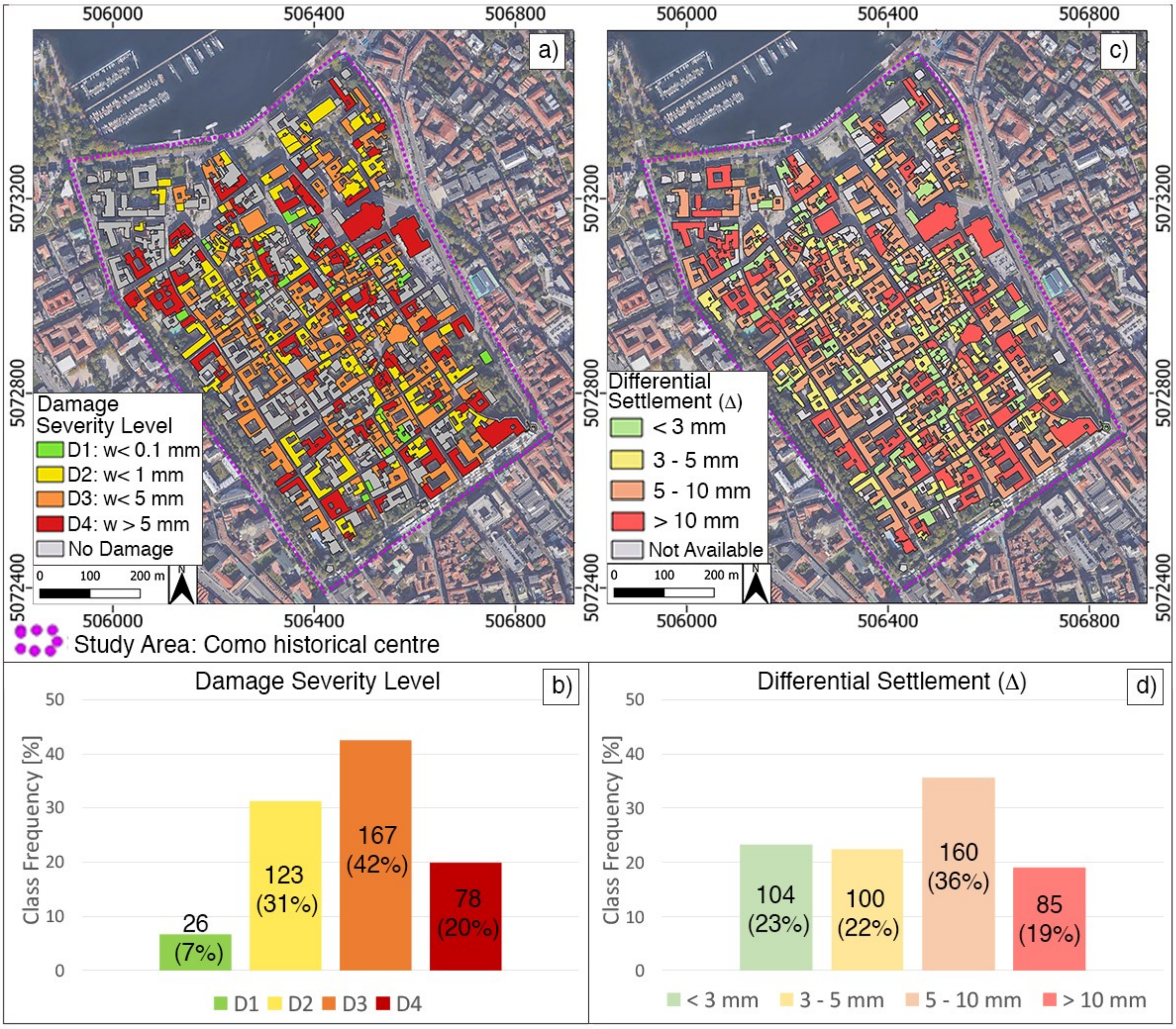

*Figure 3.9. Modified from Nappo et al. (2021a). a) Map of building damage severity for the Como historic centre. b) Distribution of D1 – D4 severity levels for the 394 damaged buildings. c) Map of InSAR-derived differential settlement Δ of buildings in the Como historic centre. d) Distribution of differential settlement classes (i.e., Δ < 3 mm, 3 < Δ < 5 mm, 5 < Δ < 10 mm, and Δ > 10 mm) for the 449 buildings with not-negligible Δ. Reference system: WGS84/UTM zone 32N.*

Table 3.6 reports the distribution per building construction material of the damage severity levels from D1 to D4 and the classes of non-negligible differential settlement.

***Table 3.6.*** *Modified from Nappo et al. (2021a). Distribution per building typology of the damage severity levels from D1 to D4 and the classes of non-negligible differential settlement.*

| **Damage Severity Level** | | | | | |
|---|---|---|---|---|---|
| **Construction Material** | **D1** | **D2** | **D3** | **D4** | **Total number** |
| Masonry (nr. 528) | 23 | 113 | 158 | 73 | 367 |
| Reinforced concrete (nr.57) | 3 | 8 | 6 | 3 | 20 |
| Stones (nr.15) | 0 | 2 | 3 | 2 | 7 |
| **Differential Settlement Δ (mm)** | | | | | |
| **Construction Material** | **Δ < 3** | **3 < Δ < 5** | **5 < Δ < 10** | **Δ > 10** | **Total number** |
| Masonry (nr. 528) | 91 | 91 | 138 | 72 | 392 |
| Reinforced concrete (nr.57) | 13 | 8 | 14 | 13 | 48 |
| Stones (nr.15) | 0 | 1 | 8 | 0 | 9 |

The obtained damage severity and differential settlement maps (Fig. 3.11a and c) were then intersected to estimate, per each typology of building (i.e., masonry, reinforced concrete and stones), the number of structures with damage severity level from D1 to D4 and non-negligible differential settlement (i.e., $\Delta \neq 0$), as reported in Table 3.7. This resulted in 275 (out of 528) masonry, 15 (out of 57) reinforced concrete and 2 (out of 15) stones buildings.

***Table 3.7.*** *Modified from Nappo et al. (2021a). Number of buildings with damage severity level from D1 to D4 and differential settlement* $\Delta \neq 0$.

| **Damage Severity Level of buildings with Δ ≠ 0** | | | | | |
|---|---|---|---|---|---|
| **Construction Material** | **D1** | **D2** | **D3** | **D4** | **Total number** |
| Masonry (nr. 528) | 14 | 69 | 120 | 72 | 275 |
| Reinforced concrete (nr.57) | 3 | 4 | 5 | 3 | 15 |
| Stones (nr.15) | 0 | 0 | 0 | 2 | 2 |

The relationships between damage severity and SRI parameters (i.e., differential settlement Δ and relative rotation $\theta$) and the corresponding empirical fragility curves were obtained for the 275 masonry (Fig. 3.12) and 15 reinforced concrete buildings (Fig. 3.13) with damage severity level from D1 to D4 and non-negligible differential settlement (Tab. 3.7). Stone buildings were discarded because their limited number (i.e., 2 in Tab. 3.7) was insufficient to generate empirical fragility curves (Nappo et al., 2021a). The results obtained for both masonry and reinforced concrete buildings remark that as the SRI parameter (i.e., Δ or $\theta$) increases, the damage severity increases proportionally (Nappo et al., 2021a).

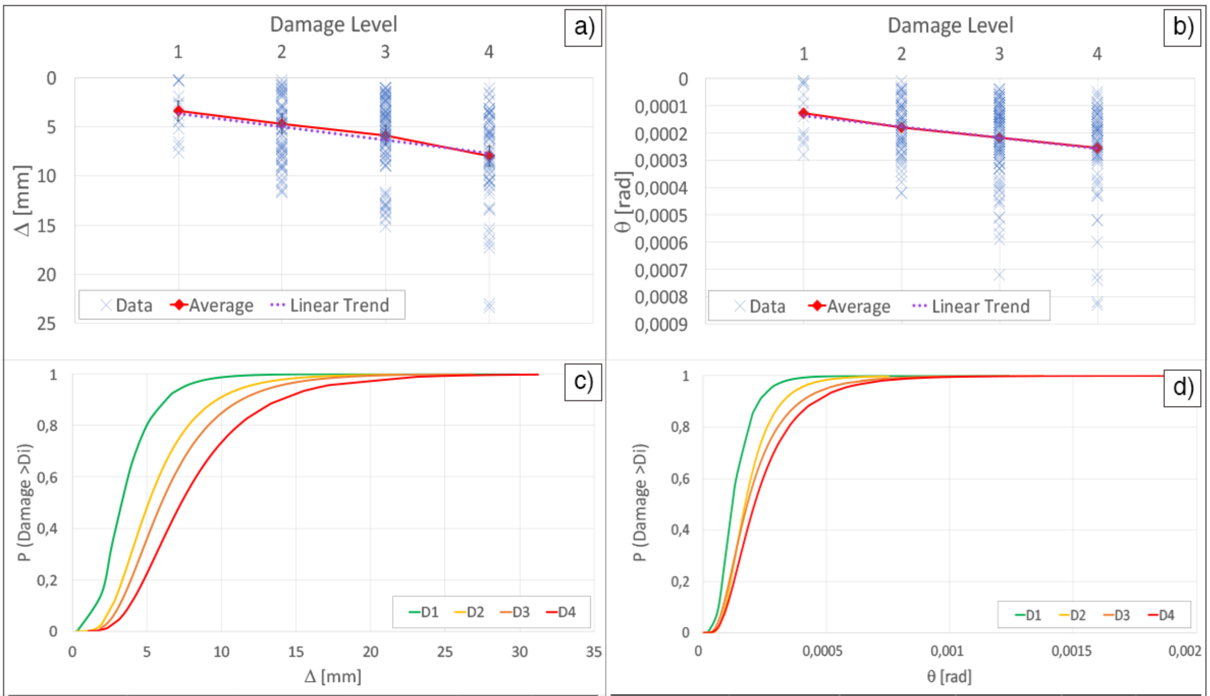

| Damage Level | Average Δ [mm] | Std.Dev. (σ)[mm] | Median ($\bar{\Delta}$)[mm] | β [mm] | CV |
|---|---|---|---|---|---|
| D1 | 3.38 | 2.60 | 3.27 | 1.32 | 0.77 |
| D2 | 4.67 | 3.18 | 5.10 | 0.83 | 0.68 |
| D3 | 6.61 | 3.83 | 6.00 | 0.71 | 0.58 |
| D4 | 7.97 | 4.67 | 7.31 | 0.62 | 0.59 |

| Damage Level | Average θ [rad] | Std.Dev. (σ) [rad] | Median ($\bar{\theta}$)[rad] | β [rad] | CV |
|---|---|---|---|---|---|
| D1 | 0.13E-03 | 9.80E-05 | 0.12E-03 | 1.25 | 0.75 |
| D2 | 0.18E-03 | 9.93E-05 | 0.17E-03 | 0.73 | 0.55 |
| D3 | 0.22E-03 | 0.13E-03 | 0.18E-03 | 0.62 | 0.59 |
| D4 | 0.26E-03 | 0.17E-03 | 0.21E-03 | 0.58 | 0.65 |

***Figure 3.10.*** *Modified from Nappo et al. (2021a). Vulnerability analysis of 275 masonry buildings in the Como historic centre. Correlation between damage severity levels and a) differential settlements (Δ) and b) relative rotation ($\theta$). Fragility curves and parameters of Equation 3.1 computed for c) differential settlements (Δ) and d) relative rotation ($\theta$).*

The fragility curves obtained for the 275 masonry buildings (Fig. 3.12c and d) show that the damage severity level D1 ($w < 0.1$ mm) is totally reached for $\Delta = 15$ mm or $\theta = 0.5\text{E-}03$ rad;

D2 (w < 1 mm) for Δ = 17 mm or $\theta$ = 0.6E-03 rad; D3 (w < 5 mm) for Δ = 20 mm or $\theta$ = 0.7E-03 rad; and D4 (w > 5 mm) for Δ = 25 mm or $\theta$ = 1.0E-03 rad (Nappo et al., 2021a). As verified in other studies using a larger sample of buildings (e.g., Peduto et al., 2019; Zang and Ng, 2005), both SRI parameters have low Coefficients of Variation (CV = σ/μ) commonly associated with more precise results (Nappo et al., 2021a). From the comparison of the two SRI parameters, the differential settlement allowed a better distinction between damage severity levels of masonry buildings in Como historic centre, and therefore should be preferred for future vulnerability analyses in the same area (Nappo et al., 2021a).

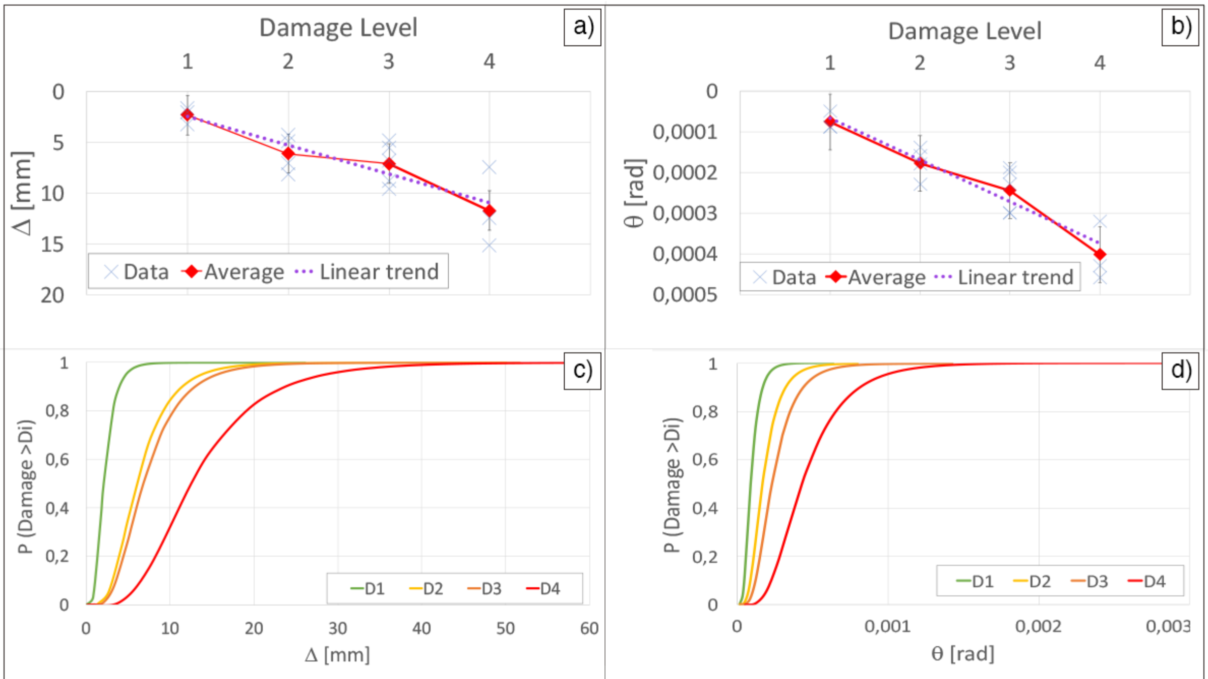

| Damage Level | Average Δ [mm] | Std.Dev. (σ) [mm] | Median ($\bar{\Delta}$) [mm] | β [mm] | CV |
|---|---|---|---|---|---|
| D1 | 2.34 | 0.80 | 2.07 | 0.33 | 0.34 |
| D2 | 6.14 | 1.81 | 6.03 | 0.30 | 0.29 |
| D3 | 7.15 | 2.04 | 6.84 | 0.29 | 0.28 |
| D4 | 11.73 | 3.93 | 12.51 | 0.37 | 0.33 |

| Damage Level | Average θ [rad] | Std.Dev. (σ) [rad] | Median ($\bar{\theta}$) [rad] | β [rad] | CV |
|---|---|---|---|---|---|
| D1 | 7.67E-05 | 2.31E-05 | 0.09E-03 | 0.34 | 0.30 |
| D2 | 0.18E-03 | 3.86E-05 | 0.17E-03 | 0.21 | 0.21 |
| D3 | 0.24E-03 | 5.32E-03 | 0.23E-03 | 0.22 | 0.22 |
| D4 | 0.40E-03 | 7.37E-03 | 0.43E-03 | 0.19 | 0.18 |

***Figure 3.11.*** *Modified from Nappo et al. (2021a). Vulnerability analysis of 15 reinforced concrete buildings in the Como historic centre. Correlation between damage levels and a) differential settlements (Δ) and b) relative rotation (θ). Fragility curves and parameters of Equation 3.1 computed for c) differential settlements (Δ) and d) relative rotation (θ).*

Similar trends of fragility curves were obtained also for the 15 reinforced concrete buildings (Fig. 3.13c and d), despite their limited number. In this case, the damage severity level D1 (w

< 0.1 mm) is totally reached for $\Delta = 7$ mm or $\theta = 0.3E\text{-}03$ rad; D2 (w < 1 mm) for $\Delta = 20$ mm or $\theta = 0.6E\text{-}03$ rad; D3 (w < 5 mm) for $\Delta = 22$ mm or $\theta = 0.8E\text{-}03$ rad; and D4 (w > 5 mm) for $\Delta = 40$ mm or $\theta = 1.3E\text{-}03$ rad (Nappo et al., 2021a). The Coefficients of Variation ($CV = \sigma/\mu$) computed for reinforced concrete buildings suggest a lower dispersion and a higher precision of data that the previous case (Nappo et al., 2021a). Also in this case, the differential settlement characterized better the different damage severity levels and should be preferred for future vulnerability analyses in the city of Como encompassing a larger number of reinforce concrete buildings (Nappo et al., 2021a).

Finally, Figure 3.12 shows a typical factsheet (e.g., Peduto et al., 2017c) reporting the geological, InSAR-derived and damage information of a masonry building in Como historic centre that could be used for future assessment of the damage evolution (Nappo et al., 2021a).

| ID | Height [m] | Floors | Material | Year of Construction | Data of Survey |
|---|---|---|---|---|---|
| 1,7 | 24 | 6 | Masonry | 1600-1760 | 3 Jun 2019 |

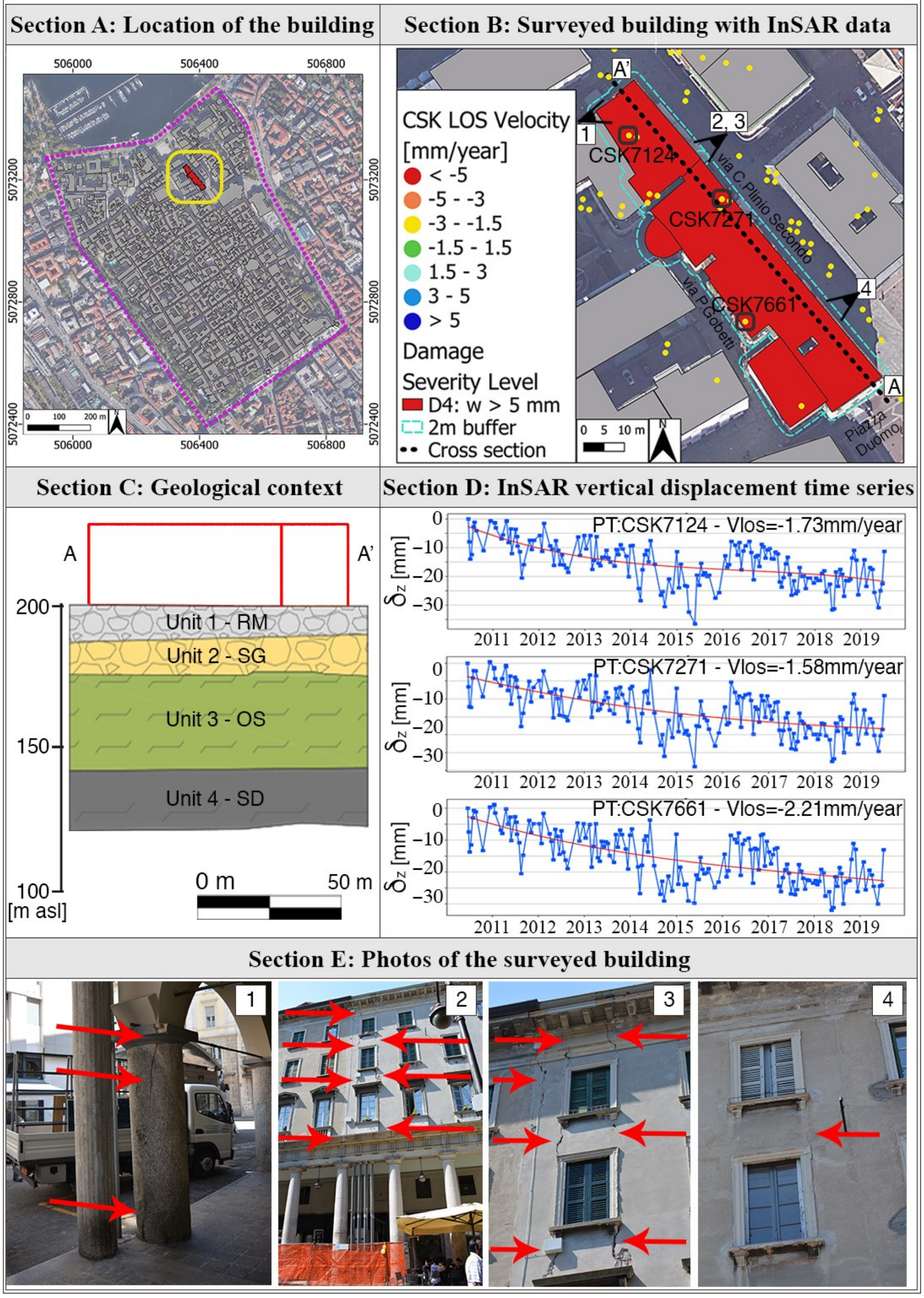

*Figure 3.12.* *Modified from Nappo et al. (2021a). Example of factsheet (modified from Peduto et al., 2017c) to store the geolocation (Section A), a closer view with InSAR data and damage severity information (Section B), the geological context (Section C), the InSAR vertical displacement time series (δz) (Section D), and some photos of the structural damage collected during the field survey (Section E) of buildings in the Como historic centre. Reference system: WGS84/UTM zone 32N.*

# 4. UAV FOR ROAD DAMAGE ASSESSMENT IN LANDSLIDE AREAS: THE PROVINCE OF COMO (N ITALY) [3]

The Province of Como extends for 1,279 km$^2$ in the Southern Alps of northern Italy (Fig. 4.1); the territory is predominantly mountainous (67%) and hilly (26%), with few plains (6%), and is formed by various lithologies of diverse tectonic origins (Nappo et al., 2021b). A dense road network, encompassing segments of different hierarchies (e.g., state, provincial, municipal), runs along steep mountains across the Province (Fig. 4.1a) connecting 148 municipalities.

Three geological sectors can be distinguished in this area (Fig. 4.1b): the Alpine Sector (Settore Alpino), the Prealpine Sector (Settore Prealpino) and the Hilly and Upper Plain Sector (Settore Collinare e di Alta Pianura) (Servizio Geologico d'Italia – ISPRA, 2021). The Alpine Sector, in the north of the Province, is formed mainly by metamorphic rocks (e.g., orthogneiss and paragneiss) and few Triassic sedimentary formations, and is crossed by a major E-W trending tectonic element (i.e., the so-called *Insubric Line*) separating the Central Alps basement nappes and the Southern Alps with a sequence of S-verging thrust faults (Laubscher, 1985). The Prealpine Sector extends from the Insubric Line to the Piedmont belt and is formed by metamorphic rocks (e.g., micascists and amphibolites) in the north and Triassic to Jurassic sedimentary formations in the remaining part (Bertotti et al., 1993). The Hilly and Upper Plain Sector goes from the Prealpine Sector to the Po Plain and is formed by recent sedimentary formations covered with Quaternary glacial deposits.

Numerous instability phenomena, of which 4881 landslides of different typology (Fig. 4.1c), affect the Province of Como causing frequent interruptions of the road viability with catastrophic consequences for the economy and society. Headlines of local newspapers often state "*Rocks, debris and mud blocking the SS340 Regina Vecchia* (i.e., a state road running along the W shore of Lake Como)", "*Landslides and mudslides on the beauties of Lake Como*", "*SP583 Lariana* (i.e., a provincial road connecting Como, Bellagio and Lecco along the S shore of Lake Como) *closed due to landslides*" (source: https://www.laprovinciadicomo.it).

---

[3] The contents of this Chapter are based on Nappo et al. (2021b).

The Italian national (ISPRA, 2021) and regional (PAI 2019 - Geoportale Regione Lombardia, 2021) landslide inventory maps classify most of these phenomena as slides (52.42%) and rapid flow (43.24%). Such inventories, introduced by the Italian Legislative Decree n.180/98 in 1998, are produced by i) investigating historical and archive documents, ii) interpreting high resolution aerial photographs, and iii) searching for geomorphological indicators of the slope instability during field investigations.

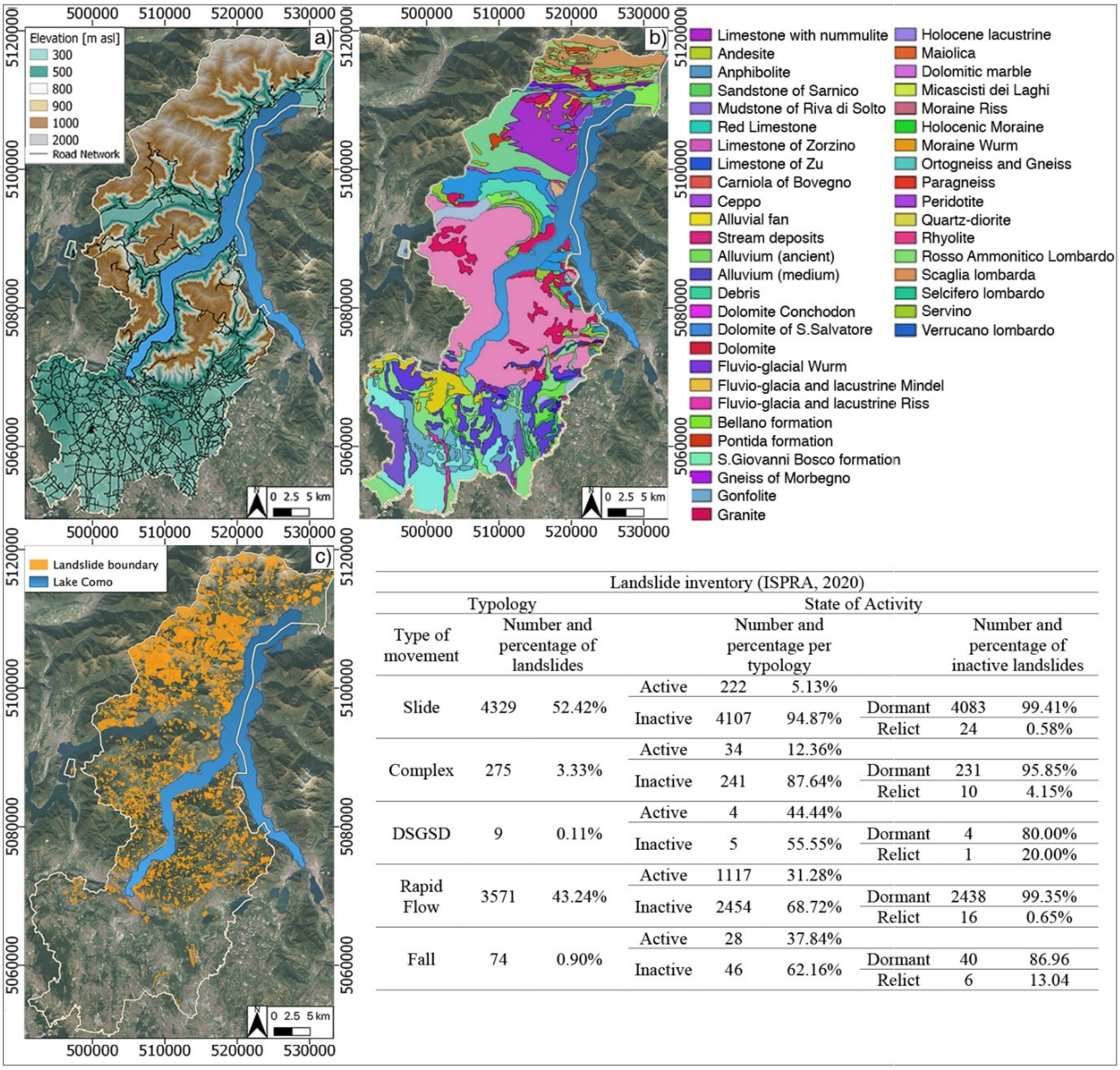

Landslide inventory (ISPRA, 2020)

| Typology | | | State of Activity | | | | | |
|---|---|---|---|---|---|---|---|---|
| Type of movement | Number and percentage of landslides | | Number and percentage per typology | | | Number and percentage of inactive landslides | | |
| Slide | 4329 | 52.42% | Active | 222 | 5.13% | | | |
| | | | Inactive | 4107 | 94.87% | Dormant | 4083 | 99.41% |
| | | | | | | Relict | 24 | 0.58% |
| Complex | 275 | 3.33% | Active | 34 | 12.36% | | | |
| | | | Inactive | 241 | 87.64% | Dormant | 231 | 95.85% |
| | | | | | | Relict | 10 | 4.15% |
| DSGSD | 9 | 0.11% | Active | 4 | 44.44% | | | |
| | | | Inactive | 5 | 55.55% | Dormant | 4 | 80.00% |
| | | | | | | Relict | 1 | 20.00% |
| Rapid Flow | 3571 | 43.24% | Active | 1117 | 31.28% | | | |
| | | | Inactive | 2454 | 68.72% | Dormant | 2438 | 99.35% |
| | | | | | | Relict | 16 | 0.65% |
| Fall | 74 | 0.90% | Active | 28 | 37.84% | | | |
| | | | Inactive | 46 | 62.16% | Dormant | 40 | 86.96 |
| | | | | | | Relict | 6 | 13.04 |

***Figure 4.1.*** *Modified from Nappo et al. (2021b). Geomorphological setting of the Province of Como (N Italy). a) Elevation map and road infrastructure network. b) Geological map (modified from Servizio Geologico d'Italia - ISPRA,2021). c) Landslide inventory map and frequency distribution of landslides typology and state of activity (modified from ISPRA, 2021). DSGSD stands for Deep Seated Gravitational Slope Deformation. Reference system: WGS84/UTM zone 32N.*

In a vulnerable territory as the Province of Como, the efficient management of transportation facilities (potentially) affected by landslides is fundamental to preserve the infrastructure's functionality and ensure the safety of road users (ANAS, 2004; Nappo et al., 2021b). Central in the vulnerability assessment of roadways exposed to landslide risk is therefore the objective and precise detection and classification of road pavement damage. Emerging techniques as the photogrammetric reconstruction of 3D models from RGB images collected by cameras mounted on Unmanned Aerial Vehicles (UAV) can facilitate the characterization of landslide-induced pavement damage for road operators, otherwise assessed via subjective visual inspections (Nappo et al., 2021b).

In this perspective, this research proposes a semi-automatic procedure combining 3D and 2D digital photogrammetry products reconstructed from UAV images to i) rapidly locate distressed parts of asphalt-paved roads affected by landslides, ii) objectively characterize longitudinal and transverse cracks induced by landslides on the road pavements, and iii) quantitatively classify the road damage severity using the International Roughness Index (IRI) (Nappo et al., 2021b). The aim is providing a standard workflow for road pavement inspections in landslide-affected areas for road maintenance agencies (Nappo et al., 2021b). Moreover, this research enhances our understanding of the effects of landslides on asphalt road pavements, thus assisting in the quantitative assessment of their consequences on the road network (Nappo et al., 2021b).

The procedure is applied to the provincial road SP14 in Laino municipality and the municipal road SC in Vercana municipality, both located in the Province of Como and known to be affected by slope instabilities (Martin et al., 2004; Nappo et al., 2021b).

Preliminarily, a correlation analysis between presence/absence of landslides and typical road damage typologies (see Tab. 2.1) observed on the pavements of the roads investigated in the Province of Como was performed, as reported in Table 4.1. The results indicated that longitudinal and transverse fractures of the asphalt road pavements can be attributed to the movements of landslides (Mavrouli et al., 2019; Nappo et al., 2019, 2021b). Other damage typologies, as fatigue cracks, are most likely caused by other factors than slope/ground instabilities (Nappo et al., 2021b).

***Table 4.1.*** *Modified from Nappo et al. (2021b). Typologies of road damage observed inside and outside landslide boundaries in the Province of Como.*

| | | **Inside a landslide** | | **Outside a landslide** | | |
|---|---|---|---|---|---|---|
| **Class of damage** | **Typology of damage** | **Number and frequency of locations** | | **Number and frequency of locations** | | **Total Number** |
| Cracking | Fatigue | 39 | 21% | 146 | 79% | 185 |
| | Block | 11 | 28% | 29 | 73% | 40 |
| | Longitudinal | 39 | 62% | 24 | 38% | 63 |
| | Transverse | 30 | 83% | 6 | 17% | 36 |
| | Edge | 11 | 14% | 66 | 86% | 77 |
| | Joint Reflection | - | - | 10 | 100% | 10 |
| | Slippage | 4 | 11% | 34 | 89% | 38 |
| Distortion | Rutting | 1 | 14% | 6 | 86% | 7 |
| | Shoving | - | - | - | - | - |
| | Depression | 5 | 50% | 5 | 50% | 10 |
| | Upheaval | - | - | - | - | - |
| Disintegration | Ravelling | 6 | 6% | 91 | 94% | 97 |
| | Potholes | - | - | 12 | 100% | 12 |

## 4.1 Materials

For this research, the topographic map (i.e., Carta Tecnica Regionale – CTR) at 1:10.000 scale and Digital Terrain Model (DTM) at 5 m resolution (Geoportale Regione Lombardia, 2021) of the Province of Como were adopted as basic information layers.

Geological and geomorphological maps at 1:10.000 scale were provided by the Servizio Geologico d'Italia (ISPRA, 2021) and Vercana municipal repository (Comune di Vercana, 2021), and used for the site-specific characterization of the investigated areas.

Landslide inventory maps were collected from the Italian national (Progetto IFFI - ISPRA, 2021) and regional (PAI 2019 - Geoportale Regione Lombardia, 2021) repositories, where location, shape, failure mechanism and state of activity of the slope instabilities are stored. The classification proposed by Cruden and Varnes (1996) is adopted here to catalogue the landslides' activity.

Field investigations were performed to i) evaluate the presence of landslides affecting the selected road sections via meso-structural analyses of bedding (in Laino) and metamorphic foliation (in Vercana), ii) measure the width of fractures on the investigated asphalt pavements, and iii) acquire RGB (5472 × 3078) images of the road pavements using a DJI Phantom4 PRO drone (Nappo et al., 2021b). The DJI Phantom4 PRO was operated in Positioning mode (P-mode) at 10 m from the road surface (Fig. 4.2a) and an average speed of 3 m/s to prevent impacts with the surrounding vegetation (Nappo et al., 2021b). The overall duration of each flight depends on the available set of batteries; by default, the DJI Phantom4 PRO can fly for approximately 30 min with a single set of batteries. The RGB (5472 × 3078) images of the road pavements were acquired in the nadir direction (Fig. 4.2a) on a regular acquisition grid (Fig. 4.2b), thus allowing an overlap of 80% between adjacent images (Nappo et al., 2021b). The camera (FC6310_8.8) is 20 mm wide with focal length of 10 mm acquiring images at 16.8 MP and Ground Sample Distance (GSD) of 0.37 cm/pixel (Nappo et al., 2021b). The acquired images were automatically geolocated by the satellite GPS system integrated in the DJI Phantom4 PRO with declared accuracy of ± 0.5 m in vertical and ± 1.5 m in horizontal positioning (Nappo et al., 2021b). For more specifics, please refer to the DJI webpage (https://www.dji.com/it/phantom-4-pro).

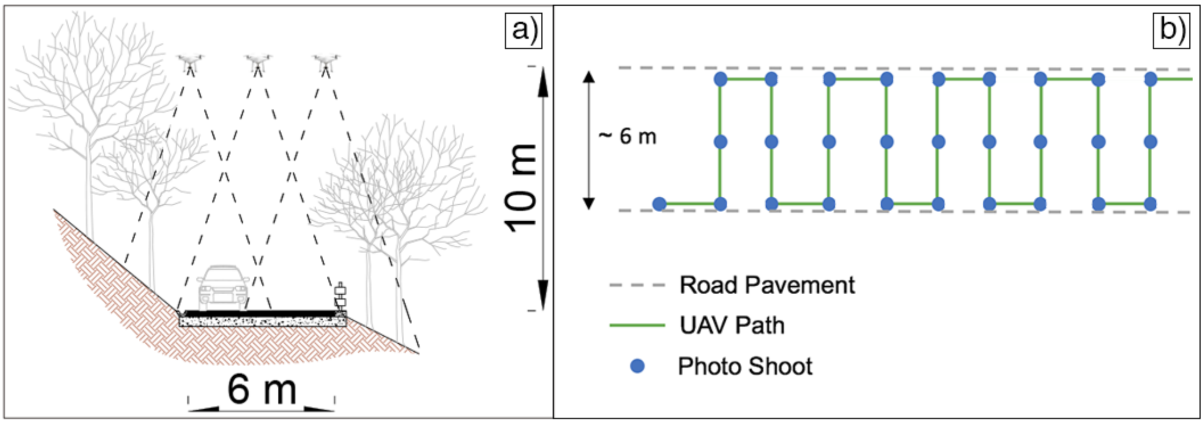

*__Figure 4.2.__ Modified from Nappo et al. (2021b). Scheme of the UAV acquisition in a) frontal and b) map view.*

## 4.2 Methodology

The detection and characterization of landslide-induced longitudinal and transverse cracks on asphalt-paved roads in the Province of Como was performed in three phases, as illustrated in Figure 4.3 (Nappo et al., 2021b).

*Phase I* is devoted to the reconstruction of the 3D point cloud of the investigated roads via Pix4D software. Such model is then processed in *Phase II* using MATLAB and CloudCompare software. In *Phase III*, algorithms for damage detection are applied to the 2D photogrammetry products using Python software, and all products are imported into GIS ArcMap software.

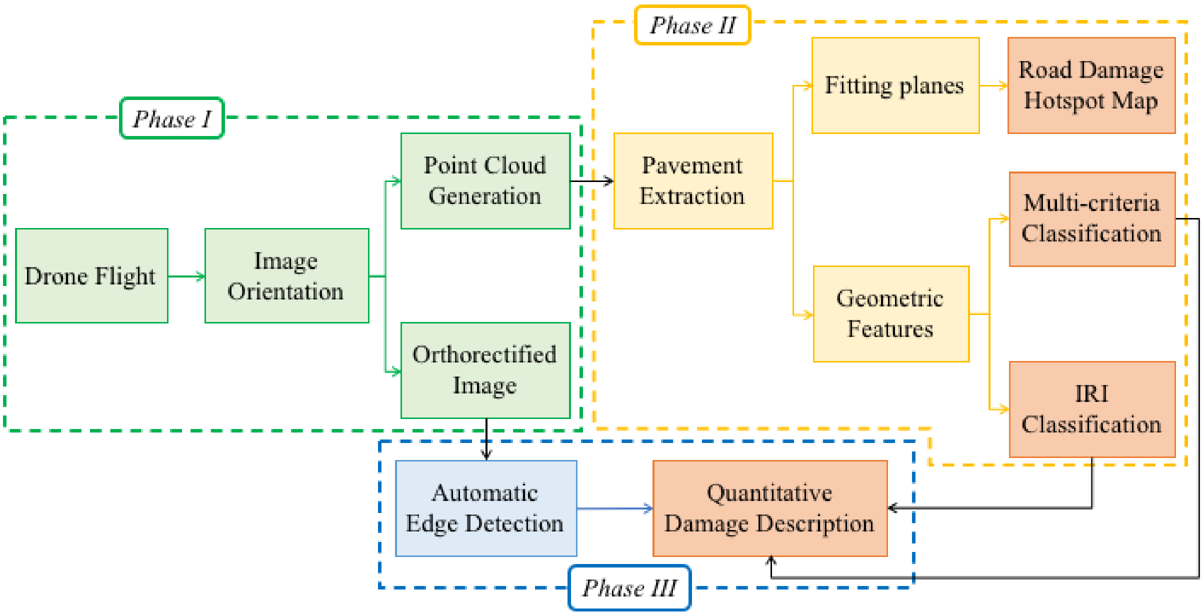

***Figure 4.3.*** *Modified from Nappo et al. (2021b). Flowchart of the proposed methodology.*

For each study area, the RGB images acquired with the DJI Phantom4 PRO were combined in *Phase I* using the Structure from Motion (SfM) photogrammetric technique, thus reconstructing a spatially oriented model of the investigated road section (Nex and Remondino, 2014). The SfM algorithm simultaneously estimates the interior and exterior camera parameters, detects keypoints in adjacent images to automatically match them, and determines the position and altitude of the camera using the GPS system integrated with the UAV (Nex and Remondino, 2014). This allows to automatically position and geolocate the 3D scene in the space (Nex and Remondino, 2014). The resulting products of *Phase I* were a 3D dense point cloud and a 2D ortho image of the scene. The 2D ortho image was used at this step to manually draw the fractures observed on the road pavement to validate the results of the following steps (Nappo et al., 2021b).

In *Phase II*, the road pavement was extracted from the original 3D point cloud and processed to compute i) the deviation of 3D points from a reference surface, and ii) the point cloud geometric features (i.e., omnivariance, verticality and roughness; Maas and Vosselman, 1999). A set of 6-by-1-m planes was progressively fitted to the road pavement in direction perpendicular to the road central line (Fig. 4.4a), thus generating the reference surface to calculate the vertical deviation of each 3D point (Nappo et al., 2021b). The resulting damage hotspot map allowed identifying irregular portions of the road pavement where distress was expected (Nappo et al, 2021b).

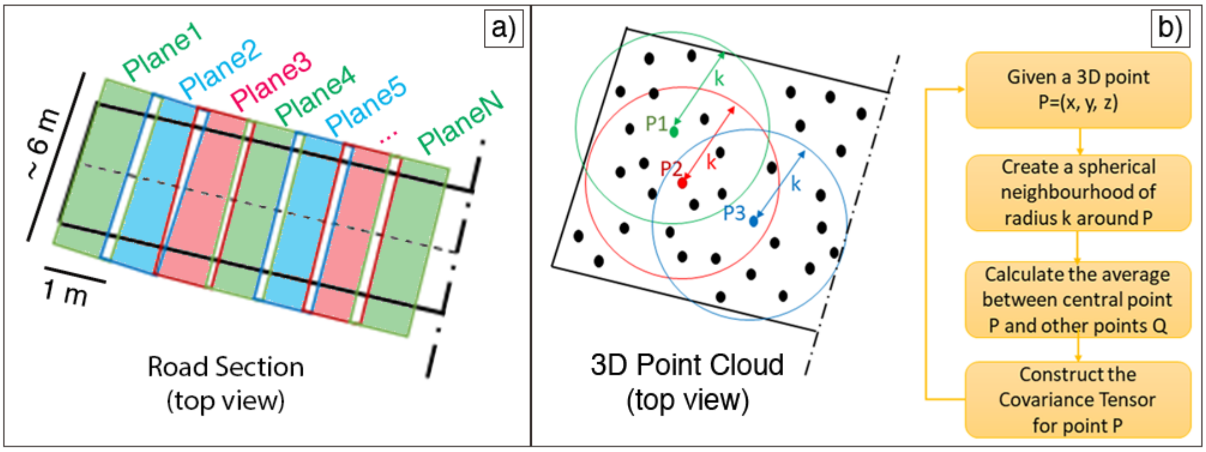

***Figure 4.4.*** *Modified from Nappo et al. (2021b). Processing schemes of Phase II. a) Set of planes progressively fitted to the road pavement and perpendicular to the road central line. b) Construction of spherical neighbourhoods around each 3D point and flowchart of the covariance matrix computation.*

Then, spherical neighbourhoods of different kernel sizes (Weinmann et al., 2013) were constructed around each 3D point (Fig. 4.4b) to compute its covariance matrix and obtain the following geometric features:

- Omnivariance (Hackel et al., 2016) describing the geometric (i.e., volumetric, surficial or linear) pattern of points into their local neighbourhood (Niemeyer et al., 2012). The kernel size (k) was set to 0.10 m to differentiate the points representing damage (with volumetric distribution) from the undamaged road surface (Nappo et al., 2021b).

- Verticality (Hackel et al., 2016) representing the height variations inside each neighbourhood (Weinmann et al., 2013). The kernel size was set to 0.02 m to maximize the distinction between damage (higher points) and road surface (Nappo et al., 2021b).
- Roughness (Kumar et al., 2015) expressing the irregularity of the road pavement. The kernel size was set to 0.20 m to determine uneven (i.e., damaged) and smooth points of the road surface (Nappo et al., 2021b).

Thresholds were imposed on the geometric features to train a multi-criteria binary classifier, able to discern presence from absence of damage on the road pavements (Nappo et al., 2021b). Specifically, a point was classified as *damage* when (Nappo et al., 2021b):

- Omnivariance (k = 0.10 m) > 1.15E-04 m
- Verticality (k = 0.02 m) > 0.12E-01 m & < 0.60E-01 m
- Roughness (k = 0.20 m) > 0.2E-02 m/km.

The 3D point clouds were also classified into four damage severity levels based on the IRI (e.g., Hatmoko et al., 2019; Yu et al., 2006) and determined as follows (Nappo et al., 2021b):

- D0 (Good) when IRI < 4 mm/m
- D1 (Fair) when 4 < IRI < 8 mm/m
- D2 (Damaged) when 8 < IRI < 12 mm/m
- D3 (Severely damaged) when IRI > 12 mm/m.

In *Phase III*, the algorithm proposed by Cubero-Fernandez et al. (2017) was applied to pre-process the ortho image of the road pavement produced in *Phase I*, and automatically perform the Canny edge detection (Canny, 1986) to identify asphalt road damage (Nappo et al., 2021b). To this aim, the ortho image was converted to its negative, the illumination enhanced with a logarithmic transformation to highlight pavement unevenness, and noise removed by smoothing the image with the Gaussian filter (Cubero-Fernandez et al., 2017). Then, damage edges were detected by applying the Canny algorithm (Canny, 1986) and refined using the closing morphological operator (Nappo et al., 2021b). The Ramer-Douglas-Peucker algorithm (Douglas and Peucker, 1973; Ramer, 1972) was applied to simplify the boundaries of the 2D damage edges that were then imported into GIS and overlaid with the 3D point cloud (Nappo et al., 2021b). The combination of 2D damage polygons and 3D point cloud allowed to associate geometric (e.g., width and area) and photogrammetric (i.e., density of points, omnivariance, verticality, roughness) information to each fracture (Nappo et al., 2021b). Based on the multi-criteria classification and average roughness (from IRI classification) of the points contained into the damage polygons, the road damage was rated according to its damage/non-damage ratio and severity (from D0 to D3 – Nappo et al., 2021b).

## 4.3 Study areas: SP14 – Laino and SC – Vercana

The provincial road SP14 connects the municipalities of Laino and Ponna in the mountainous valley called "Val d'Intelvi" (Nappo et al., 2021b – Fig. 4.5a). The territory is formed mainly by Sinemurian – Lower Pliensbachian Moltrasio limestone (MOT), consisting of grey limestone in well-defined beds of 5-70 cm thickness with chert in nodules or discontinuous bands, and Late Pleistocene glacial deposits (LNC; Lakes Supersynthem – Cantù Synthem) of overconsolidated non-cohesive granular material in layers of 10-20 m thick massive coarse gravels alternated with clayey silt and limited sand (Bini et al., 1996; Michetti et al., 2014b; Nangeroni, 1969; Pracchi, 1954 – Fig. 4.5b and c). The investigated section (200 m) of the SP14 in the proximity of Laino municipality, crosses an extended unstable slope characterized by two slides (L1 and L2 in Fig. 4.5b) moving along the MOT discontinuities (Nappo et al., 2021b). The sharp-edge blocks of MOT slide on top of each other of 20-30 cm and are partially covered by 50-70 cm thickness of lawn (Fig. 4.5d). The L2 slide tentatively mapped in Figure 4.5b was detected during field investigations in March 2020 and June 2021, when extensive damage (i.e., cracks and deformations of the asphalt pavement and displaced edging curbs) was observed along the SP14 – Laino (Fig. 4.5e-g). The uphill curbs delimiting the SP14 roadway are tilted, and those posed downhill are displaced of 8 cm in vertical and 4 cm in horizontal directions (Nappo et al., 2021b – Fig. 4.5g). Two UAV flights were performed in this area: the first at 10 m acquiring 371 (5472x3078) RGB images of the SP14 roadway, and the second at 30 m acquiring additional 492 images of the entire area.

The municipal road SC – Vercana in the northern sector of Lake Como connects the localities of Piazzo and Pighè within the municipality (Nappo et al., 2021b – Fig. 4.6a). Migmatitic gneiss (Penninic Unit) and quartz-diorite of Mount Bassetta (Serizzo – Unit of Val Masino – Bregaglia – Iorio) form the substrate of the area, covered by 1-2 m thickness of Quaternary eluvial and glacial deposits (Comune di Vercana, 2021 – Fig. 4.6b-d). The substrate outcropping along the SC – Vercana is highly fractured and oriented dip-slope (Fig. 4.6e), with foliation planes oriented as Riedel shear structures with respect to the Insubric Line. The investigated section

(700 m) of the SC – Vercana crosses four slides (from V1 to V4 in Fig. 4.6b) and is extensively damaged (i.e., cracks and deformations of the asphalt pavement, ditch and curbs – Fig. 4.6f and g), as observed during the field investigations in June 2021. At the intersection with the V2 slide, 78.70 m of the roadway are unpaved (Fig. 4.6h) and gabions, rockfall barriers and hydraulic structures for surficial water outflow have been placed (Nappo et al., 2021b). In this area, 1209 (5472x3078) RGB images were acquired with the DJI Phantom4 PRO.

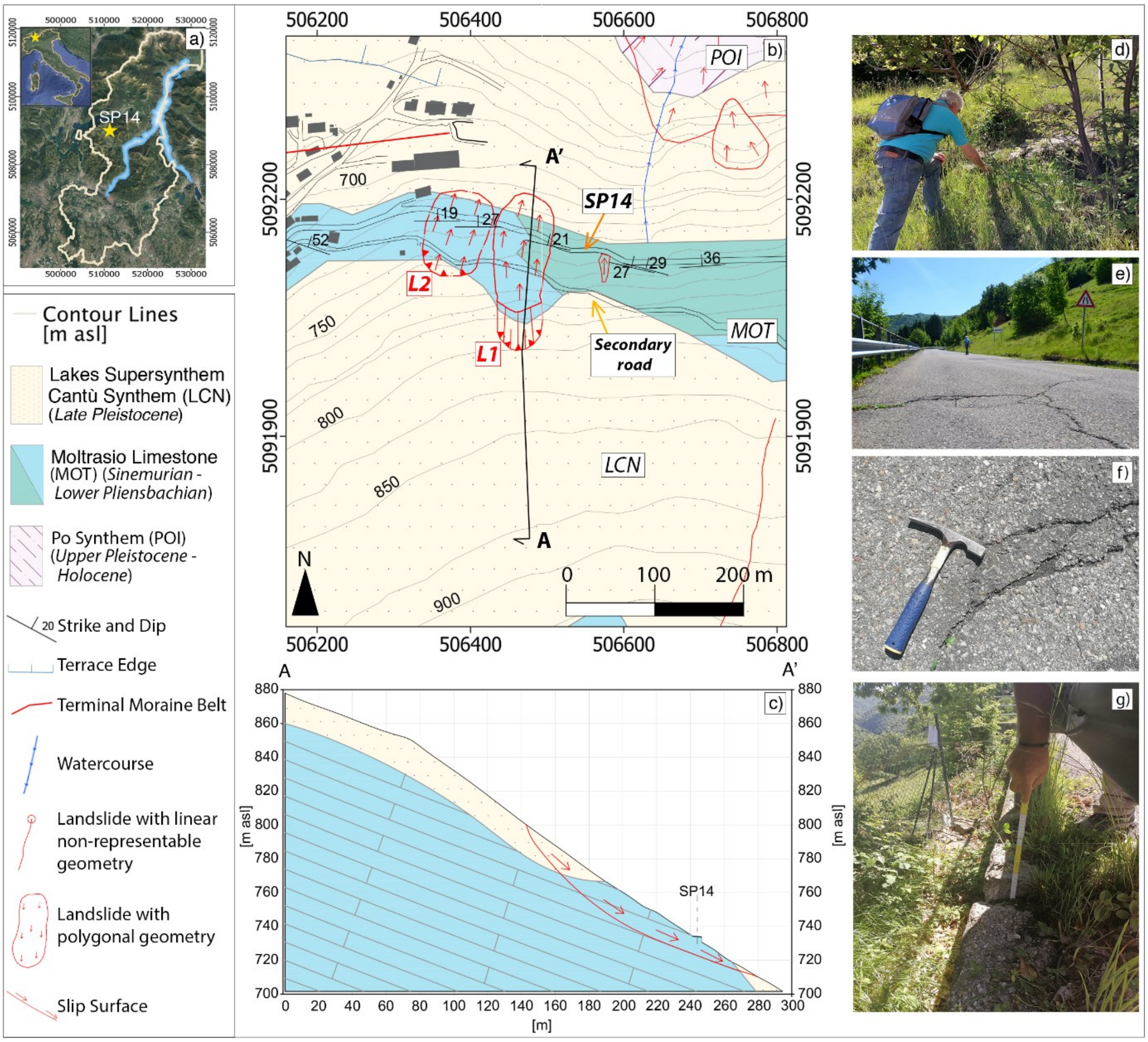

***Figure 4.5.*** *Modified from Nappo et al. (2021b). a) Location of the SP14 – Laino in the Province of Como. Geological and geomorphological b) map and c) cross section A-A' (modified from Michetti, 2014a). d) Outcropping blocks of Moltrasio limestone (MOT) sliding 20-30 cm on top of each other and partially covered by 50-70 cm thickness of lawn. e) and f) Deformation and crack on the asphalt road pavement. g) Misplaced curb with 8 cm vertical and 4 cm horizontal movements. Reference system: WGS84/UTM zone 32N.*

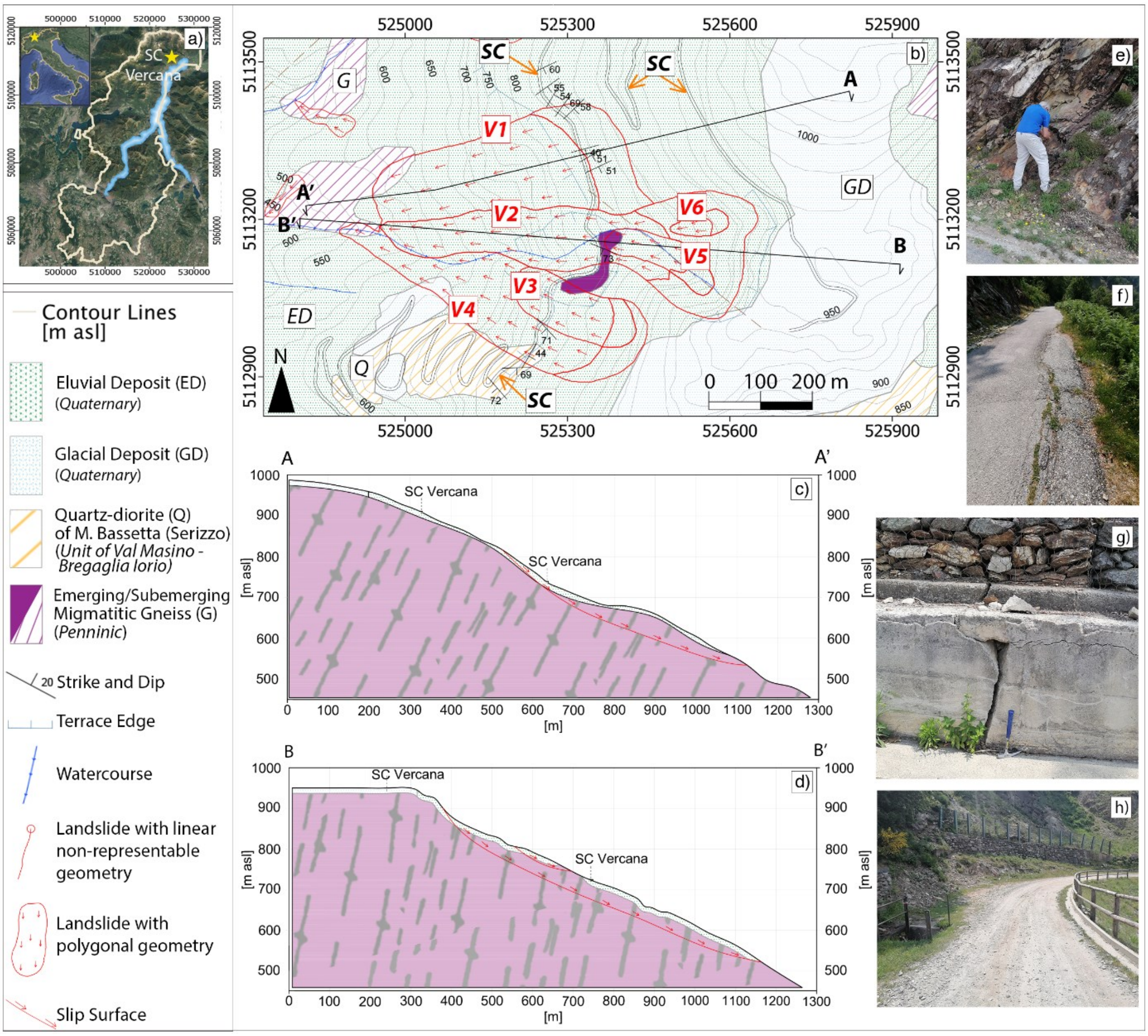

*Figure 4.6.* *Modified from Nappo et al. (2021b). a) Location of the SC - Vercana. b) Geological and geomorphological map (modified from Comune di Vercana, 2021). Geological cross sections c) A-A' and d) B-B' (modified from Comune di Vercana, 2021). e) Outcropping highly fractured gneiss with foliation planes oriented as Riedel shear structures with respect to the Insubric Line. f) Deformation and crack along the roadway. g) Fracture in the concrete retaining wall. h) View of the V2 landslide with unpaved road surface. Reference system: WGS84/UTM zone 32N.*

Finally, Table 4.2 summarizes the main characteristics of the slides affecting the investigated sections of the SP14 – Laino and the SC – Vercana.

***Table 4.2.*** *Modified from Nappo et al. (2021b). Characteristics of the slides affecting SP14 – Laino (200 m) and SC – Vercana (700 m) (modified from ISPRA, 2021 and PAI, 2019).*

| Study Area | ID Landslide | State of activity | Perimeter [m] | Area [$m^2$] | Volume [$m^3$] | Width [m] | Length [m] |
|---|---|---|---|---|---|---|---|
| SP14 – Laino | L1 | Inactive | 422 | 9,315 | 57,588 | 51 | 135 |
| | L2 | - | 268 | 4,710 | - | 61 | 93 |
| SC – Vercana | V1 | Inactive | 1,715 | 69,451 | 1,193,116 | 168 | 465 |
| | V2 | Active | 2,864 | 77,366 | 1,231,459 | 101 | 660 |
| | V3 | Inactive | 772 | 18,871 | 186,229 | 90 | 236 |
| | V4 | Inactive | 1,840 | 63,909 | 1,372,024 | 167 | 557 |
| | V5 | Active | 625 | 10,494 | 69,731 | 53 | 219 |
| | V6 | Active | 351 | 3,483 | 10,755 | 38 | 103 |

## 4.4 Results

This section presents the results obtained by applying the methodology described in *Section 4.2* to the SP14 – Laino and SC – Vercana in the Province of Como described in *Section 4.3*.

### 4.4.1 Provincial road SP14 - Laino

Figure 4.7 shows the 3D point cloud of the SP14 – Laino (Fig. 4.7a and b) and the 2D ortho image of the whole surveyed area (Fig. 4.7c) reconstructed in *Phase I.*

Eighteen (18) longitudinal and 8 transverse cracks were manually detected from the 2D ortho image of the SP14 – Laino (Fig. 4.8). Within the boundaries of L1 and L2 slides, the 15 (out of 18) longitudinal cracks have width varying from 0.32 to 3.50 cm, while the 8 transverse cracks are in the range of 0.76-2.63 cm (Nappo et al., 2021b). Here, a fatigue crack wide 0.95 cm was also detected at the E side of the road evolving outside the L1 slide (Nappo et al., 2021b). Additional 13 longitudinal, 9 transverse and 2 fatigue cracks were detected inside the L1 and L2 slides on the pavement of the secondary road located southern (i.e., uphill) than the SP14 (Fig. 4.8). However, this road section was not further investigated because its 3D point cloud, reconstructed from the images acquired at 30 m of altitude, has a lower resolution compared to model of the SP14 (Nappo et al., 2021b).

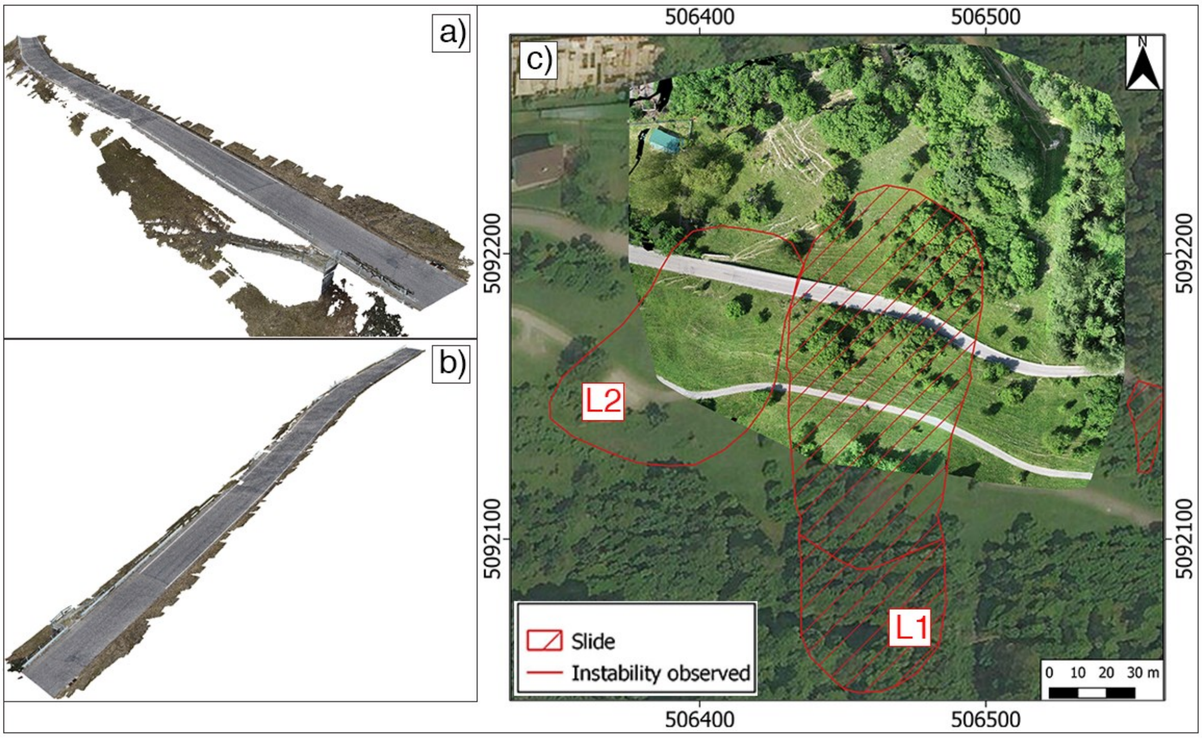

***Figure 4.7.*** *Modified from Nappo et al. (2021b). a) and b) Axonometric views of the 3D point cloud of the SP14 – Laino reconstructed via SfM. c) Top view of the 2D ortho image of the investigated area reconstructed via SfM. Reference system: WGS84/UTM zone 32N.*

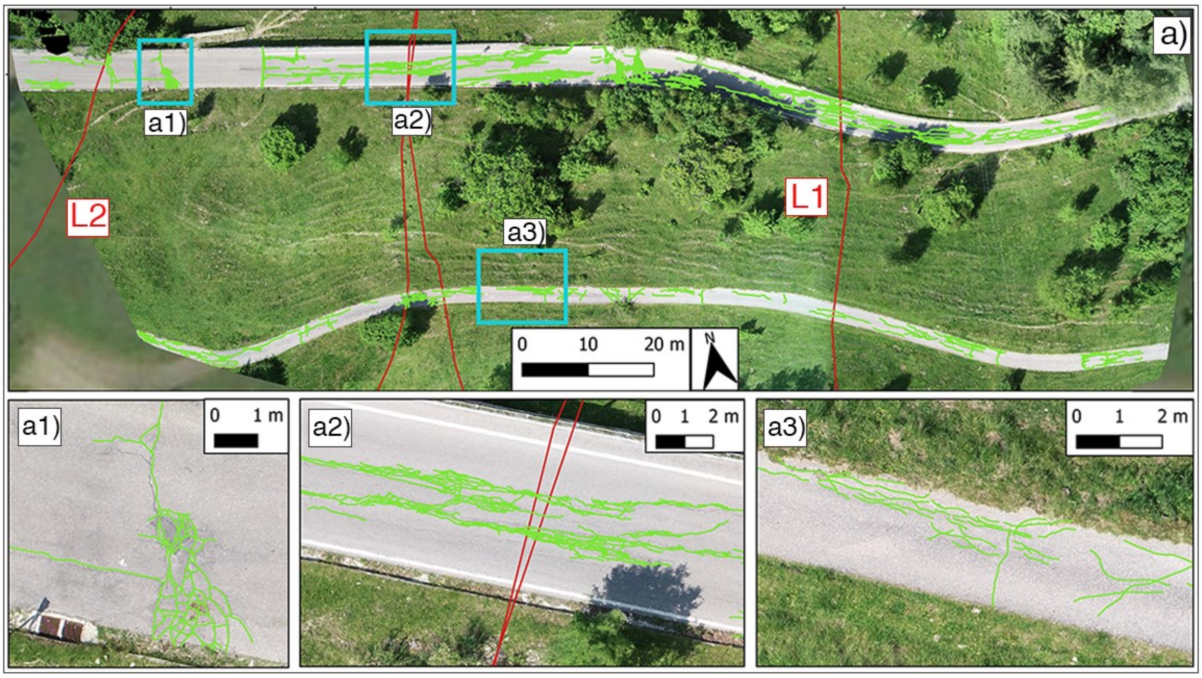

***Figure 4.8.*** *Modified from Nappo et al. (2021b). Manual detection from the 2D ortho image of 26 longitudinal and transverse cracks along the SP14 – Laino, and other 24 fractures (longitudinal, transverse and fatigue cracks) along the uphill secondary road.*

In *Phase II*, the computation of the Euclidean distance of each 3D point of the road pavement from the reference surface (Fig. 4.9a) highlighted deviations of about ± 5 cm (positive in red and negative in blue) where longitudinal and transverse cracks were previously observed (see Fig. 4.8 for comparison) (Nappo et al., 2021b). These hotspots suggest that the asphalt road pavement deforms heterogeneously under the effects of landslides (Nappo et al., 2021b).
As for the point cloud geometric features, longitudinal and transverse cracks wider that 1 cm were distinguished from the undamaged road surface by high values of omnivariance (Fig. 4.9b), verticality (Fig. 4.9c) and roughness (Fig. 4.9d). Noticeably, although out of the scope of this research, omnivariance and roughness also detected the fatigue crack at the E edge of the L1 slide (Nappo et al., 2021b). Boundary effects and noise are visible at the E side of the road section, thus limiting the distinction of damage typologies (Nappo et al., 2021b).

Figure 4.10 shows the classification of the 3D point cloud using the multi-criteria (i.e., presence or absence of damage by thresholding the geometric features) and IRI-based classifiers (i.e., severity levels from D0 to D3 according to the roughness). Longitudinal and transverse cracks wider than 1 cm were detected by the multi-criteria classifier (Fig. 4.10a) but constrained better by the IRI-based classifier using a higher threshold on the roughness (Nappo et al., 2021b – Fig. 4.10b). Similarly, fatigue cracks are well discernible in Figure 4.10. Smaller fractures were detected as few disperse points and therefore considered as errors of the classifiers (Nappo et al., 2021b). Noises and boundary effects in the geometric features (see Fig. 4.9) affected these classifications, thus detecting points of false damage and/or severity (i.e., false positive).

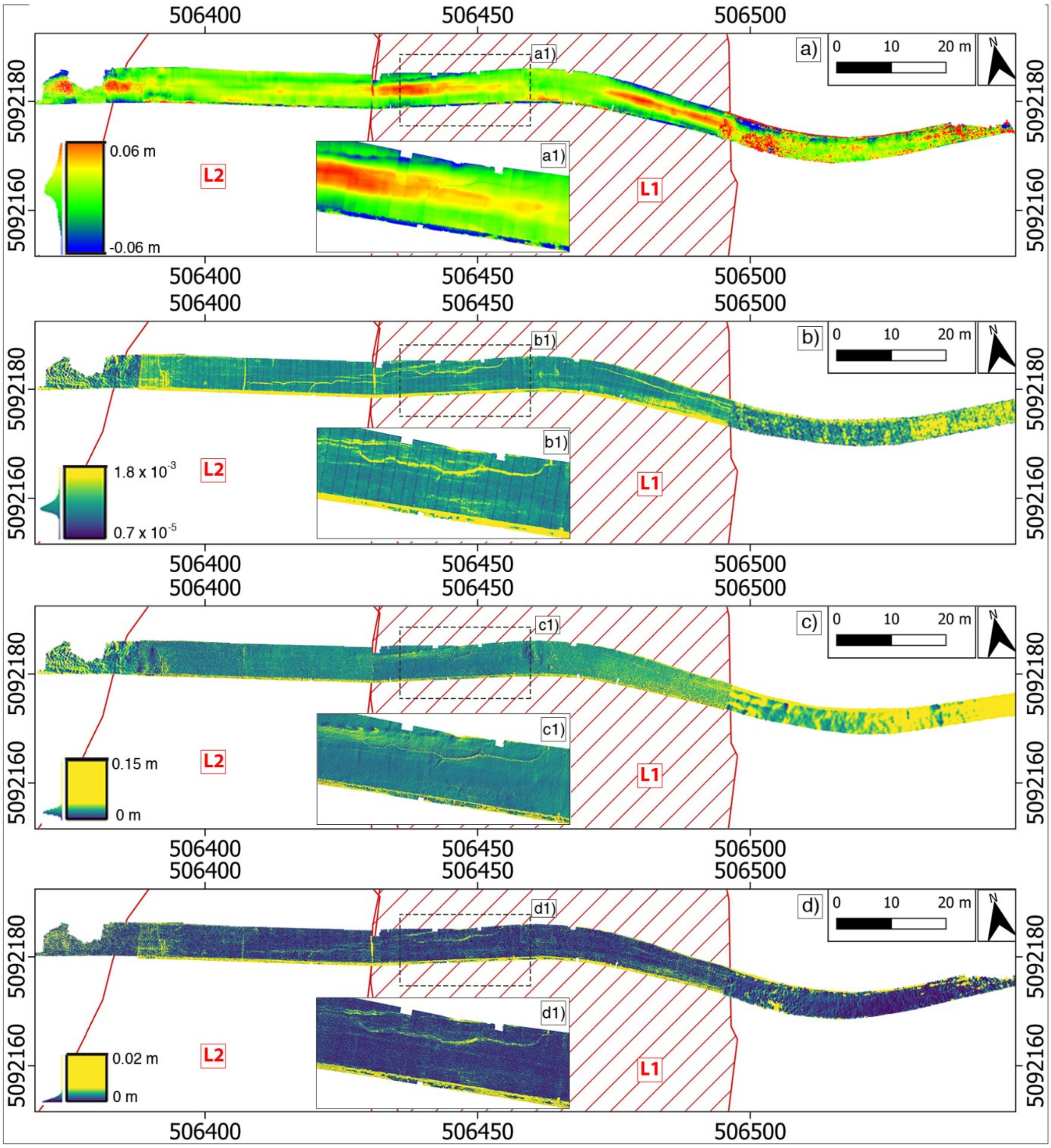

***Figure 4.9.*** *Modified from Nappo et al. (2021b). a) Distance from the planar reference road surface, b) Omnivariance, c) Verticality and d) Roughness computed for the SP14 – Laino. Reference system: WGS84/UTM zone 32N.*

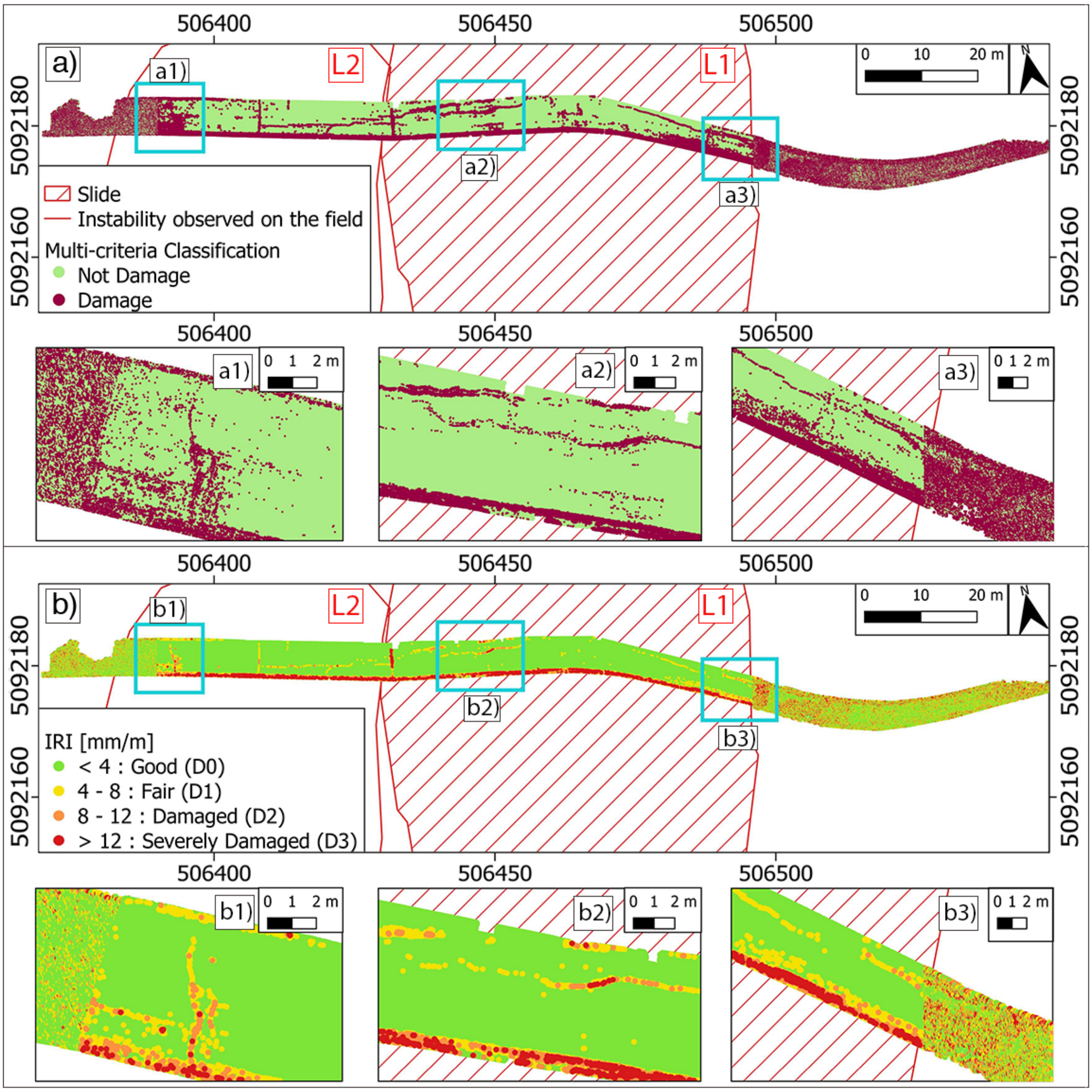

***Figure 4.10.*** *Modified from Nappo et al. (2021b). a) Multi-criteria and b) IRI severity classification of the SP14 – Laino point cloud. False positives are labelled as D3 at the southern edge of the road, where the concrete ditch is located. Noises and boundary effects are visible at the E side of the road, outside the L1 slide boundary. Reference system: WGS84/UTM zone 32N.*

The automatic road damage detection performed in *Phase III*, identified 6 longitudinal and 4 transverse cracks inside L1 and L2 slides boundaries, and 2 longitudinal and 1 fatigue cracks outside the slides (Nappo et al., 2021b – Fig. 4.11). The performance of the classifiers is related to the GSD of the input images (see Section 4.4.3 for specifications).

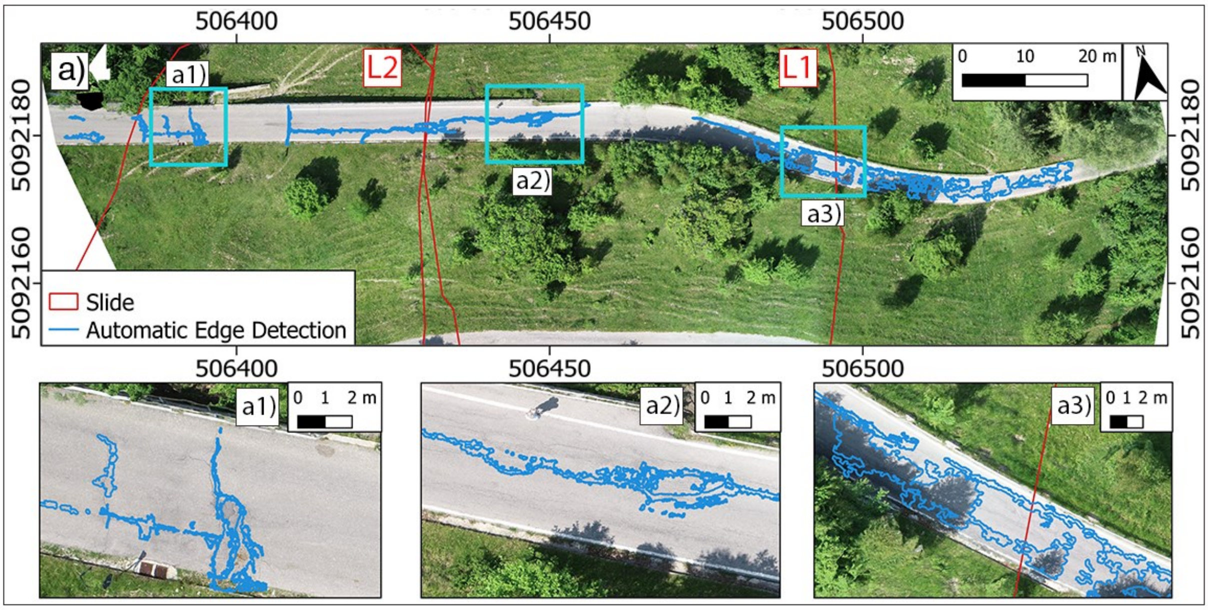

***Figure 4.11.*** *Modified from Nappo et al. (2021b). Automatic damage detection on the asphalt road pavement of SP14 – Laino. Reference system: WGS84/UTM zone 32N.*

The damage polygons shown in Figure 4.11 were imported into GIS to determine their width and area and compare them with real values measured in the field (Tab. 4.3). Fatigue cracks were discarded from this analysis because out of the scope of this research (Nappo et al., 2021b). Longitudinal and transverse cracks have average width of 2.03 cm, and average error between automatic and real area values of 1.94 $m^2$ due to the inability of the automatic algorithm in detecting the fractures' real width (Nappo et al., 2021b – Tab. 4.3).

***Table 4.3.*** *Modified from Nappo et al. (2021b). Automatic damage characterization for SP14 - Laino. The acronyms LC, TC and FC stand respectively for longitudinal, transverse and fatigue crack.*

| **ID Landslide** | **ID Damage** | **Damage Type** | **Width [cm]** | **Automatic Area [$m^2$]** | **Measured Area [$m^2$]** | **Error [$m^2$]** |
|---|---|---|---|---|---|---|
| | **1** | LC | 3.50 | 0.48 | 0.58 | 0.10 |
| | **2** | LC | 1.02 | 3.11 | 0.28 | 2.83 |
| **L2** | **3** | TC | 1.75 | 1.71 | 0.52 | 1.18 |
| **L2** | **4** | LC | 1.00 | 0.38 | 0.04 | 0.34 |
| **L2** | **5** | TC | 1.90 | 0.63 | 0.09 | 0.54 |
| **L2** | **6** | LC | 1.27 | 0.73 | 0.05 | 0.68 |
| **L2** | **7** | TC | 3.63 | 3.19 | 1.47 | 1.72 |
| **L2** | **8** | TC | 1.90 | 0.91 | 0.41 | 0.50 |
| **L2** | **9** | LC | 1.59 | 6.20 | 2.04 | 4.16 |

| | | | | | | |
|---|---|---|---|---|---|---|
| **L1** | **10** | LC | 2.69 | 8.74 | 6.00 | 2.74 |
| **L1** | **11** | LC | 1.82 | 7.25 | 2.91 | 4.34 |
| | **12** | FC | 1.00 | 80.72 | - | - |
| **L1** | **13** | LC | 2.28 | 4.72 | 0.46 | 4.27 |

When overlaid with the 3D point cloud, the 2D damage polygons were classified according to the ratio between damage and non-damage points derived from the multi-criteria classification (Tab. 4.4), and the IRI-based damage severity levels (Tab. 4.5). Longitudinal and transverse cracks with highest damage ratio (i.e., 2.97 and 2.93 respectively - Tab. 4.4) are located at the W edge of L2 slide, where boundary effects are visible (see Fig. 4.11 for comparison). As a cascading effect, the damage rating in Table 4.4 is conditioned by the accuracy of the multi-criteria classifier that, at this stage, can only give a first suggestion on the extent of road damage in landslide areas (Nappo et al. 2021b).

***Table 4.4.*** *Modified from Nappo et al. (2021b). Rating of damage extent on the SP14 – Laino using the multi-criteria binary classifier.*

| **Multi-criteria binary classifier** | | | | | |
|---|---|---|---|---|---|
| **ID Landslide** | **ID Damage** | **Density of damage points [No/m$^2$]** | **Density of non-damage points [No/m$^2$]** | **Damage ratio** | **Rating** |
| | **1** | 69 | 239 | 0.29 | **VIII** |
| | **2** | 227 | 76 | 2.97 | **II *** |
| **L2** | **3** | 261 | 89 | 2.93 | **III *** |
| **L2** | **4** | 124 | 239 | 0.52 | **VI** |
| **L2** | **5** | 73 | 303 | 0.24 | **IX** |
| **L2** | **6** | 131 | 236 | 0.55 | **V** |
| **L2** | **7** | 113 | 222 | 0.51 | **VII** |
| **L2** | **8** | 32 | 313 | 0.10 | **X** |
| **L2** | **9** | 29 | 374 | 0.08 | **XII** |
| **L1** | **10** | 34 | 366 | 0.09 | **XI** |
| **L1** | **11** | 26 | 340 | 0.07 | **XIII** |
| | **12** | 289 | 47 | 6.09 | **I *** |
| **L1** | **13** | 134 | 166 | 0.81 | **IV** |

Longitudinal and transverse cracks were then ranked from D0 to D3 (Tab. 4.5 and Fig. 4.12) adopting the damage severity classification based on fractures' average roughness (IRI). As shown in Table 4.5 and Figure 4.12, D2 is the most frequent severity level in L2 slide, and D3 the most frequent in L1 slide (Nappo et al., 2021b).

***Table 4.5.*** *Modified from Nappo et al. (2021b). IRI-based classification of damage on the SP14 – Laino.*

| | | IRI classifier | | | Roughness | | | |
|---|---|---|---|---|---|---|---|---|
| **ID Landslide** | **ID Damage** | **Number of points** | | | **Mean (μ)** | **St. Dev. (σ)** | **CV (= σ/μ)** | **Overall severity** |
| | | **D1** | **D2** | **D3** | | | | |
| | **1** | 51 | 21 | 38 | 7.46 | 6.67 | 0.89 | **D1** |
| | **2** | 310 | 116 | 74 | 5.07 | 4.11 | 0.81 | **D1** |
| **L2** | **3** | 185 | 73 | 13 | 8.31 | 3.08 | 0.37 | **D2** |
| **L2** | **4** | 30 | 6 | 0 | 4.16 | 3.35 | 0.80 | **D1** |
| **L2** | **5** | 88 | 29 | 6 | 4.28 | 2.26 | 0.51 | **D1** |
| **L2** | **6** | 129 | 36 | 13 | 6.94 | 3.06 | 0.44 | **D1** |
| **L2** | **7** | 0 | 37 | 150 | 8.42 | 3.13 | 0.37 | **D2** |
| **L2** | **8** | 128 | 75 | 40 | 8.46 | 3.66 | 0.43 | **D2** |
| **L2** | **9** | 263 | 102 | 202 | 11.41 | 7.50 | 0.65 | **D2** |
| **L1** | **10** | 338 | 84 | 263 | 13.44 | 11.00 | 0.81 | **D3** |
| **L1** | **11** | 127 | 6 | 0 | 5.42 | 1.21 | 0.22 | **D1** |
| | **12** | 51 | 21 | 38 | 12.40 | 12.72 | 1.02 | **D3** |
| **L1** | **13** | 310 | 116 | 74 | 22.76 | 19.43 | 0.85 | **D3** |

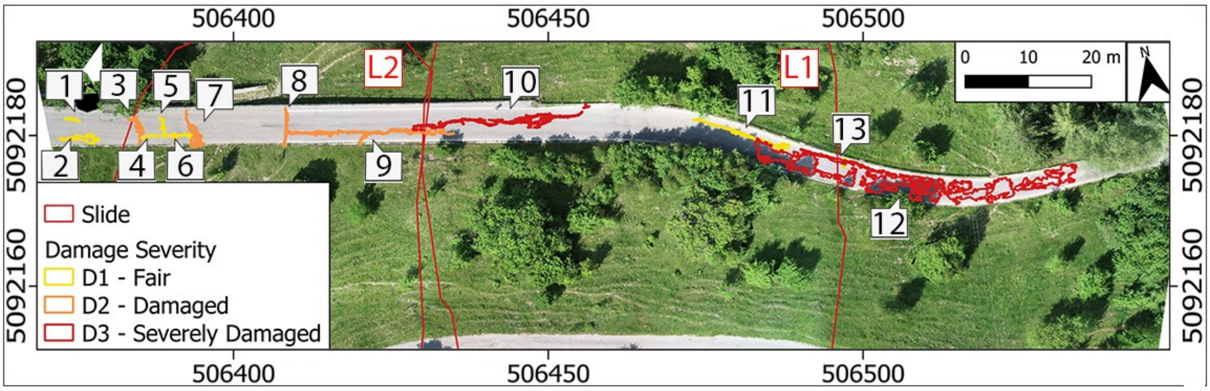

***Figure 4.124.*** *Modified from Nappo et al. (2021b). IRI-based severity classification of 2D automatic damage polygons of SP14 – Laino. The numeration from 1 to 13 refers to the ID Damage reported in Table 4.5. Reference system: WGS84/UTM zone 32N.*

### 4.4.2 Municipal road SC – Vercana

Figure 4.13 shows the 2D ortho image of the SC – Vercana, obtained from the SfM 3D model reconstruction of *Phase I*, overlaid with the fractures determined manually (Fig. 4.13a-c) and automatically via edge detection of *Phase III* (Fig. 4.13d-f) – the latter reported here for convenience. The manual approach identified 28 longitudinal cracks of width between 0.37 and 3.59 cm, 21 transverse cracks wide 0.32-2.71 cm, 8 edge cracks wide 0.32-0.97 cm, and 27 fatigue cracks of 0.97-2.85 cm width (Nappo et al., 2021b). Using the automatic algorithm, 1 depression, 16 longitudinal, 11 transverse cracks and 17 fatigue cracks were detected; the latter encompassing multiple damage typologies (Nappo et al., 2021b). No damage could be detected on the unpaved section (78.70 m) of the SC – Vercana crossing the V2 slide.

The highest deviations of the 3D points from the reference surface (Fig. 4.14a-c) detected in *Phase II* reach ± 5 cm (positive in red and negative in blue) where longitudinal and transverse cracks are wider than 2 cm (e.g., Fig. 4.14a), the roadway is unpaved (Fig. 4.14b), and fractures are highly interconnected (e.g., Fig. 4.14c) (Nappo et al., 2021b). The thresholding applied to the geometric features (i.e., omnivariance, verticality and roughness) allowed to retrieve the multi-criteria (Fig. 4.14d-f) and IRI-based classifications (Fig. 4.14g-i) of the 3D point cloud. As seen for the SP14 – Laino, longitudinal and transverse cracks wider than 1 cm are successfully detected by the multi-criteria classifier but constrained better by the IRI-based classifier (Nappo et al., 2021b). Given their extension, fatigue cracks are detected by both classifiers. Noises (e.g., ditch, curbs, unpaved road surface) and boundary effects are observed also in this case, thus determining numerous false positives (Nappo et al., 2021b).

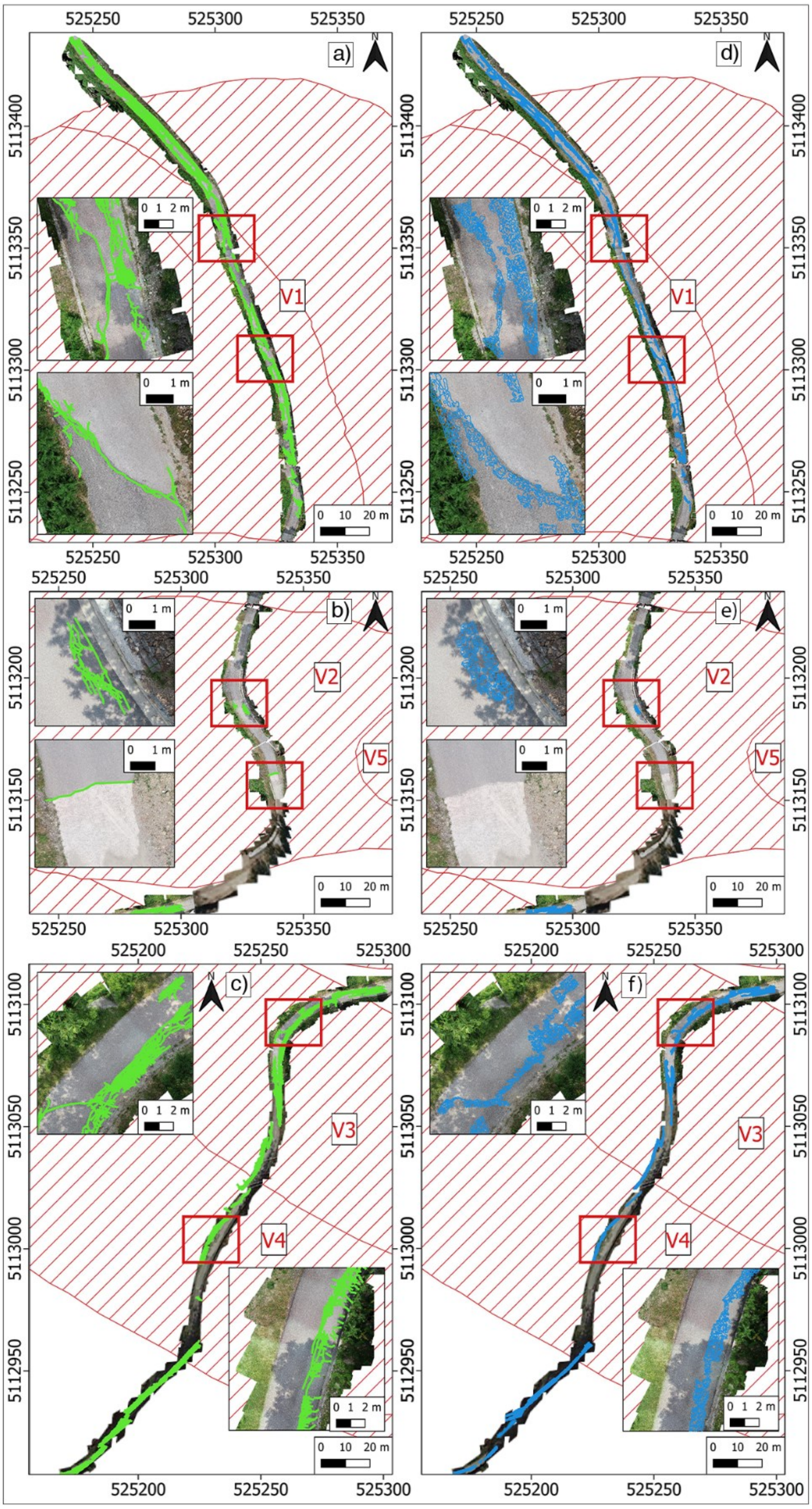

***Figure 4.13.*** *From Nappo et al. (2021b). Ortho image of SC – Vercana overlaid with a), b) and c) manual damage, and d), e) and f) automatically detected damage. The road pavement crosses V1 slide in a) and d); the V2 slide in b) and e); the V3 and V4 slides in c) and f). Reference system: WGS84/UTM zone 32N.*

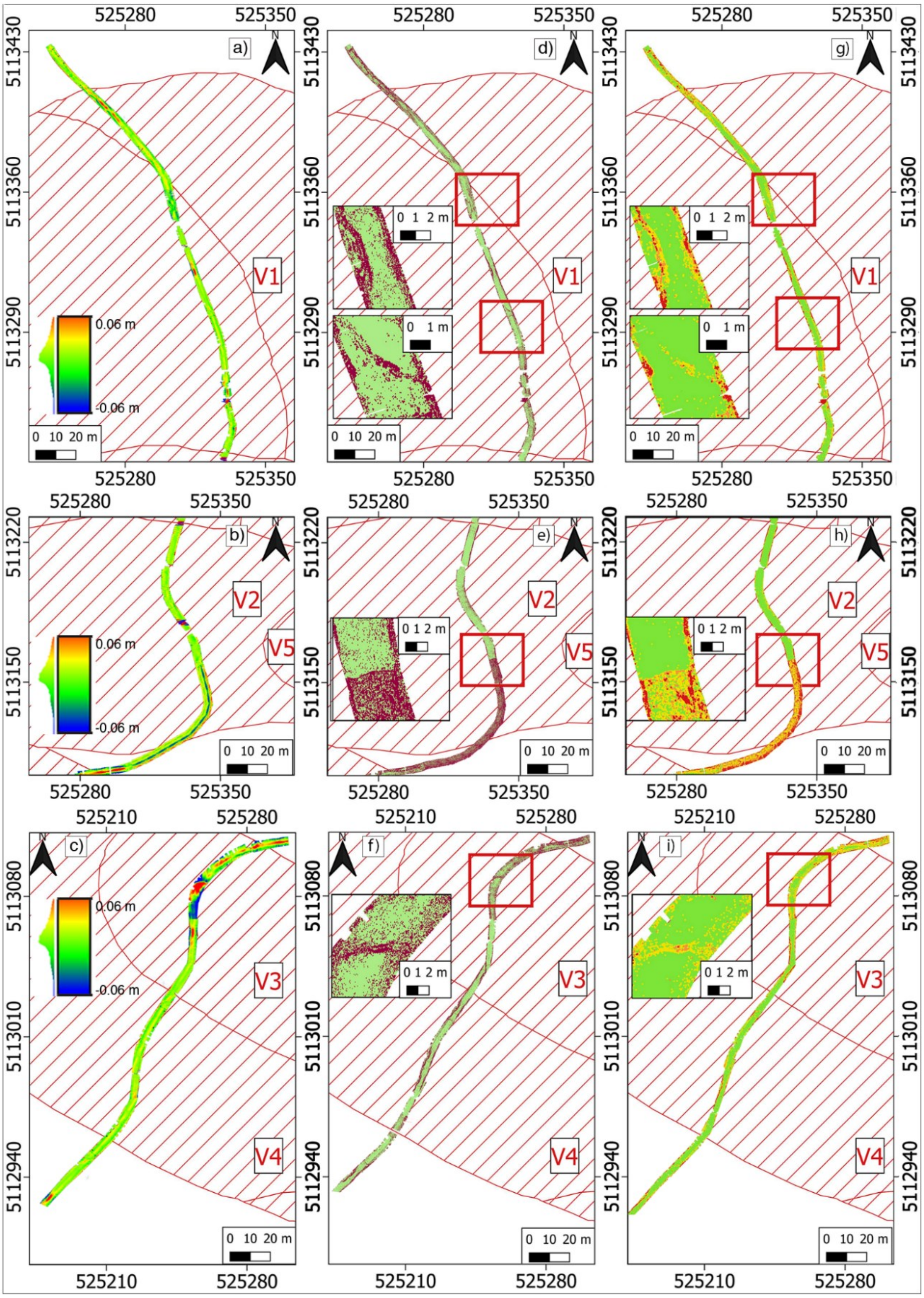

*Figure 4.14. Modified from Nappo et al. (2021b). Results for the SC – Vercana. a), b) and c) Road damage hotspot map. d), e) and f) Multi-criteria classification. g) h) and i) IRI-based severity classification. The road pavement crosses V1 slide in a), d) and g); the V2 slide in b), e) and h); the V3 and V4 slides in c), f) and i). Reference system: WGS84/UTM zone 32N.*

Table 4.6 reports the comparison between the area of fractures measured on the field and those obtained from the 2D automatic damage polygons (Fig. 4.13d-f). Longitudinal and transverse cracks have average width of 1.73 cm. As for the SP14 – Laino, the average error between automatic and real area values is 1.84 $m^2$ (Nappo et al., 2021b – Tab. 4.6). Fatigue cracks were discarded from this analysis because out of the scope of this research (Nappo et al., 2021b).

The classifications of 2D damage polygons according to the ratio between damage and non-damage points (i.e., multi-criteria classifier), and their average roughness (i.e., IRI-based severity levels) are reported in Tables 4.7 and 4.8 respectively. As mentioned for the case of SP14 – Laino, these results are conditioned by the accuracy of the edge detection and the classifiers (Nappo et al., 2021b).

Figure 4.15 shows the 2D damage polygons classified from D0 to D3 according to their IRI-based severity (Nappo et al., 2021b). Here, 1 polygon is severely damaged (D3), 9 are damaged (D2), 28 are fair (D1) and 14 are good (D0), rendering D1 the most frequent severity level inside the slides and D0 outside (Nappo et al., 2021b).

***Table 4.6.*** *Modified from Nappo et al. (2021b). Automatic damage characterization for SC – Vercana. The acronyms LC, TC and FC stand respectively for longitudinal, transverse and fatigue crack; D_D stands for depression.*

| ID Landslide | ID Damage | Damage Type | Width [cm] | Automatic Area [$m^2$] | Measured Area [$m^2$] | Error [$m^2$] |
|---|---|---|---|---|---|---|
| | **1** | FC | 1.68 | 0.49 | 1.42 | - |
| | **2** | LC | 1.15 | 0.11 | 1.16 | 1.05 |
| **V1** | **3** | FC | 1.54 | 24.04 | 25.54 | - |
| | **4** | LC | 1.32 | 0.12 | 0.98 | 0.86 |
| | **5** | LC | 1.00 | 0.15 | 1.43 | 1.28 |
| | **6** | LC | 1.54 | 0.22 | 0.53 | 0.31 |
| **V1** | **7** | LC | 1.66 | 1.03 | 3.70 | 2.67 |
| **V1** | **8** | TC | 1.43 | 0.17 | 2.11 | 1.94 |
| **V1** | **9** | FC | 1.54 | 2.33 | 15.67 | - |
| **V1** | **10** | LC | 3.59 | 1.45 | 5.52 | 4.07 |
| **V1** | **11** | D_D | 1.32 | 0.12 | 2.10 | - |
| **V1** | **12** | LC | 1.34 | 0.15 | 3.33 | 3.18 |

| | | | | | | |
|---|---|---|---|---|---|---|
| **V1** | **13** | LC | 2.12 | 0.36 | 1.85 | 1.49 |
| **V1** | **14** | LC | 1.32 | 0.04 | 0.19 | 0.15 |
| **V1** | **15** | LC | 3.50 | 0.38 | 1.75 | 1.37 |
| **V1** | **16** | LC | 3.21 | 1.47 | 3.94 | 2.47 |
| **V1** | **17** | FC | 1.59 | 1.02 | 7.37 | - |
| **V1** | **18** | TC | 1.32 | 0.04 | 0.16 | 0.12 |
| **V1** | **19** | TC | 1.00 | 0.04 | 0.18 | 0.14 |
| **V1** | **20** | LC | 0.97 | 0.01 | 0.63 | 0.62 |
| **V1** | **21** | TC | 1.00 | 0.07 | 0.12 | 0.05 |
| **V1** | **22** | TC | 0.95 | 0.02 | 0.34 | 0.32 |
| **V1** | **23** | TC | 1.73 | 0.34 | 4.07 | 3.73 |
| **V1** | **24** | FC | 1.40 | 2.57 | 9.38 | - |
| **V1** | **25** | LC | 0.97 | 0.18 | 1.79 | 1.61 |
| **V1** | **26** | TC | 2.71 | 0.06 | 0.06 | 0.00 |
| **V1** | **27** | LC | 1.36 | 0.72 | 7.13 | 6.41 |
| **V1** | **28** | FC | 1.63 | 1.37 | 8.67 | - |
| **V1** | **29** | FC | 2.71 | 1.31 | 3.27 | - |
| **V1** | **30** | LC | 1.78 | 0.08 | 1.49 | 1.41 |
| **V1** | **31** | TC | 1.00 | 0.04 | 0.29 | 0.25 |
| **V1** | **32** | TC | 0.97 | 0.18 | 1.99 | 1.81 |
| **V1** | **33** | FC | 1.54 | 0.36 | 1.88 | - |
| **V2** | **34** | LC | 2.11 | 1.16 | 9.81 | 8.65 |
| **V3** | **35** | FC | 1.43 | 3.49 | 26.73 | - |
| **V3** | **36** | FC | 0.97 | 0.12 | 0.97 | - |
| **V3** | **37** | TC | 1.26 | 0.16 | 1.46 | 1.30 |
| **V3** | **38** | FC | 2.85 | 5.08 | 12.21 | - |
| **V3** | **39** | FC | 2.76 | 2.20 | 7.20 | - |
| **V3** | **40** | FC | 1.28 | 2.99 | 9.68 | - |
| **V3** | **41** | LC | 2.75 | 0.82 | 3.60 | 2.78 |
| **V3** | **42** | FC | 1.27 | 2.74 | 11.90 | - |
| **V3** | **43** | LC | 2.75 | 0.82 | 2.36 | 1.54 |
| **V4** | **44** | FC | 2.85 | 5.08 | 11.11 | - |
| **V4** | **45** | FC | 1.60 | 15.83 | 18.59 | - |
| | **46** | FC | 2.85 | 5.08 | 8.88 | - |

***Table 4.7.*** *Modified from Nappo et al. (2021b). Classification of damage on SC – Vercana using the multi-criteria binary classifier.*

| Multi-criteria binary classifier | | | | | |
|---|---|---|---|---|---|
| **ID Landslide** | **ID Damage** | **Density of damage points [No/m$^2$]** | **Density of non-damage points [No/m$^2$]** | **Damage ratio** | **Rating** |
| | **1** | 111 | 256 | 0.43 | **XXXIII** |
| | **2** | 230 | 172 | 1.34 | **III** |
| **V1** | **3** | 135 | 186 | 0.72 | **XV** |
| | **4** | 134 | 261 | 0.51 | **XXVI** |
| | **5** | 100 | 285 | 0.35 | **XXXV** |
| | **6** | 151 | 206 | 0.73 | **XIV** |
| **V1** | **7** | 88 | 258 | 0.34 | **XXXVI** |
| **V1** | **8** | 64 | 329 | 0.19 | **XLI** |
| **V1** | **9** | 113 | 249 | 0.45 | **XXXI** |
| **V1** | **10** | 137 | 219 | 0.63 | **XXII** |
| **V1** | **11** | 97 | 295 | 0.33 | **XXXVII** |
| **V1** | **12** | 26 | 29 | 0.88 | **X** |
| **V1** | **13** | 56 | 229 | 0.24 | **XXXIX** |
| **V1** | **14** | 5 | 26 | 0.20 | **XL** |
| **V1** | **15** | 141 | 115 | 1.22 | **V** |
| **V1** | **16** | 239 | 161 | 1.48 | **I** |
| **V1** | **17** | 122 | 243 | 0.50 | **XXVII** |
| **V1** | **18** | 13 | 381 | 0.03 | **XLIV** |
| **V1** | **19** | 11 | 367 | 0.03 | **XLV** |
| **V1** | **20** | 159 | 229 | 0.69 | **XVII** |
| **V1** | **21** | 0 | 367 | 0.00 | **XLVI** |
| **V1** | **22** | 29 | 385 | 0.08 | **XLIII** |
| **V1** | **23** | 136 | 190 | 0.72 | **XVI** |
| **V1** | **24** | 123 | 247 | 0.50 | **XXIX** |
| **V1** | **25** | 88 | 223 | 0.39 | **XXXIV** |
| **V1** | **26** | 50 | 417 | 0.12 | **XLII** |
| **V1** | **27** | 104 | 234 | 0.45 | **XXXII** |
| **V1** | **28** | 134 | 119 | 1.13 | **VII** |
| **V1** | **29** | 160 | 211 | 0.76 | **XIII** |

| | | | | | |
|---|---|---|---|---|---|
| **V1** | **30** | 158 | 254 | 0.62 | **XXIII** |
| **V1** | **31** | 72 | 134 | 0.54 | **XXV** |
| **V1** | **32** | 92 | 294 | 0.31 | **XXXVIII** |
| **V1** | **33** | 146 | 241 | 0.60 | **XXIV** |
| **V2** | **34** | 167 | 177 | 0.95 | **VIII** |
| **V3** | **35** | 149 | 166 | 0.90 | **IX** |
| **V3** | **36** | 155 | 119 | 1.30 | **IV** |
| **V3** | **37** | 227 | 159 | 1.43 | **II** |
| **V3** | **38** | 127 | 196 | 0.65 | **XXI** |
| **V3** | **39** | 195 | 168 | 1.16 | **VI** |
| **V3** | **40** | 120 | 239 | 0.50 | **XXVIII** |
| **V3** | **41** | 23 | 27 | 0.88 | **XI** |
| **V3** | **42** | 180 | 386 | 0.47 | **XXX** |
| **V3** | **43** | 36 | 42 | 0.88 | **XII** |
| **V4** | **44** | 139 | 216 | 0.65 | **XIX** |
| **V4** | **45** | 117 | 178 | 0.66 | **XVIII** |
| | **46** | 174 | 270 | 0.65 | **XX** |

***Table 4.8.*** *Modified from Nappo et al. (2021b). Classification of damage on SC – Vercana using the IRI-based damage severity levels.*

| | | **IRI classifier** | | | **Roughness** | | | |
|---|---|---|---|---|---|---|---|---|
| **ID Landslide** | **ID Damage** | **Number of points** | | | **Mean (μ)** | **St. Dev. (σ)** | **CV (= σ/μ)** | **Overall severity** |
| | | **D1** | **D2** | **D3** | | | | |
| | **1** | 19 | 4 | 3 | 1.64 | 1.76 | 1.07 | **D0** |
| | **2** | 86 | 30 | 15 | 3.35 | 3.26 | 0.97 | **D0** |
| **V1** | **3** | 5218 | 1185 | 594 | 7.04 | 3.53 | 0.50 | **D1** |
| | **4** | 32 | 0 | 0 | 1.71 | 1.39 | 0.81 | **D0** |
| | **5** | 26 | 1 | 0 | 1.47 | 1.27 | 0.86 | **D0** |
| | **6** | 17 | 3 | 1 | 2.18 | 1.92 | 0.88 | **D0** |
| **V1** | **7** | 73 | 16 | 33 | 8.96 | 5.29 | 0.59 | **D2** |
| **V1** | **8** | 17 | 0 | 1 | 5.51 | 2.5 | 0.45 | **D1** |
| **V1** | **9** | 379 | 18 | 5 | 5.41 | 2.05 | 0.38 | **D1** |
| **V1** | **10** | 208 | 28 | 27 | 6.98 | 4.41 | 0.63 | **D1** |
| **V1** | **11** | 49 | 2 | 0 | 5.12 | 1.07 | 0.21 | **D1** |

| | | | | | | | | |
|---|---|---|---|---|---|---|---|---|
| **V1** | **12** | 32 | 6 | 9 | 8.49 | 5.91 | 0.70 | **D2** |
| **V1** | **13** | 22 | 3 | 1 | 5.72 | 2.78 | 0.49 | **D1** |
| **V1** | **14** | 0 | 0 | 0 | 1.27 | 0.57 | 0.45 | **D0** |
| **V1** | **15** | 46 | 30 | 65 | 15.49 | 13.85 | 0.89 | **D3** |
| **V1** | **16** | 346 | 125 | 79 | 4.12 | 5.14 | 1.25 | **D1** |
| **V1** | **17** | 276 | 65 | 20 | 6.82 | 3.5 | 0.51 | **D1** |
| **V1** | **18** | 0 | 0 | 0 | 0.81 | 0.5 | 0.62 | **D0** |
| **V1** | **19** | 0 | 0 | 0 | 0.74 | 0.59 | 0.80 | **D0** |
| **V1** | **20** | 31 | 6 | 11 | 9.11 | 6.96 | 0.76 | **D2** |
| **V1** | **21** | 0 | 0 | 0 | 0.73 | 0.5 | 0.68 | **D0** |
| **V1** | **22** | 1 | 0 | 0 | 0.93 | 0.8 | 0.86 | **D0** |
| **V1** | **23** | 177 | 53 | 33 | 8.03 | 5.37 | 0.67 | **D2** |
| **V1** | **24** | 286 | 70 | 65 | 8.49 | 6.49 | 0.76 | **D2** |
| **V1** | **25** | 54 | 13 | 16 | 9.4 | 7.68 | 0.82 | **D2** |
| **V1** | **26** | 0 | 2 | 0 | 8.63 | 0.23 | 0.03 | **D2** |
| **V1** | **27** | 154 | 10 | 0 | 5.39 | 1.25 | 0.23 | **D1** |
| **V1** | **28** | 428 | 115 | 33 | 6.91 | 2.83 | 0.41 | **D1** |
| **V1** | **29** | 157 | 28 | 13 | 6.92 | 4.47 | 0.65 | **D1** |
| **V1** | **30** | 56 | 17 | 9 | 7.96 | 6.02 | 0.76 | **D1** |
| **V1** | **31** | 2 | 0 | 0 | 4.9 | 0.86 | 0.18 | **D1** |
| **V1** | **32** | 27 | 0 | 0 | 4.87 | 0.67 | 0.14 | **D1** |
| **V1** | **33** | 59 | 9 | 4 | 6.37 | 2.58 | 0.41 | **D1** |
| **V2** | **34** | 531 | 79 | 29 | 6.27 | 2.51 | 0.40 | **D1** |
| **V3** | **35** | 1412 | 251 | 102 | 6.63 | 3.16 | 0.48 | **D1** |
| **V3** | **36** | 50 | 6 | 0 | 5.58 | 1.63 | 0.29 | **D1** |
| **V3** | **37** | 160 | 31 | 1 | 6.21 | 1.84 | 0.30 | **D1** |
| **V3** | **38** | 464 | 59 | 49 | 6.75 | 3.47 | 0.51 | **D1** |
| **V3** | **39** | 527 | 43 | 17 | 5.93 | 2.28 | 0.38 | **D1** |
| **V3** | **40** | 286 | 70 | 65 | 8.21 | 3.38 | 0.41 | **D2** |
| **V3** | **41** | 32 | 6 | 9 | 2.49 | 4.45 | 1.79 | **D0** |
| **V3** | **42** | 507 | 12 | 3 | 2.67 | 2.21 | 0.83 | **D0** |
| **V3** | **43** | 32 | 6 | 9 | 8.97 | 4.45 | 0.50 | **D2** |
| **V4** | **44** | 464 | 59 | 49 | 2.21 | 2.47 | 1.12 | **D0** |
| **V4** | **45** | 1593 | 201 | 113 | 4.66 | 2.68 | 0.58 | **D1** |

| | | | | | | | |
|---|---|---|---|---|---|---|---|
| | **46** | 464 | 59 | 49 | 2.3 | 2.47 | 1.07 | **D0** |

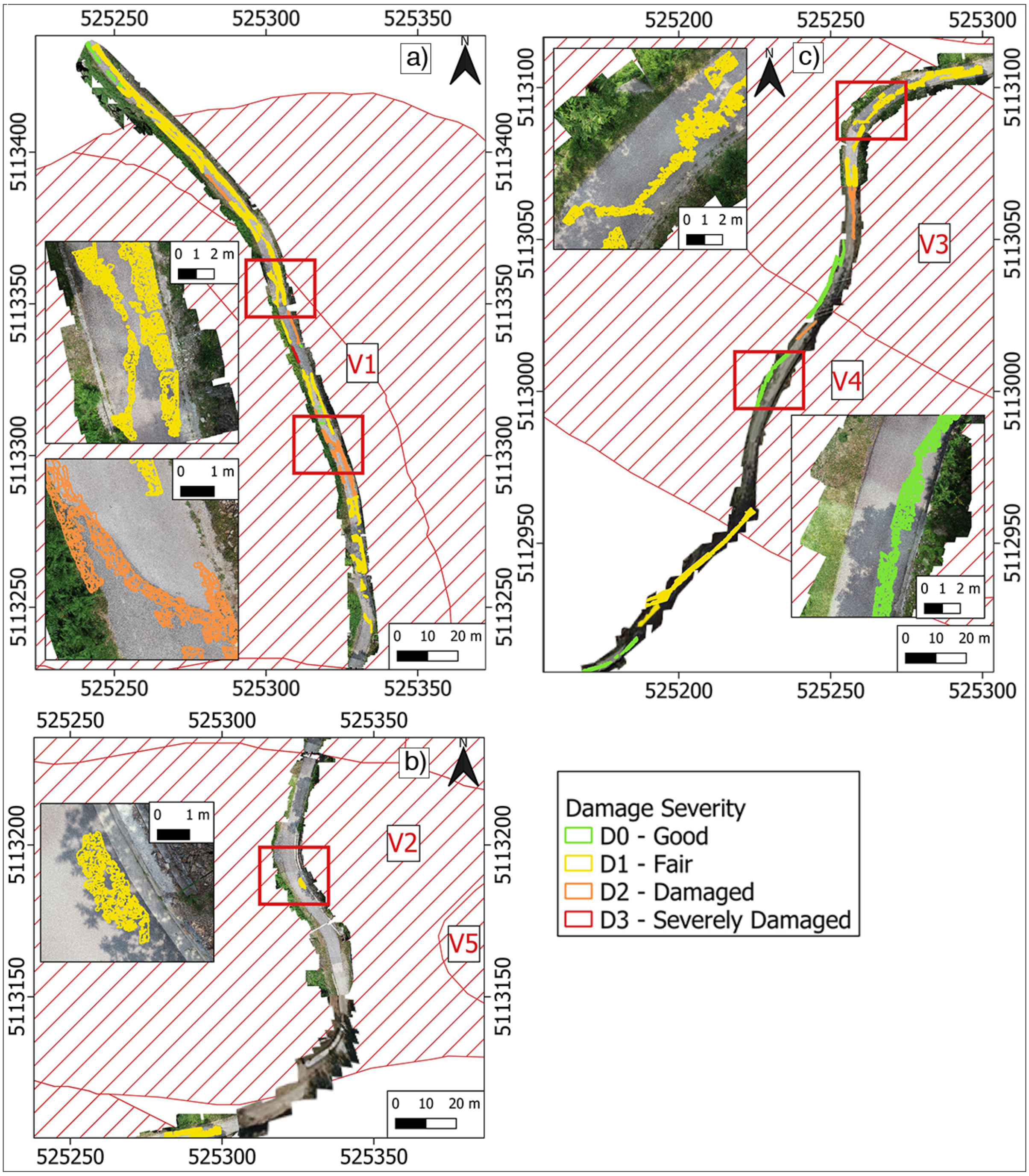

***Figure 4.15.*** *Modified from Nappo et al. (2021b). IRI-based severity classification of 2D automatic damage polygons of SC – Vercana crossing a) V1, b) V2, and c) V3 and V4 landslides. Reference system: WGS84/UTM zone 32N.*

### 4.4.4 Specifics of the generated 3D models

For completeness, this Section reports the specifics of the 3D model reconstruction via SfM of SP14 – Laino and SC – Vercana.

For SP14 – Laino, two 3D models were generated from images taken at 10 and 30 m altitude. The first point cloud (at 10 m) is composed by 47,264,421 points; the second (at 30 m) by 60,439,041 points. Table 4.9 reports the errors generated during the SfM process. The GSD of the image overlap is 0.11 cm/pixel (Nappo et al., 2021b).

***Table 4.9.*** *Modified from Nappo et al. (2021b). Quality report of the SP14 – Laino 3D model.*

| **Case study: SP14 - Laino** | | | | | | | |
|---|---|---|---|---|---|---|---|
| | **Absolute camera position and orientation uncertainties** | | | | | | |
| | X [m] | Y [m] | Z [m] | Omega [degree] | Phi [degree] | Kappa [degree] | |
| Mean | 0.142 | 0.106 | 0.178 | 0.053 | 0.067 | 0.094 | |
| Sigma | 0.038 | 0.015 | 0.016 | 0.003 | 0.010 | 0.013 | |
| | **Relative camera position and orientation uncertainties** | | | | | | |
| | X [m] | Y [m] | Z [m] | Omega [degree] | Phi [degree] | Kappa [degree] | Reprojection error [pixel] |
| Mean | 0.001 | 0.002 | 0.002 | 0.022 | 0.015 | 0.011 | 0.127 |
| Sigma | 0.001 | 0.001 | 0.001 | 0.003 | 0.007 | 0.004 | |
| | **Geolocation variance** | | | | | | |
| | X [m] | Y [m] | Z [m] | Omega [degree] | Phi [degree] | Kappa [degree] | |
| Mean | 0.001 | 0.002 | -0.009 | | | | |
| Sigma | 0.321 | 0.614 | 0.374 | | | | |
| RMSE | 0.321 | 0.614 | 0.374 | 1.406 | 3.393 | 7.969 | |

The SC – Vercana 3D model is composed by 797,708,725 points. The errors generated during the SfM process are reported in Table 4.10. The GSD of the image overlap is 0.17 cm/pixel (Nappo et al., 2021b).

*Table 4.10. Modified from Nappo et al. (2021b). Quality report of the SC – Vercana 3D model.*

| **Case study: SC – Vercana** | | | | | | | |
|---|---|---|---|---|---|---|---|
| | **Absolute camera position and orientation uncertainties** | | | | | | |
| | X [m] | Y [m] | Z [m] | Omega [degree] | Phi [degree] | Kappa [degree] | |
| Mean | 0.115 | 0.128 | 0.191 | 0.065 | 0.060 | 0.072 | |
| Sigma | 0.024 | 0.035 | 0.010 | 0.006 | 0.003 | 0.001 | |
| | **Relative camera position and orientation uncertainties** | | | | | | |
| | X [m] | Y [m] | Z [m] | Omega [degree] | Phi [degree] | Kappa [degree] | Reprojection error [pixel] |
| Mean | 0.010 | 0.031 | 0.011 | 0.045 | 0.092 | 0.015 | 0.130 |
| Sigma | 0.003 | 0.020 | 0.007 | 0.025 | 0.018 | 0.004 | |
| | **Geolocation variance** | | | | | | |
| | X [m] | Y [m] | Z [m] | Omega [degree] | Phi [degree] | Kappa [degree] | |
| Mean | 0.001 | 0.002 | -0.007 | | | | |
| Sigma | 0.604 | 1.844 | 0.665 | | | | |
| RMSE | 0.604 | 1.844 | 0. 665 | 1.404 | 3.174 | 5.487 | |

# 5. CHALLENGES IN MONITORING CONSTRUCTIONS IN VULNERABLE AREAS

Monitoring structures and infrastructures affected by ground movements originated from subsidence and landslides is fundamental to "*strengthen disaster risk governance*" and "*reduce disaster damage to critical (infra)structures and disruption of basic services*" (UNDRR, 2021). To this aim, the use of remote sensing techniques (e.g., satellite-based InSAR and UAV-based photogrammetry) at different scales (from large to small) represents a valid support to local governments or civil protection departments, but their interpretation might be challenging. Each remote sensing technique has its own limitations (e.g., distortions in the SAR images, UAV maximum speed and flight time) that need to be considered when monitoring (infra)structures subjected to subsidence and/or landslides. Also, data acquisition, processing or geolocation errors can lead to erroneous interpretations of the acquired dataset. Therefore, although guidelines and standard procedures can be established at different scales of analysis to facilitate the adoption of InSAR (e.g., DPC-ReLUIS, 2021; Ezquerro et al., 2020; Peduto et al., 2015) and UAV (e.g., Nappo et al., 2021b) in the management of (infra)structures subjected to ground and slope instabilities, it is necessary to acquire a good knowledge of the construction, impacting hazard and geological setting of the investigated area via documentary and/or in situ investigations. Then, depending on the problem arising during the investigation of buildings subjected to subsidence and road pavements affected by landslides, the most appropriate solution should be determined case by case.

This Chapter provides two examples of issues encountered during respectively the use of InSAR measurements for monitoring a residential area in the city of Rome (Italy) subjected to subsidence, and the use of UAV-based 3D models to detect landslide-induced damage on the pavement of a highway interchange in Panagia (Greece). For each case study, a possible solution to the encountered issue is proposed and other alternatives are discussed.

## 5.1 Where are the PS? [4]

The residential area of Valco San Paolo in the city of Rome (Italy) is built on a Late Pleistocene to Holocene alluvial valley bordered at W by the Tiber River and at E by a currently culverted tributary of the River, named Grotta Perfetta stream (Bozzano et al., 2000, 2008; Funiciello and Giordano, 2008; Luberti et al., 2017; Marra and Rosa, 1995; Milli et al., 2016; Parotto, 2008; Ventriglia et al., 2002 – Fig. 5.1a).

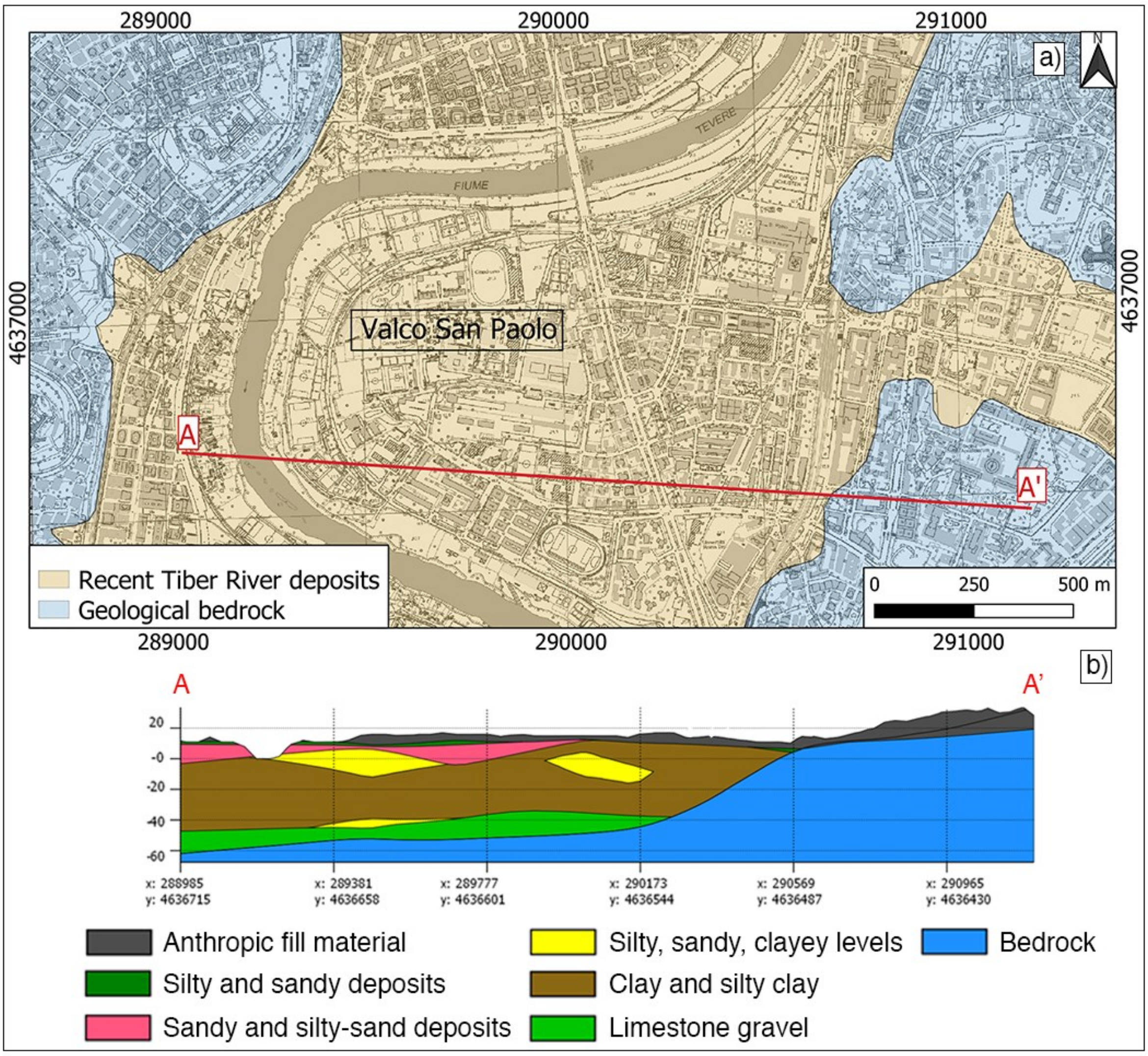

*Figure 5.1. a) Geological map and (modified from Bozzano et al., 2008) and b) Geological cross section AA' (courtesy of M. Rompato, University of Cassino, and F. Bozzano, Sapienza University of Rome) of the Valco San Paolo area in Rome (Italy). Reference system: WGS84/UTM zone 33N.*

---

[4] The contents of this Section are part of the author's ongoing work at Sapienza University of Rome (Italy) in the framework of DPC-ReLUIS 2019-2021 Project (WP6).

The valley is formed by a lithological sequence (Fig. 5.1b) of 1) anthropic fill material, 2) silty and sandy deposits, 3) brown to yellow sandy and silty-sand deposits, 4) alternating silty-sandy, sandy-silty, clayey-silty and clayey levels, 5) grey clay and silty clay with variable peat content, 6) limestone gravel in a grey, sandy-silty matrix, and 7) pre-Holocene valley bedrock (Bozzano et al., 2008). Given the presence of alternated layers of compressible soil, the area is prone to long-lasting subsidence (Bozzano et al., 2008).

Aiming at applying the InSAR-based multi-scale framework to monitor urban areas subjected to subsidence as proposed in Chapter 3, C-band (ERS 1&2 and Envisat) and X-band (Cosmo-SkyMed) InSAR data acquired between ca. 1992 and 2014 (Fig. 5.2) were visualized on the Italian Geoportale Nazionale (2021).
The large-scale analysis of ERS 1&2 and Envisat InSAR measurements showed downward movements in the southern sector of the Valco San Paolo area (Fig. 5.2a-d). Although the C-band data coverage was limited, the same deformation pattern was observed also with CSK (Fig. 5.2e-f). Here, the multivariate regression analysis could not be performed because the InSAR data were not downloadable, and the geological information were too sparse to reliably reconstruct the stratigraphy of the entire residential area. As an alternative to the proposed large-scale subsidence mapping, only the buildings showing average LOS velocity lower than -5 mm/year during the entire monitoring period (i.e., 1992-2019) were considered for further vulnerability assessment (e.g., Peduto et al., 2015; Ezquerro et al., 2020).

As for the vulnerability analysis of these buildings, although subsidence settlements are possible because of the complex geology of the area, the interpretation of InSAR measurements was not straightforward. Indeed, multiple factors, either structural (e.g., elastic behaviour, thermic expansion, viscous shrinkage) or geological (e.g., large-scale subsidence of the valley, local consolidation processes), could contribute to the formation of the downward InSAR signal and should be discerned to correctly interpret the data (DPC-ReLUIS, 2021). In this regard, the collection of cartographic data and original construction projects could be of primary help to define the features of the investigated buildings. Then, once the building typology has been determined, comparisons with the fragility curves available in literature (e.g., Nappo et al., 2021a; Peduto et al., 2017c; Zhang and Ng, 2005) could be established to pursue a first attempt of vulnerability analysis for the investigated building.

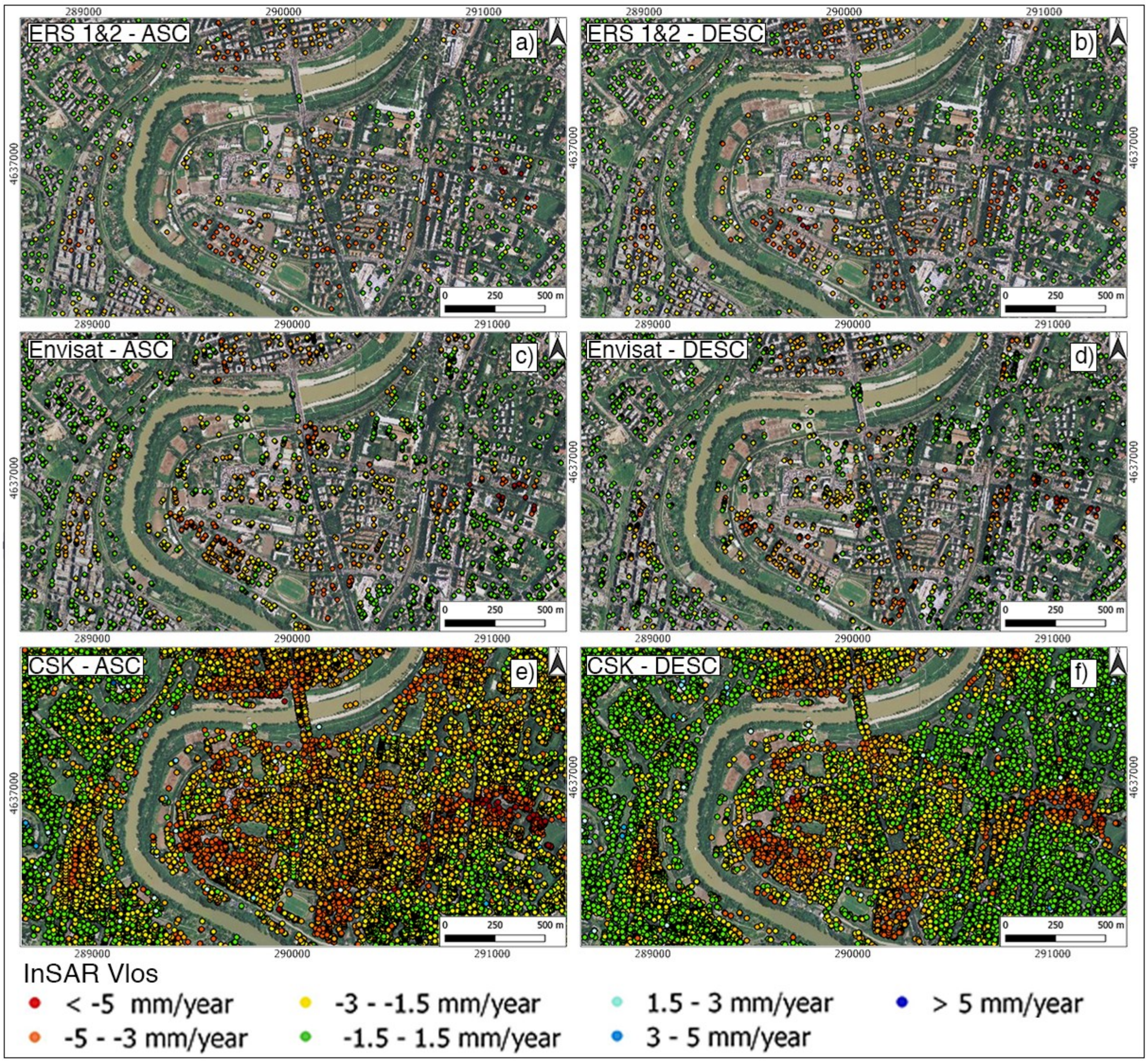

***Figure 5.2.*** *PS LOS velocity maps recorded from a) – b) ERS 1&2 (1992-2000), c) – d) Envisat (2003-2010), and e) – f) Cosmo-SkyMed (2011-2014), in ascending and descending acquisition geometries. (Source: Geoportale Nazionale, 2021). Reference system: WGS84/UTM zone 33N.*

Here, the tower residential buildings named “Torri stellari” (Fig. 5.3) already investigated by Di Carlo et al. (2021) are used as an example for small-scale analysis in absence of downloadable InSAR products. These buildings are composed by 8 floors and have a load-bearing tower structure made of reinforced concrete and finished with brick walls and hollow block slabs; the foundation system is constituted by isolated spread footing posed at 4 m depth with micro piles reaching the deeper bedrock (Di Carlo et al., 2021 – Fig. 5.3a). The average LOS velocity recorded on these buildings between 2011 and 2019 ranges between -3 and -5 mm/year, with a vertical displacement of about 2 mm in the considered time frame (Di Carlo et al., 2021). From the comparison with the fragility curves proposed by Nappo et al. (2021a), the damage severity of these buildings should correspond to D1 (i.e., w < 0.1 mm). In situ inspections of the damage pattern of the considered buildings confirmed a low-range damage severity, compatible with a D1 level as derived from Nappo et al. (2021a).

Further investigations are surely needed to properly assess the damage pattern and severity of the considered buildings and determine whether the observed InSAR signal is likely attributable to the local subsidence predisposing factors (e.g., Nappo et al., 2020). However, these preliminary results allow thinking that subsidence might be the primary cause of movement for these tower buildings, and therefore will be investigated in more detail.

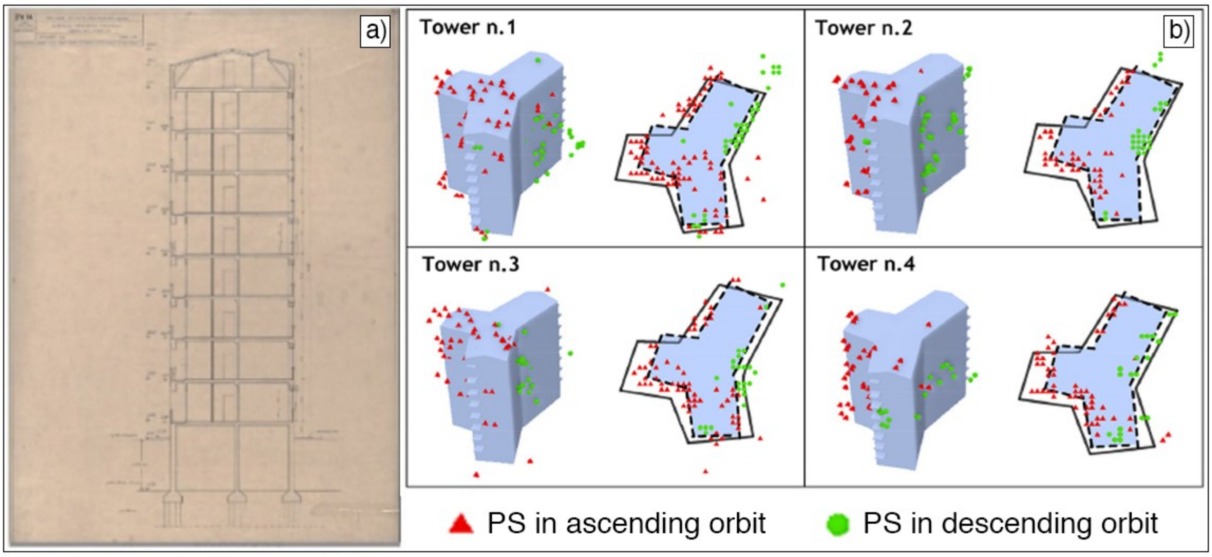

***Figure 5.3.*** *Example of tower buildings in Valco San Paolo residential area (Rome). a) Typical cross section of the buildings from archive records of the original construction project (modified from Di Carlo et al., 2021). b) Positioning of CSK PS in ascending and descending acquisition geometries on the 3D modelled buildings (modified from Di Carlo et al., 2021).*

Another important aspect to consider when monitoring buildings subjected to ground instability using InSAR measurements is the correct geolocation and positioning of InSAR PS that is fundamental to determine the (natural or anthropic) element to which a measurement is referred. The PS location is determined with the geocoding of InSAR products during their processing by transforming radar coordinates into a common geodetic reference system (Hanssen, 2001; Montazeri et al., 2018). The accuracy of the results, generally in the order of 1-2 m, depends on the quality of the DTM adopted during the InSAR processing to estimate the topographic phase component and the reference point (DPC-ReLUIS, 2021). Depending on the input SAR images and satellite, the PS can be precisely located on the volume of a construction (e.g., roof, façade) by estimating their height during the InSAR processing. In this regard, Figure 5.3 shows an example of correct positioning of CSK PS on 3D modelled buildings in Valco San Paolo area (Di Carlo et al., 2021).

## 5.2 Pavement distress or error? [5]

The Panagia Interchange (Km 121+940) of Egnatia Odos A2 motorway in Greece is composed by a two-lane bridge and two roadways constructed on clayey and silty sands, stiff clay/ophiolite and flysch (Loli et al., 2020 – Fig. 5.4). The geotechnical properties of these lithotypes are reported in Table 5.1.

***Table 5.1.*** *Geotechnical parameters at Panagia Interchange (Greece) (modified from Loli et al., 2020).*

| | **Clayey and silty sand** | **Stiff clay/ophiolite** | **Flysch** |
|---|---|---|---|
| SPT count number ($N_{SPT}$) | 16 (14-19) | 43 | 16 |
| 1D Compression Index ($E_m$) [MPa] | - | 50 | > 900 |
| Water content (w) [%] | 1.1 | 11.8 | - |
| Specific weight (γ) [kN/m$^3$] | 21.6 | 24.2 | 25 |
| Void ratio (e) | 0.44 | - | 0.44 |
| Effective friction angle (ϕ’) [°] | 33 | 24 | 35 |
| Effective cohesion (c’) [kPa] | 5 | 35 | 70 |
| Residual friction angle ($\phi'_r$) [°] | 18 | 20 | - |
| Undrained shear strength ($C_u$) [kPa] | 70 | 220 | - |
| Permeability (K) [cm/s] | 4.6E-05 | 2.4E-05 | 1E-05 |

The area is subjected to the movements of an active landslide (Loli et al., 2020), and therefore was surveyed in October 2020 with a DJI drone flying at ca. 58 m altitude in oblique acquisition mode to detect damage on the asphalt-paved motorway and adjacent secondary roads. To this

---

[5] The contents of this Section are based on the author’s work performed at University of Twente (The Netherlands) in the framework of Horizon 2020 PANOPTIS Project (WP5), and the manuscript “*Routine monitoring and quick response strategies for infrastructure assets via UAV acquisitions*” co-authored with Sofia Tilon, Francesco Nex, Norman Kerle (University of Twente), Irene Sevilla De la llave and Miguel Angel Martin Cuenca (Acciona Ingenieria S.A.) - currently in preparation.

aim, 224 (4000x3000) RGB images with GSD of 1.71 cm/pixel were collected to reconstruct the 3D point cloud and the 2D ortho image of the surveyed area (in blue in Fig. 5.4) via SfM algorithm.

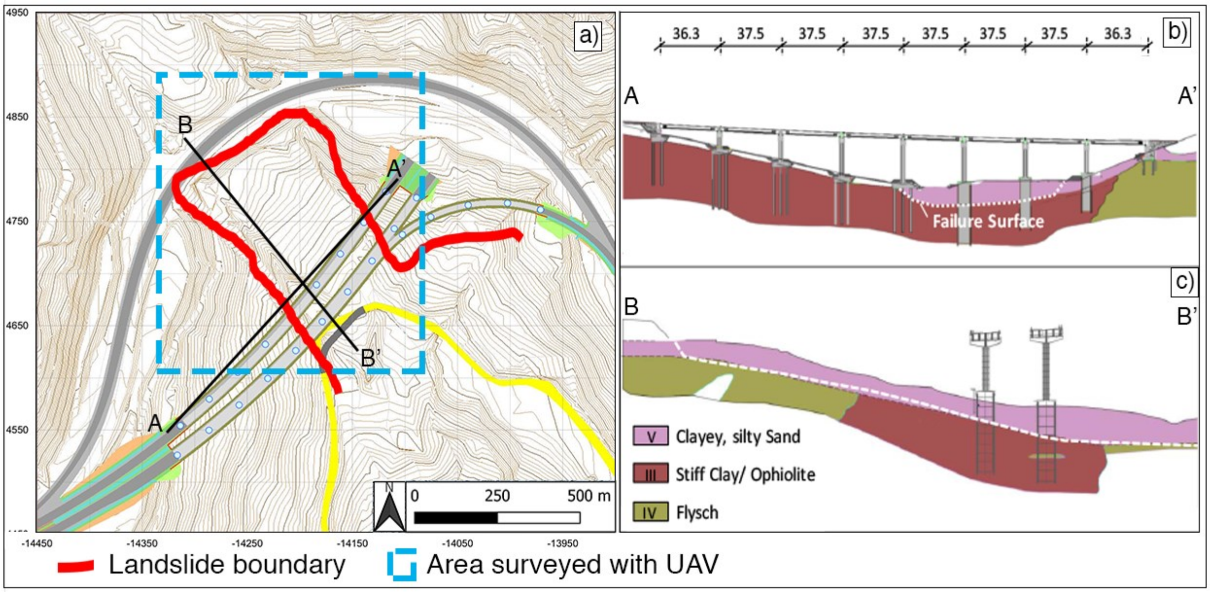

***Figure 5.4.*** *a) Topographic map of Panagia Interchange (Greece) with indication of landslide boundary and area surveyed with UAV (modified from Loli et al., 2020). Geological cross sections b) AA' and c) BB' (modified from Loli et al., 2020). Reference system: WGS84/UTM zone 34N.*

Aiming at detecting and classifying the pavement damage potentially induced by landslides on the motorway, the semi-automatic procedure using UAV photogrammetry products as proposed in Chapter 4 was adopted also here.

During field surveys, fractures were not detected on the four investigated road sections (i.e., uphill and downhill lanes of the A2 motorway, and uphill and downhill secondary roads); therefore, only pavement deformations were researched by computing the distance of 3D points from the reference surface constructed for each road section (see Fig.4.4a) to obtain the damage hotspot map. At first sight, deformations between 2 and 6 cm were identified at the interface between the uphill secondary road and the landslide (Fig. 5.5a), and peaks up to ± 10-20 cm were detected on the other road sections (Fig. 5.5b-c). Instead, a closer investigation of the road pavements revealed the presence of artefacts in the point cloud resulting in extended holes in the model (Fig. 5.5b and c) and compromising the correct interpretation of the results.

What initially looked like pavement deformations were revealed to be instead errors in the point cloud. Several attempts of reprocessing the UAV images and the newly generated point clouds were performed to determine the origin of the error, which was then attributed to the mismatching of UAV images in the SfM processing or the insufficient overlap (< 80%) between adjacent images. Another possible cause of mismatching could be the incorrect positioning of the 3D scene into the space, here performed automatically using the satellite GPS integrated with the aircraft, that could be refined by using Ground Control Points (GCP) in future works.

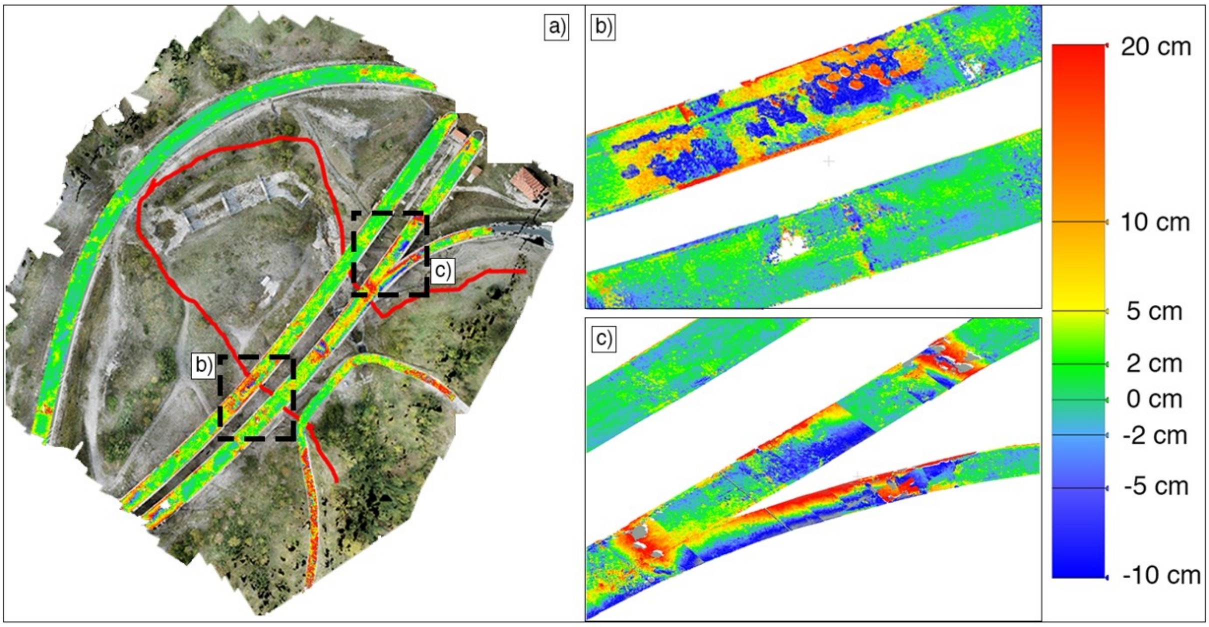

***Figure 5.5.*** *a) Top view of the 3D point cloud of Panagia Interchange (Greece) superimposed with the deviations of the road asphalt 3D points from a reference surface. b) and c) Artefacts generated during the SfM point cloud generation.*

# 6. CONCLUSIONS

The presented Ph.D. Thesis pursued the establishment of standard and semi-automatic procedures to facilitate the adoption of remote sensing techniques (e.g., satellite-based InSAR and UAV-based photogrammetry) for routine monitoring of (historic) buildings subjected to subsidence and road networks exposed to landslides. Such procedures can effectively contribute to the management of risks related to subsidence and landslides interacting with (infra)structures, thus preventing that these ground and slope instabilities of moderate intensity may turn into unforeseen disasters with severe consequences for society, economy, urban and natural environments. The millimetric accuracy and wide spatial and temporal coverage of InSAR measurements allow interpreting the spatial distribution of subsidence at large scale and monitoring the small scale movements experienced by buildings resting on compressible stratigraphic units prone to subside. Accurate geolocation and positioning of InSAR products are essential to avoid misinterpretations of data and provide reliable vulnerability maps for risk management purposes.

As for UAV-based photogrammetry products, they proved to be successful in detecting longitudinal and transverse cracks induced by landslides on asphalt road pavements and rating their severity in four levels based on the International Roughness Index (IRI). Precautions need to be taken in the image acquisition and processing phases to assure a minimum overlap of 80% between adjacent images and avoid mismatching that may compromise the road damage detection and classification.

The strategies proposed in this Thesis specifically address a two-fold need: a better understanding of the complex relationships between causes (i.e., subsidence and landslides) and effects (i.e., ground sinking and damage) on the (infra)structures, and the quantitative detection and classification of road pavement damage as already available for building damage.

Multi-platform and multi-temporal InSAR data were embedded here in a multi-scale framework for monitoring the causes and effects of subsidence in urban areas.

At large scale, the use of a multivariate regression model was proposed to investigate the correlations between C-band InSAR-derived ground measurements and subsidence predisposing factors (e.g., compressible soil layers, groundwater level variations) attributable to the local hydro-geological, stratigraphic and geotechnical setting. The multivariate regression analysis applied to the city of Como (northern Italy) demonstrated that subsidence needs to be modelled with nonlinear functions (e.g., hyperbolic, quadratic, seasonal) that may account for the spatial heterogeneity of ground lowering due to different stages of soil consolidation, rapid events or changes in predisposing or triggering factors (Cigna et al., 2011; Kim et al., 2010; Nappo et al., 2020). Although nonlinear behaviours may remain undetected when InSAR data are unwrapped with linear deformation models, a good hydrogeological and geotechnical knowledge of the investigated site can assist in the interpretation of PS time series for monitoring subsidence (Cigna et al., 2011; Nappo et al., 2020). The spatial distribution of residuals generated from the multivariate regression modelling was adopted here to detect areas subjected to hydro-geological and stratigraphic conditions predisposing to subsidence and (nonlinearly) correlated with the InSAR-derived measurements. This approach allows determining whether the (known) causes of subsidence are sufficient to explain the vertical movements of the ground, or other (natural or anthropogenic) factors influence the InSAR signal and (potentially) increase or decrease the ground instability.

At small scale, the vulnerability of (historic) buildings exposed to subsidence was assessed via empirical fragility curves correlating the severity of damage observed on the structures with the intensity of subsidence, described here as the differential settlement or relative rotation induced by the ground movements at building foundation depth. The subsidence-related intensity (SRI) parameters (i.e., differential settlement and relative rotation) can be obtained more precisely from X-band, rather than C-band, InSAR measurements because of the higher ground resolution of these SAR sensors (e.g., Del Ventisette et al., 2013; Peduto et al., 2015). The procedure adopted for subsidence vulnerability analyses in urban areas is strictly related to the building damage assessment that, in turn, depends on the conservation status (e.g., frequency of maintenance or restoration works) of each structure (Nappo et al., 2021a). The damage classification adapted from Burland et al. (1977) was based on the width of fractures measured on the field on the exterior façades of the buildings. This could induce underestimations or overestimations of the damage severity because the interior crack pattern is not considered. Additionally, the building response is conditioned by the foundation typology, therefore more precise information about the building foundation system is recommended to improve the vulnerability analysis.

The multi-scale procedure was performed with a deterministic approach, but future refinements of the proposed framework may adopt probabilistic models and advanced functions to account for more variations of the subsidence predisposing factors and give a broader spectrum of possible future building damage scenarios.

The multi-scale framework for monitoring the effects of subsidence in urban areas was applied to the city of Como (N Italy) that, resting on highly compressible Late Pleistocene to Holocene sediments with variable groundwater content due to the vicinity to the Lake Como, is naturally prone to long-lasting ground sinking (Nappo et al., 2020, 2021a). Additional anthropogenic activities started in 1945-1950 exacerbated the natural subsidence of the area, reaching peaks of movement of 10 mm/year along the lakeshore (Comerci et al., 2007; Ferrario et al., 2015a; Nappo et al., 2020, 2021a). The multivariate regression analysis at basin scale was performed using C-band ERS 1&2 (1992-2000) and Envisat (2003-2010) data. At this step, the InSAR-derived ground movements were correlated to known subsidence predisposing factors (SPF – i.e., thicknesses of compressible lithologies, overburden stress and piezometric level). For the purpose of this research, the SPF were assumed invariant in the years 1992-2010 because i) the dense urbanization of the city does not permit modifications of the thickness of sedimentary units, ii) localized anthropogenic activity (e.g., the novel construction of buildings) would not affect the overburden stress at basin scale, and iii) seasonal variations of the piezometric level are negligible at basin scale (Nappo et al., 2020). The analysis of nonlinear GAM regression residuals (Fig. 3.10) revealed that 70% of the InSAR-derived vertical velocity can be related to the SPF at basin scale. Some uncertainties were detected in the Cosia stream delta area (i.e., the NW sector of the basin) and persisted even when considering the anthropogenic culverting of the Cosia stream and the recent (Late Pliocene to Late glacial) activity of the Gonfolite backthrust (Livio et al., 2011; Michetti et al., 2014a, 2014b; Sileo et al., 2007) as possible additional factors influencing the InSAR signal in that area (Nappo et al., 2020). However, this highlighted the necessity of further detailed investigations in the NW sector of the basin of Como to determine what causes the InSAR-derived vertical velocity to be higher in this area, and eventually verify their interaction with local subsidence. On the other hand, the spatial pattern of regression residuals in the historic centre of the city of Como resulted to be small and unstructured, thus suggesting a higher correlation between SPF and InSAR-derived ground measurements. Therefore, this area was selected for the small scale vulnerability analysis.

This analysis was performed using X-band Cosmo-SkyMed (2010-2019) data that allowed retrieving the SRI parameters (i.e., differential settlement and relative rotation) associated to each building that were then correlated with building damage severity via empirical fragility curves. For the vulnerability analysis of Como historic centre, the buildings' foundation typology was assumed to be shallow due to the lack of more detailed information. Additionally, the observed fractures were assumed to be due to exclusively vertical movements, without considering possible tilting, because of the availability of a single CSK acquisition geometry (i.e., descending). The vulnerability analysis could be greatly improved when CSK data from both ascending and descending orbits will be combined to retrieve the vertical and horizontal components of LOS movements (Nappo et al., 2021a). Regardless of these limitations typical of this kind of analyses, the vulnerability analysis of masonry and reinforced concrete buildings of Como historic centre (Fig. 3.12 and 3.13) demonstrated that, as expected, the most severe damage occurs on buildings experiencing higher differential settlements and/or relative rotations (Nappo et al., 2021a). These results can be compared with only a few studies involving masonry and reinforced concrete buildings resting on shallow foundations in subsiding areas (e.g., Nappo et al., 2021a; Peduto et al., 2019; Zhang and Ng, 2005). Diverse procedures can be adopted for the computation of the SRI parameters; for instance, the length (L) could be calculated as the Euclidean distance between two points, or by plotting the profile of InSAR data interpolated within a single building (Nappo et al., 2021a). Moreover, the sample of considered buildings may differ for geometry, finishing of the façade and/or foundation system, thus resulting in different damage patterns. The results obtained for Como historic centre showed that the differential settlement is the SRI parameter to be preferred to differentiate between damage severity levels in future vulnerability analyses in the city (Nappo et al., 2021a).

A semi-automatic procedure combining UAV-based 3D and 2D photogrammetry products was also proposed in this Thesis to characterize and rate the severity of longitudinal and transverse cracks on asphalt road pavements in landslide-affected areas (Nappo et al., 2021b).

Point cloud models of the asphalt road pavements can be reconstructed from UAV-based RGB images, when appropriately overlapping, to automatically detect longitudinal and transverse cracks wider than 1 cm induced by landslides on the asphalt road surface (Nappo et al., 2021b). The DJI Phantom4 PRO adopted for this research was flown along a regular acquisition path at 10 m height from the road surface, thus avoiding obstacles such as trees or vehicles. UAV types, flying altitudes and paths can be adapted according to the specific application and study area, but local regulations (e.g., ENAC, 2021) must be respected. Images can be collected in the nadir and/or oblique acquisition views to mitigate occlusion problems (Nappo et al., 2021b). For this research, UAV images were acquired in the nadir view with Ground Sample Distance (GSD) of 0.11 (in Laino) and 0.17 cm/pixel (in Vercana), thus distinguishing longitudinal and transverse cracks on the asphalt road pavement and ensuring that the road-related proxies obtained from the 3D models are significative and reliable (Nappo et al., 2021b). Prior to the generation of the 3D point cloud of the investigated road surface, shadow removal algorithms can be applied to the UAV images to limit noises or errors in the 3D model reconstruction (Nappo et al., 2021b).

Moreover, the satellite GPS receiver integrated with the Phantom4 PRO was used here to automatically position the acquired UAV images into the space and generate the 3D model (Nappo et al., 2021b). Although georeferencing errors lower than 0.7 m were produced when locating the 3D models on the topographic maps (reference system: WGS 84/ UTM zone 32 N), this did not affect the detection and classification of longitudinal and transverse cracks on the asphalt-paved roads (Nappo et al., 2021b). However, Ground Control Points (GCP) could be used in future works to enhance the geolocation precision of the road 3D models in the photogrammetric processing.

The damage hotspots maps, generated as Euclidean distance of 3D points from a reference surface, underlined the heterogeneity of landslides' effects on asphalt road pavements and provided a first tool for road practitioners to localize areas of expected damage formation (Nappo et al., 2021b). Further tests on road sections with diverse damage and instability conditions could broaden the applicability of this hotspot map to detect multiple types of road pavement damage, rather than deformations and longitudinal and transverse cracks (Nappo et al., 2021b). The geometric features (i.e., omnivariance, verticality and roughness) generated from the processing of the 3D point cloud allowed to train the multi-criteria and IRI-based classifiers. The first allowed determining the presence/absence of road pavement damage from the point cloud by labelling a 3D point as *damage* or *not-damage* based on certain thresholds imposed on the geometric features. The second classifier determined the severity level (from D0 to D3) of each 3D point based on the International Roughness Index (IRI). Both multi-criteria and IRI-based classifiers correctly detected longitudinal and transverse cracks wider than 1 cm, thus representing an effective tool to prioritize maintenance road interventions based on the extent or severity of landslide-related damage (Nappo et al., 2021b). Although refinements of both classifiers are necessary, they have the great potential of detecting damage directly from the 3D point cloud without prior knowledge of the road pavement condition (Nappo et al., 2021b).

The edge detection algorithm (Canny, 1986; Cubero-Fernandez et al., 2017) applied to the 2D ortho images generated from the photogrammetric 3D model reconstruction successfully detected longitudinal and transverse cracks wider than 1 cm (Nappo et al., 2021b). Although the real width of the fractures is lost with the automatic edge detection and shadowed images can affect the damage recognition, 93% overlap between manual and automatic results could be achieved for detached fractures.

The combination of UAV-based 3D and 2D photogrammetric products allowed then attributing quantitative information (e.g., width, area, roughness) to longitudinal and transverse cracks, then rated according to their extent and IRI-based severity.

The results obtained from this procedure allowed characterizing the asphalt road pavement damage using its geometry and extent rather than circular buffers of fixed length (e.g., Nappo et al., 2019), and rating the severity of each fracture according to a road-related descriptor (i.e., IRI) rather than a parameter representing the landslide intensity (e.g., Ferlisi et al., 2020a; Mavrouli et al., 2019). Embedding such quantitative descriptions of longitudinal and transverse cracks into vulnerability analyses of road networks affected by landslides, rather than segmenting the roads into portions of variable lengths (e.g., Ferlisi et al., 2020a), could greatly improve the management of landslide risk to linear infrastructure (Nappo et al., 2021b).

However, additional efforts are needed to extend the applicability of the proposed procedure to longer road networks and critical infrastructure, where the UAV flight height might be limited and 10 m altitude might be forbidden (ICAO, 2021; ENAC, 2021). In this regard, standard protocols could be established to automate the UAV acquisition over strategic infrastructure, also adopting fixed-wing or VTOL aircrafts, thus rendering this procedure more feasible at larger scales (Nappo et al., 2021b). As future research, InSAR- (e.g., Nappo et al., 2019) and UAV-based procedures (e.g., Nappo et al., 2021b) may be combined to establish novel frameworks for multi-scale monitoring of road networks affected by landslides.

The semi-automatic procedure proposed to detect and classify longitudinal and transverse cracks on asphalt road pavements affected by landslides using UAV-based photogrammetry products was applied to the provincial road SP14 in Laino and the municipal road SC in Vercana municipalities in the Province of Como (northern Italy) (Nappo et al., 2021b). Here, the frequency distribution of asphalt road damage typologies (as defined in Table 2.1) in landslide areas was preliminarily assessed (Table 4.1), thus determining that longitudinal and transverse cracks can be attributed to the movements of landslides (Mavrouli et al., 2019; Nappo et al., 2019, 2021b). However, it is fundamental considering that each type of pavement distress could be induced by the synergistic action of multiple factors, and therefore broader analyses are necessary to identify a single damage cause (Nappo et al., 2021b).

The damage hotspots maps highlighted deviations of ± 5 cm where longitudinal and transverse cracks are wider than 1 cm (in Laino) and 2 cm (in Vercana). The multi-criteria and IRI-based classifiers detected longitudinal and transverse cracks wider than 1 cm on both SP14 – Laino and SC – Vercana, although noises and boundary effects are visible in both case studies due to possible geolocation errors of the data and/or the presence of concrete structures (e.g., curbs, ditches) at the edges of the road pavements (Nappo et al., 2021b).

The automatic edge detection showed high accuracy in both case studies, with differences between automatic and manual measurements of the fractures' area ranging between 0.01 and 1.56 $m^2$ for SP14 – Laino, and 0 – 8.65 $m^2$ for SC – Vercana (Nappo et al., 2021b). The automatically detected polygons were then rated according to the damage extent (from the multi-criteria 3D point classification) and severity (from the IRI-based classification), thus providing a helpful contribution to local road practitioners and Governments to prioritize the small-scale interventions and preserve the road infrastructure from more severe landslide consequences.

Although beyond the scope of the research, fatigue cracks were detected on the SP14 – Laino and SC – Vercana in different steps (i.e., damage hotspot map, geometric features, multi-criteria and IRI-based classifiers, automatic edge detection), thus underlying the necessity of additional research to generalize the application of the tested procedure to other damage typologies or constrain it better to solely landslide-induced damage.

In the end, precautions need to be taken when monitoring (infra)structures affected by ground and slope instabilities using InSAR and/or UAV technologies.

Common issues that might be encountered in using InSAR measurements for monitoring urban areas subjected to subsidence are the lack of a complete (multi-platform and multi-temporal) dataset that might limit the application of multivariate regression analysis, and the PS geolocation and position on the affected building. In this regard, the case of Valco San Paolo residential area in the city of Rome (Italy) remarked the importance of geological investigations to interpret the InSAR measurements at large-scale when the proposed method for zoning the subsidence risk using a nonlinear multivariate regression analysis is not straightforward. In such way it is still possible to determine the constructions that are affected by higher vertical movements and for which a vulnerability analysis might be performed via comparisons with existing literature. For a rapid assessment of building vulnerability to subsidence, in absence of detailed information on the damage status or before performing a field investigation, the fragility curves available in the literature (e.g., Nappo et al., 2021a; Peduto et al., 2017c; Zhang and Ng, 2005) could be useful to determine the expected building damage severity. For instance, this approach was tested for four residential tower buildings identified in the Valco San Paolo area that showed high InSAR LOS velocity in the years 1992-2019 and vertical differential settlement of 2 mm; this resulted in the definition of a D1 building damage severity level (i.e., fracture width lower than 0.1 mm) then confirmed by in situ inspections. Additionally, the correct geolocation and positioning of InSAR PS on the volume of a construction (e.g., roof, façade) is important when monitoring buildings subjected to ground instability using InSAR measurements, thus determining whether the measurement can be referred to the terrain or to the construction.

As for the application of UAV-based methodologies for road damage detection in landslide-affected areas, a common issue might be the mismatching of acquired images during the reconstruction of the road 3D models via the Structure from Motion (SfM) algorithm. This error might be due to an insufficient image overlap (i.e., lower than 80%) between adjacent UAV acquisitions that determines errors in the point cloud that might be misinterpreted as pavement distress. To avoid similar errors, the UAV flight should be accurately planned either considering possible adverse weather conditions (e.g., strong wind) or acquiring additional (backup) images. In this regard, the case of Panagia Interchange (Greece) demonstrated the importance of a good input set of UAV images to automatically detect distresses on asphalt-paved roads. Future works might consider the use of fixed-wing or VTOL aircrafts to acquire images over strategic infrastructure and limit the interventions of the pilot in the image acquisition phase. Moreover, Ground Control Points (GCP) and GPS permanent stations could be used to improve the geolocation and orientation of the UAV images into the space, thus reducing the possible errors and image mismatching in the 3D model reconstruction phase.

Finally, it is worth noticing that the methodologies presented in this Ph.D. Thesis can be further implemented to foster the demand of safe and resilient constructions to mitigate future disasters. The wish is that these automatic procedures will be integrated into the risk management framework via guidelines or protocols for routine monitoring of structures subjected to ground movements, such as those generated by subsidence and landslides.

# REFERENCES

## *Abstract*

UNDRR, 2021. URL https://www.undrr.org/implementing-sendai-framework/what-sendai-framework - Last access: September 2021.

## *Chapter 1 - Introduction*

AASHO, 1962. Road Test-Report61E. HRB, National Research Coun- cil, Washington, D.C., USA.

ANAS, 2004. I Quaderni tecnici per la salvaguardia delle infrastrutture V.

Ancochea, E., Huertas, M.J., Hernán, F., Brändle, J.L., 2010. Volcanic evolution of São Vicente, Cape Verde Islands: The Praia Grande landslide. J. Volcanol. Geotherm. Res. 198, 143–157. https://doi.org/10.1016/J.JVOLGEORES.2010.08.016

Antonielli B., Sciortino A., Scancella S., Bozzano F., Mazzanti P. (2021). Tracking deformation processes at the Legnica Glogow Copper District (Poland) by Satellite InSAR—I: Room and Pillar Mine District. Land,10, 653. https://doi.org/10.3390/ land10060653

ASTM, 2020. ASTM D6433-20 Standard Practice for Roads and Parking Lots Pavement Condition Index Surveys, ASTM International, West Conshohocken, PA, USA.

Bianchini, S., Pratesi, F., Nolesini, T., Casagli, N., 2015. Building deformation assessment by means of persistent scatterer interferometry analysis on a landslide-affected area: The Volterra (Italy) case study. Remote Sens. 7, 4678–4701. https://doi.org/10.3390/rs70404678

Bjerrum, L., 1967. Engineering geology of Norwegian normally-consolidated marine clays as related to settlements of buildings. Geotechnique 17, 83–118. https://doi.org/10.1680/geot.1967.17.2.83

Bjerrum, L., 1963. Allowable settlement of structures, in: 3rd European Conference on Soil Mechanics and Foundation Engineering, Wiesbaden, 2, Brighton, England. pp. 135–137.

Blong, R.J., 1973. A numerical classification of selected landslides of the debris-slide-avalanche-flow type, Engineering Geology, Chapter 7, pp.99-144.

Borrelli, L., Nicodemo, G., Ferlisi, S., Peduto, D., Di Nocera, S., Gullà, G., 2018. Geology, slow-moving landslides, and damages to buildings in the Verbicaro area (North-western Calabria region, southern Italy). J. Maps 14, 32–44. https://doi.org/10.1080/17445647.2018.1425164

Boscardin, M.D., Cording, E.J., 1989. Building Response to Excavation-Induced Settlement. J. Geotech. Eng. 115, 1–21. https://doi.org/10.1061/(ASCE)0733-9410(1989)115:1(1)

Botey i Bassols, J., Vàzquez-Suñé, E., Crosetto, M., Barra, A., Gerard, P., 2021. D-InSAR monitoring of ground deformation related to the dewatering of construction sites. A case study of Glòries Square, Barcelona. Engineering Geology, 286, 106041, https://doi.org/10.1016/j.enggeo.2021.106041

Bozzano, F., Esposito, C., Franchi, S., Mazzanti, P., Perissin, D., Rocca, A., Romano, E., 2015. Understanding the subsidence process of a quaternary plain by combining geological and hydrogeological modelling with satellite InSAR data: The Acque Albule Plain case study. Remote Sensing of Environment, 168, 219–238.

Bozzano, F., Esposito, C., Mazzanti, P., Patti, M., Scancella, S., 2018. Imaging multi-age construction settlement behaviour by advanced SAR interferometry. Remote Sens. 10. https://doi.org/10.3390/rs10071137

Burland, J.B., Broms, B.B., De Mello, V.F.B., 1977. Behaviour of Foundations and Structures Comportement des Fondations et des Structures. State Art Rep. 363–400.

Burland, J.B., Wroth, C.P., 1974. Settlement of buildings and associated damage, in: Settlement of Structures, Proceedings of the Conference of the British Geotechnical Society. pp. 611–764.

Cardenal, J., Fernández, T., Pérez-García, J.L., Gómez-López, J.M., 2019. Measurement of road surface deformation using images captured from UAVs. Remote Sens. 11, 1–24. https://doi.org/10.3390/rs11121507

Cascini, L., Calvello, M., Grimaldi, G.M., 2010a. Groundwater Modeling for the Analysis of Active Slow-Moving

Landslides. ASCE Library. https://ascelibrary.org/doi/abs/10.1061/(ASCE)GT.1943-5606.0000323

Corominas, J., Moya, J., Ledesma, A. et al., 2005 Prediction of ground displacements and velocities from groundwater level changes at the Vallcebre landslide (Eastern Pyrenees, Spain). Landslides 2, 83–96 (2005). https://doi.org/10.1007/s10346-005-0049-1

Crosta, G.B., Imposimato, S., Roddeman, D., Chiesa, S., Moia, F., 2005. Small fast-moving flow-like landslides in volcanic deposits: The 2001 Las Colinas Landslide (El Salvador). Eng. Geol. 79, 185–214. https://doi.org/10.1016/J.ENGGEO.2005.01.014

Cruden, D.M., 1991. A simple definition of landslide, Bulletin of International Association of Engineering Geology, n.43, Paris, pp.27-28.

Cruden, D., Varnes, D., 1996. Landslides: Investigation and Mitigation. Chapter 3 - Landslide Types and Processes. Transp. Res. Board Spec. Rep.

Cusicanqui, J., Kerle, N., Nex, F., 2018. Usability of aerial video footage for 3-D scene reconstruction and structural damage assessment. Nat. Hazards Earth Syst. Sci. 18, 1583–1598. https://doi.org/10.5194/nhess-18-1583-2018

D'Amico, F., Gagliardi, V., Bianchini Ciampoli, L., Tosti, F., 2020. Integration of InSAR and GPR techniques for monitoring transition areas in railway bridges. NDT & E International, 115, 102291.

Dai, F.C, Lee, C.F., 2001. Frequency–volume relation and prediction of rainfall-induced landslides, Engineering Geology, Volume 59, Issues 3–4, Pages 253-266, https://doi.org/10.1016/S0013-7952(00)00077-6

de Wit, K., Lexmond, B.R., Stouthamer, E., Neussner, O., Dörr, N., Schenk, A., Minderhoud, P.S.J., 2021. Identifying Causes of Urban Differential Subsidence in the Vietnamese Mekong Delta by Combining InSAR and Field Observations. Remote Sensing, 13, 189. https://doi.org/10.3390/rs13020189

del Ventisette, C., Solari, L., Raspini, F., Ciampalini, A., di Traglia, F., Moscatelli, M., Pagliaroli, A., Moretti, S., 2015. Use of PSInSAR data to map highly compressible soil layers. Geol. Acta 13, 309–323. https://doi.org/10.1344/GeologicaActa2015.13.4.4

Den Haan, E.J., Kruse, G.A.M., 2006. Characterisation and engineering properties of Dutch peats. In: Tan, T.S., Phoon, K.K., Hight, D.W., Leroueil, S. (Eds.), Characterization and Engineering Properties of Natural Soils 3. Taylor & Francis Group, London, pp. 2101–2133.

DPC-ReLUIS, 2021. URL https://www.reluis.it/it/ - Last access: September 2021.

Duarte, D., Nex, F., Kerle, N., Vosselman, G., 2017. Towards a more efficient detection of earthquake induced façade damages using oblique UAV imagery. Int. Arch. Photogramm. Remote Sens. Spat. Inf. Sci. - ISPRS Arch. 42, 93–100. https://doi.org/10.5194/isprs-archives-XLII-2-W6-93-2017

EEA, 2021. URL https://www.eea.europa.eu/data-and-maps/daviz/natural-hazards-in-eea-member-countries-6/#tab-dashboard-01 – Last access: September 2021.

European Commission, 2021. Overview of natural and man-made disaster risks the European Union may face. Commission Staff Working Document. Brusselles, 22 march 2021.

Ezquerro, P., Del Soldato, M., Solari, L., Tomás, R., Raspini, F., Ceccatelli, M., Fernández-Merodo, J.A., Casagli, N., Herrera, G., 2020. Vulnerability Assessment of Buildings due to Land Subsidence using InSAR Data in the Ancient Historical City of Pistoia (Italy). Sensors 20, 2749. https://doi.org/10.3390/s20102749

Fazio, N.L., Perrotti, M., Andriani, G.F., Mancini, F., Rossi, P., Castagnetti, C., Lollino, P., 2019. A new methodological approach to assess the stability of discontinuous rocky cliffs using in-situ surveys supported by UAV-based techniques and 3-D finite element model: a case study. Eng. Geol. 260. https://doi.org/10.1016/j.enggeo.2019.105205

Fell, R., Corominas, J., Bonnard, C., Cascini, L., Leroi, E., Savage, W.Z., 2008. Guidelines for landslide susceptibility, hazard and risk zoning for land use planning. Eng. Geol. 102, 85–98. https://doi.org/10.1016/j.enggeo.2008.03.022

Ferlisi, S., Marchese, A., Peduto, D., 2020a. Quantitative analysis of the risk to road networks exposed to slow-moving landslides: a case study in the Campania region (southern Italy). Landslides 2020. https://doi.org/10.1007/s10346-020-01482-8

Fernandez Galarreta, J., Kerle, N., Gerke, M., 2015. UAV-based urban structural damage assessment using object-based image analysis and semantic reasoning. Nat. Hazards Earth Syst. Sci. 15, 1087–1101.

https://doi.org/10.5194/nhess-15-1087-2015

Ferrario, M.F., Bonadeo, L., Brunamonte, F., Livio, F., Martinelli, E., Michetti, A.M., Censi Neri, P., Chiessi, V., Comerci, V., Höbig, N., 2015a. Late Quaternary environmental evolution of the Como urban area (Northern Italy): A multidisciplinary tool for risk management and urban planning. Eng. Geol. 193, 384–401. https://doi.org/10.1016/j.enggeo.2015.05.013

Galloway, D.L.; Burbey, T.J., 2011. Review: Regional land subsidence accompanying groundwater extraction. Hydrogeol. J., 19, 1459–1486.

George, K.P., Rajagopal, A.S., Lim, L.K., 1989. Models for predicting pavement deterioration. Transp. Res. Rec. 1215, 1–7.

Giordan, D., Adams, M.S., Aicardi, I., Alicandro, M., Allasia, P., Baldo, M., De Berardinis, P., Dominici, D., Godone, D., Hobbs, P., Lechner, V., Niedzielski, T., Piras, M., Rotilio, M., Salvini, R., Segor, V., Sotier, B., Troilo, F., 2020. The use of unmanned aerial vehicles (UAVs) for engineering geology applications. Bull. Eng. Geol. Environ. 79, 3437–3481. https://doi.org/10.1007/s10064-020-01766-2

Giordan, D., Hayakawa, Y., Nex, F., Remondino, F., Tarolli, P., 2018. Review article: the use of remotely piloted aircraft systems (RPASs) for natural hazards monitoring and management. Nat. Hazards Earth Syst. Sci. 18, 1079–1096. https://doi.org/10.5194/nhess-18-1079-2018

Gomez, C., Purdie, H., 2016. UAV- based Photogrammetry and Geocomputing for Hazards and Disaster Risk Monitoring – A Review. Geoenvironmental Disasters. https://doi.org/10.1186/s40677-016-0060-y

Guzzetti, F., Peruccacci, S., Rossi, M. et al. 2007. Rainfall thresholds for the initiation of landslides in central and southern Europe. Meteorol. Atmos. Phys. 98, 239–267. https://doi.org/10.1007/s00703-007-0262-7

Herrera, G., Fernández, J.A., Tomás, R., Cooksley, G., Mulas, J., 2009. Advanced interpretation of subsidence in Murcia (SE Spain) using A-DInSAR data - Modelling and validation. Nat. Hazards Earth Syst. Sci. 9, 647–661. https://doi.org/10.5194/nhess-9-647-2009

Herrera, G., Tomás, R., Monells, D., Centolanza, G., Mallorquí, J.J., Vicente, F., Navarro, V.D., Lopez-Sanchez, J.M., Sanabria, M., Cano, M., Mulas, J., 2010. Analysis of subsidence using TerraSAR-X data: Murcia case study. Eng. Geol. 116, 284–295. https://doi.org/10.1016/j.enggeo.2010.09.010

Hungr, O., Leroueil, S., Picarelli, L., 2014. The Varnes classification of landslide types, an update. Landslides 11, 167–194. https://doi.org/10.1007/s10346-013-0436-y

Hürlimann, M., Garcia-Piera, J.O., Ledesma, A., 2000. Causes and mobility of large volcanic landslides: application to Tenerife, Canary Islands. J. Volcanol. Geotherm. Res. 103, 121–134. https://doi.org/10.1016/S0377-0273(00)00219-5

Hutchinson, J.N., 1988. General report: Morphological and geotechnical parameters of landslides in relation to geology and hydrogeology, Proc.5th Int. Symp. Landslides, Lousanne, Switzerland, 3-35.

Inzerillo, L., Di Mino, G., Roberts, R., 2018. Image-based 3D reconstruction using traditional and UAV datasets for analysis of road pavement distress. Autom. Constr. 96, 457–469. https://doi.org/10.1016/j.autcon.2018.10.010

ISPRA, 2021. URL https://www.isprambiente.gov.it – Last access: September 2021.

Jaboyedoff, M., Michoud, C., Derron, M.H., Voumard, J., Leibundgut, G., Sudmeier-Rieux, K., Michoud, C., Nadim, F., Leroi, E., 2016. Human-Induced Landslides: Toward the analysis of anthropogenic changes of the slope environment. In: Landslides and Engineered Slopes. Experience, Theory and Practice. 1st Edition, CRC Press, ISBN 9781315375007.

Jones, S., Kasthurba, A.K., Bhagyanathan, A. et al. 2021. Impact of anthropogenic activities on landslide occurrences in southwest India: An investigation using spatial models. J Earth Syst Sci 130, 70 (2021). https://doi.org/10.1007/s12040-021-01566-6

Kawagoe, S., Kazama, S., Priyantha Ranjan Sarukkalige, 2009. Assessment of snowmelt triggered landslide hazard and risk in Japan, Cold Regions Science and Technology, Volume 58, Issue 3, Pages 120-129, https://doi.org/10.1016/j.coldregions.2009.05.004

Keefer, D.K., 2002. Investigating Landslides Caused by Earthquakes – A Historical Review. Surveys in Geophysics 23, 473–510. https://doi.org/10.1023/A:1021274710840

Kontogianni, V., Stiros, S.C., 2020. Ground loss and static soil–Structure Interaction during Urban Tunnel Excavation: Evidence from the Excavation of the Athens Metro. Infrastructures, 5, 64.

https://doi.org/10.3390/infrastructures5080064

Krøgli, I. K., Devoli, G., Colleuille, H., Boje, S., Sund, M., and Engen, I. K., 2018. The Norwegian forecasting and warning service for rainfall- and snowmelt-induced landslides, Nat. Hazards Earth Syst. Sci., 18, 1427–1450, https://doi.org/10.5194/nhess-18-1427-2018

Lissak, C., Bartsch, A., De Michele, M., Gomez, C., Maquaire, O., Raucoules, D., Roulland, T., 2020. Remote Sensing for Assessing Landslides and Associated Hazards. Surv. Geophys. https://doi.org/10.1007/s10712-020-09609-1

Martino, S., Scarascia Mugnozza, G., 2005. The role of the seismic trigger in the Calitri landslide (Italy): historical reconstruction and dynamic analysis, Soil Dynamics and Earthquake Engineering, Volume 25, Issue 12, Pages 933-950, https://doi.org/10.1016/j.soildyn.2005.04.005

Mavrouli, O., Corominas, J., Ibarbia, I., Alonso, N., Jugo, I., Ruiz, J., Luzuriaga, S., Navarro, J.A., 2019. Integrated risk assessment due to slope instabilities in the roadway network of Gipuzkoa, Basque Country. Nat. Hazards Earth Syst. Sci. 19, 399–419. https://doi.org/10.5194/nhess-19-399-2019

Mayr, A., Rutzinger, M., Geitner, C., 2018. Multitemporal analysis of objects in 3D point clouds for landslide monitoring. Int. Arch. Photogramm. Remote Sens. Spat. Inf. Sci. - ISPRS Arch. 42, 691–697. https://doi.org/10.5194/isprs-archives-XLII-2-691-2018

Milillo, P., Giardina, G., DeJong, M.J., Perissin, D., Milillo, G., 2018. Multi-temporal InSAR structural damage assessment: The London crossrail case study. Remote Sensing, 10, 287.

Mohamadi, B., Balz, T., Younes, A., 2019. A model for complex subsidence causality interpretation based on PS-InSAR cross-heading orbits analysis. Remote Sens. 11. https://doi.org/10.3390/rs11172014

Nappo, N., Ferrario, M.F., Livio, F., Michetti, A.M., 2020. Regression Analysis of Subsidence in the Como Basin (Northern Italy): New Insights on Natural and Anthropic Drivers from InSAR Data. Remote Sens. 12, 2931. https://doi.org/10.3390/rs12182931

Nappo, N., Mavrouli, O., Nex, F., van Westen, C., Gambillara, R., Michetti, A.M., 2021b. Use of UAV-based photogrammetry products for semi-automatic detection and classification of asphalt road damage in landslide-affected areas. Eng. Geol. 294, 106363. https://doi.org/10.1016/j.enggeo.2021.106363

Nappo, N., Peduto, D., Mavrouli, O., van Westen, C.J., Gullà, G., 2019. Slow-moving landslides interacting with the road network: Analysis of damage using ancillary data, in situ surveys and multi-source monitoring data. Eng. Geol. 260, 105244. https://doi.org/10.1016/j.enggeo.2019.105244

Nappo, N., Peduto, D., Polcari, M., Livio, F., Ferrario, M.F., Comerci, V., Stramondo, S., Michetti, A.M., 2021a. Subsidence in Como historic centre (northern Italy): assessment of building vulnerability combining hydrogeological and stratigraphic features, Cosmo-SkyMed InSAR and damage data. Int. J. Disaster Risk Reduct. 56, 102115. https://doi.org/10.1016/j.ijdrr.2021.102115

Naudet, V., Lazzari, M., Perrone, A., Loperte, A., Piscitelli, S., Lapenna, V., 2008. Integrated geophysical and geomorphological approach to investigate the snowmelt-triggered landslide of Bosco Piccolo village (Basilicata, southern Italy), Engineering Geology, Volume 98, Issues 3–4, Pages 156-167, https://doi.org/10.1016/j.enggeo.2008.02.008

Nex, F., Duarte, D., Steenbeek, A., Kerle, N., 2019. Towards real-time building damage mapping with low-cost UAV solutions. Remote Sens. https://doi.org/10.3390/rs11030287

Nex, F., Remondino, F., 2014. UAV for 3D mapping applications: A review. Appl. Geomatics. https://doi.org/10.1007/s12518-013-0120-x

Nicodemo, G., Peduto, D., Ferlisi, S., 2020. Building damage assessment and settlement monitoring in subsidence-affected urban areas: case study in the Netherlands. Proc. Int. Assoc. Hydrol. Sci. 382, 651–656. https://doi.org/10.5194/piahs-382-651-2020

Niethammer, U., Rothmund, S., Schwaderer, U., Zeman, J., Joswig, M., 2012. Open source image-processing tools for low-cost uav-based landslide investigations. ISPRS - Int. Arch. Photogramm. Remote Sens. Spat. Inf. Sci. XXXVIII-1/C22, 161–166. https://doi.org/10.5194/isprsarchives-xxxviii-1-c22-161-2011

Peduto, D., Cascini, L., Arena, L., Ferlisi, S., Fornaro, G., Reale, D., 2015. A general framework and related procedures for multiscale analyses of DInSAR data in subsiding urban areas. ISPRS J. Photogramm. Remote Sens. 105, 186–210. https://doi.org/10.1016/j.isprsjprs.2015.04.001

Peduto, D., Elia, F., Montuori, R., 2018. Probabilistic analysis of settlement-induced damage to bridges in the city of Amsterdam (The Netherlands). Transp. Geotech. 14, 169–182. https://doi.org/10.1016/j.trgeo.2018.01.002

Peduto, D., Ferlisi, S., Nicodemo, G., Reale, D., Pisciotta, G., Gullà, G., 2017a. Empirical fragility and vulnerability curves for buildings exposed to slow-moving landslides at medium and large-scales. Landslides 14, 1993–2007. https://doi.org/10.1007/s10346-017-0826-7

Peduto, D., Huber, M., Speranza, G., van Ruijven, J., Cascini, L., 2017b. DInSAR data assimilation for settlement prediction: Case study of a railway embankment in the Netherlands. Can. Geotech. J. 54, 502–517. https://doi.org/10.1139/cgj-2016-0425

Peduto, D., Korff, M., Nicodemo, G., Marchese, A., Ferlisi, S., 2019. Empirical fragility curves for settlement-affected buildings: Analysis of different intensity parameters for seven hundred masonry buildings in The Netherlands. Soils Found. 59, 380–397. https://doi.org/10.1016/j.sandf.2018.12.009

Peduto, D., Nicodemo, G., Maccabiani, J., Ferlisi, S., 2017c. Multi-scale analysis of settlement-induced building damage using damage surveys and DInSAR data: A case study in The Netherlands. Eng. Geol. 218, 117–133. https://doi.org/10.1016/j.enggeo.2016.12.018

Ponzo, F.C., Iacovino C., Ditommaso R., Bonano M., Lanari R., Soldovieri F., Cuomo V., Bozzano F., Ciampi P., Rompato M., 2021. Tranport Infrastructure SHM Using Integrated SAR Data and On-Site Vibrational Acquisitions: "Ponte Della Musica-Armando Trovajoli" Case Study. Appl. Sci. 2021, 11, 6504. https://doi.org/10.3390/app11146504

Pratesi, F., Tapete, D., Del Ventisette, C., Moretti, S., 2016. Mapping interactions between geology, subsurface resource exploitation and urban development in transforming cities using InSAR Persistent Scatterers: Two decades of change in Florence, Italy. Appl. Geogr. 77, 20–37. https://doi.org/10.1016/j.apgeog.2016.09.017

Ragnoli, A., De Blasiis, M., Di Benedetto, A., 2018. Pavement distress detection methods: a review. Infrastructures 3 (4), 58. https://doi.org/10.3390/infrastructures3040058

Remondino, F., Nocerino, E., Toschi, I., Menna, F., 2017. A critical review of automated photogrammetric processing of large datasets. https://doi.org/10.5194/isprs-archives-XLII-2-W5-591-2017

Rosi, A., Tofani, V., Agostini, A., Tanteri, L., Stefanelli, C. T., Catani, F., Casagli, N., 2016. Subsidence mapping at regional scale using persistent scatters interferometry (PSI): the case of Tuscany region (Italy). International Journal of Applied Earth Observation and Geoinformation, 52, 328–337. doi: 10.1016/j.jag.2016.07.003

Saad, A.M., Tahar, K.N., 2019. Identification of rut and pothole by using multirotor unmanned aerial vehicle (UAV). Meas. J. Int. Meas. Confed. https://doi.org/10.1016/j.measurement.2019.01.093

Scoular, J., Ghail, R., Mason, P., Lawrence, J., Bellhouse, M., Holley, R., Morgan, T., 2020. Retrospective InSAR Analysis of East London during the Construction of the Lee Tunnel. Remote Sensing, 12, 849. https://doi.org/10.3390/rs12050849

Schuster, R.L., Wieczorek, G.F., 2002. Landslide triggers and types. Book Landslides. 1st Edition, 2002, Routledge. ISBN: 9780203749197

Skempton, A.W, 1953. Discussion in soil stability problems in road engineering, Proc. of the Institution of Civil Engineers, pp.219-280.

Skempton, A.W., MacDonald, D.H., 1956. The allowable settlements of buildings. Proc. Inst. Civ. Eng. https://doi.org/10.1680/ipeds.1956.12202

Segoni, S., Piciullo, L. & Gariano, S.L., 2018. A review of the recent literature on rainfall thresholds for landslide occurrence. Landslides 15, 1483–1501. https://doi.org/10.1007/s10346-018-0966-4

Solari, L., Ciampalini, A., Raspini, F., Bianchini, S., Moretti, S., 2016. PSInSAR analysis in the pisa urban area (Italy): A case study of subsidence related to stratigraphical factors and urbanization. Remote Sens. 8. https://doi.org/10.3390/rs8020120

Solari, L., Del Soldato, M., Bianchini, S., Ciampalini, A., Ezquerro, P., Montalti, R., Raspini, F., Moretti, S., 2018. From ERS 1/2 to Sentinel-1: Subsidence Monitoring in Italy in the Last Two Decades. Frontiers in Earth Science. Vol 6. Doi: 10.3389/feart.2018.00149

Stramondo, S., Bozzano, F., Marra, F., Wegmuller, U., Cinti, F.R., Moro, M., Saroli, M., 2008. Subsidence induced by urbanisation in the city of Rome detected by advanced InSAR technique and geotechnical investigations. Remote Sens. Environ. 112, 3160–3172. https://doi.org/10.1016/j.rse.2008.03.008

Stumpf, A., Malet, J.P., Kerle, N., Niethammer, U., Rothmund, S., 2013. Image-based mapping of surface fissures for the investigation of landslide dynamics. Geomorphology 186, 12–27. https://doi.org/10.1016/j.geomorph.2012.12.010

Tan, Y., Li, Y., 2019. UAV photogrammetry-based 3D road distress detection. ISPRS Int. J. Geo-Information 8. https://doi.org/10.3390/ijgi8090409

Tanyaş, H., van Westen, C. J., Allstadt, K. E., Nowicki Jessee, M. A., Görüm, T., Jibson, R. W., Godt, J. W., Sato, H. P., Schmitt, R. G., Marc, O., Hovius, N., 2017. Presentation and Analysis of a Worldwide Database of Earthquake-Induced Landslide Inventories. JGR Earth Surface. Vol 122 – 10. https://doi.org/10.1002/2017JF004236

Tomás, R., Romero, R., Mulas, J. et al. 2014. Radar interferometry techniques for the study of ground subsidence phenomena: a review of practical issues through cases in Spain. Environ Earth Sci 71, 163–181. https://doi.org/10.1007/s12665-013-2422-z

Tosi, L., Carbognin, L., Teatini, P., Strozzi, T., Wegmüller, U. 2002. Evidence of the present relative land stability of Venice, Italy, from land, sea, and space observations. Geophysical Research Letters, 29, 3-1–3-4

Tosi, L., Teatini, P., Strozzi, T., 2013. Natural versus anthropogenic subsidence of Venice. Scientific Reports, 3, 2710

UNDRR, 2021. URL https://www.undrr.org/implementing-sendai-framework/what-sendai-framework - Last access: September 2021.

Vacca, G., Dessì, A., Sacco, A., 2017. The use of nadir and oblique UAV images for building knowledge. ISPRS Int. J. Geo-Information 6. https://doi.org/10.3390/ijgi6120393

Valagussa, A., Marc, O., Frattini, P., Crosta, G.B., 2019. Seismic and geological controls on earthquake-induced landslide size. Earth Planet. Sci. Lett. 506, 268–281. https://doi.org/10.1016/J.EPSL.2018.11.005

van Asch, Th. W. J., Malet, J.-P., and Bogaard, T. A., 2009. The effect of groundwater fluctuations on the velocity pattern of slow-moving landslides, Nat. Hazards Earth Syst. Sci., 9, 739–749, https://doi.org/10.5194/nhess-9-739-2009

van Westen, C.J., 1993. Training package for Geographic Information Systems for Slope Stability and Zonation, UNESCO-IUGS GARS Project, Chapters 1,2.

Varnes, D.J., 1978. Slope movement: types and processes, in Landslides: Analysis and Control, Washington, Report 176, pp. 11-33.

Wasowski, J., Bovenga, F., 2014. Investigating landslides and unstable slopes with satellite Multi Temporal Interferometry: Current issues and future perspectives. Eng. Geol. 174, 103–138. https://doi.org/10.1016/j.enggeo.2014.03.003

Yin, Y., Wang, F. & Sun, P., 2009. Landslide hazards triggered by the 2008 Wenchuan earthquake, Sichuan, China. Landslides 6, 139–152. https://doi.org/10.1007/s10346-009-0148-5

Zhang, J., van Westen, C. J., Tanyas, H., Mavrouli, O., Ge, Y., Bajrachary, S., Gurung, D. R., Dhital, M. R., and Khanal, N. R., 2019. How size and trigger matter: analyzing rainfall- and earthquake-triggered landslide inventories and their causal relation in the Koshi River basin, central Himalaya, Nat. Hazards Earth Syst. Sci., 19, 1789–1805, https://doi.org/10.5194/nhess-19-1789-2019

## *Chapter 2 – Use of InSAR and UAV for consequence analysis: a literature review*

AASHO, 1962. Road Test-Report61E. HRB, National Research Coun- cil, Washington, D.C., USA.

Akgul, M., Yurtseven, H., Akburak, S., Demir, M., Cigizoglu, H.K., Ozturk, T., Eksi, M., Akay, A.O., 2017. Short term monitoring of forest road pavement degradation using terrestrial laser scanning. Meas. J. Int. Meas. Confed. https://doi.org/10.1016/j.measurement.2017.02.045

Alhasan, A., White, D.J., De Brabanter, K., 2017. Spatial pavement roughness from stationary laser scanning. Int. J. Pavement Eng. 18, 83–96. https://doi.org/10.1080/10298436.2015.1065403

ANAS, 2004. I Quaderni tecnici per la salvaguardia delle infrastrutture V.

ASTM, 2020. ASTM D6433-20 Standard Practice for Roads and Parking Lots Pavement Condition Index Surveys, ASTM International, West Conshohocken, PA, USA.

Baldi, P., Casula, G., Cenni, N., Loddo, F., Pesci, A., 2009. GPS-based monitoring of land subsidence in the Po

Plain (Northern Italy). Earth Planet. Sci. Lett. 288, 204–212. https://doi.org/10.1016/j.epsl.2009.09.023

Bamler, R., Hartl, P., 1998. Synthetic aperture radar interferometry, Inverse Problems, n.14, Publishing Ltd.

Béjar-Pizarro, M., Guardiola-Albert, C., García-Cárdenas, R.P., Herrera, G., Barra, A., Molina, A.L., Tessitore, S., Staller, A., Ortega-Becerril, J.A., García-García, R.P., 2016. Interpolation of GPS and geological data using InSAR deformation maps: Method and application to land subsidence in the alto guadalentín aquifer (SE Spain). Remote Sens. 8. https://doi.org/10.3390/rs8110965

Berardino, P., Fornaro, G., Lanari, R., Sansosti, E., 2002. A new algorithm for surface deformation monitoring based on small baseline differential SAR interferograms. IEEE Trans. Geosci. Remote Sens. 40, 2375–2383. https://doi.org/10.1109/TGRS.2002.803792

Bitelli, G., Bonsignore, F., Del Conte, S., Franci, F., Lambertini, A., Novali, F., Severi, P., Vittuari, L., 2020. Updating the subsidence map of Emilia-Romagna region (Italy) by integration of SAR interferometry and GNSS time series: the 2011–2016 period. Proc. Int. Assoc. Hydrol. Sci. 382, 39–44. https://doi.org/10.5194/piahs-382-39-2020

Bjerrum, L., 1967. Engineering geology of Norwegian normally-consolidated marine clays as related to settlements of buildings. Geotechnique 17, 83–118. https://doi.org/10.1680/geot.1967.17.2.83

Bjerrum, L., 1963. Allowable settlement of structures, in: 3rd European Conference on Soil Mechanics and Foundation ENgineering, Wiesbaden, 2, Brighton, England. pp. 135–137.

Boscardin, M.D., Cording, E.J., 1989. Building Response to Excavation-Induced Settlement. J. Geotech. Eng. 115, 1–21. https://doi.org/10.1061/(ASCE)0733-9410(1989)115:1(1)

Bozzano, F., Esposito, C., Mazzanti, P., Patti, M., Scancella, S., 2018. Imaging multi-age construction settlement behaviour by advanced SAR interferometry. Remote Sens. 10. https://doi.org/10.3390/rs10071137

Bru, G., Herrera, G., Tomás, R., Duro, J., de la Vega, R., Mulas, J., 2013. Control of deformation of buildings affected by subsidence using persistent scatterer interferometry. Struct. Infrastruct. Eng. 9, 188–200. https://doi.org/10.1080/15732479.2010.519710

Budetta, P., De Luca, C., Nappi, M., 2016. Quantitative rockfall risk assessment for an important road by means of the rockfall risk management (RO.MA.) method. Bull. Eng. Geol. Environ. 75, 1377–1397. https://doi.org/10.1007/s10064-015-0798-6

Burland, J.B., Broms, B.B., De Mello, V.F.B., 1977. Behaviour of Foundations and Structures Comportement des Fondations et des Structures. State Art Rep. 363–400.

Burland, J.B., Wroth, C.P., 1974. Settlement of buildings and associated damage, in: Settlement of Structures, Proceedings of the Conference of the British Geotechnical Society. pp. 611–764.

Byun, Y., J. Song, W. Song, and B. Kang., 2016. Conceptual study of a smart docking system for VTOL-UAV. J. Aerosp. Eng. 29 (2): 04015053. https://doi.org/10.1061/(ASCE)AS.1943-5525.0000508

Cardenal, J., Fernández, T., Pérez-García, J.L., Gómez-López, J.M., 2019. Measurement of road surface deformation using images captured from UAVs. Remote Sens. 11, 1–24. https://doi.org/10.3390/rs11121507

Chang, K.T., Chang, J.R., Liu, J.K., 2005. Detection of pavement distresses using 3D laser scanning technology, in: Proceedings of the 2005 ASCE International Conference on Computing in Civil Engineering. https://doi.org/10.1061/40794(179)103

Cigna, F., Osmanoğlu, B., Cabral-Cano, E., Dixon, T.H., Ávila-Olivera, J.A., Garduño-Monroy, V.H., DeMets, C., Wdowinski, S., 2012. Monitoring land subsidence and its induced geological hazard with Synthetic Aperture Radar Interferometry: A case study in Morelia, Mexico. Remote Sens. Environ. 117, 146–161. https://doi.org/10.1016/j.rse.2011.09.005

Coenen, T.B.J., Golroo, A., 2017. A review on automated pavement distress detection methods. https://doi.org/10.1080/23311916.2017.1374822

Corominas, J., van Westen, C., Frattini, P., Cascini, L., Malet, J.P., Fotopoulou, S., Catani, F., Van Den Eeckhaut, M., Mavrouli, O., Agliardi, F., Pitilakis, K., Winter, M.G., Pastor, M., Ferlisi, S., Tofani, V., Hervás, J., Smith, J.T., 2014. Recommendations for the quantitative analysis of landslide risk. Bull. Eng. Geol. Environ. 73, 209–263. https://doi.org/10.1007/s10064-013-0538-8

Costantini, M., 1998. A novel phase unwrapping method based on network programming, in IEEE Transactions on Geoscience and Remote Sensing, vol. 36, no. 3, pp. 813-821, May 1998, doi: 10.1109/36.673674.

Costantini, M., Falco, S., Malvarosa, F., Minati, F., 2008. A new method for identification and analysis of persistent scatterers in series of sar images. Int. Geosci. Remote Sens. Symp. 2. https://doi.org/10.1109/IGARSS.2008.4779025

Costantini, M., Falco, S., Malvarosa, F., Minati, F., Trillo, F., 2009. Method of persistent scatterer pairs (PSP) and high resolution SAR interferometry. Int. Geosci. Remote Sens. Symp. 3, III-904-III–907. https://doi.org/10.1109/IGARSS.2009.5417918

Crosetto, M., Monserrat, O., Cuevas-González, M., Devanthéry, N., Crippa, B., 2016. Persistent Scatterer Interferometry: A review. ISPRS J. Photogramm. Remote Sens. 115, 78–89. https://doi.org/10.1016/j.isprsjprs.2015.10.011

Cubero-Fernandez, A., Rodriguez-Lozano, F.J., Villatoro, R., Olivares, J., Palomares, J.M., 2017. Efficient pavement crack detection and classification. Eurasip J. Image Video Process. 2017. https://doi.org/10.1186/s13640-017-0187-0

De Blasiis, M.R., Di Benedetto, A., Fiani, M., 2020. Mobile Laser Scanning Data for the Evaluation of Pavement Surface Distress. Remote Sens. 12, 942. https://doi.org/10.3390/rs12060942

Delair, 2021. URL https://delair.aero/delair-commercial-drones/professional-mapping-drone-delair-ux11/ - Last access: September 2021.

Del Ventisette, C., Ciampalini, A., Manunta, M., Calò, F., Paglia, L., Ardizzone, F., Mondini, A.C., Reichenbach, P., Mateos, R.M., Bianchini, S., Garcia, I., Füsi, B., Deák, Z.V., Rádi, K., Graniczny, M., Kowalski, Z., Piatkowska, A., Przylucka, M., Retzo, H., Strozzi, T., Colombo, D., Mora, O., Sánchez, F., Herrera, G., Moretti, S., Casagli, N., Guzzetti, F., 2013. Exploitation of large archives of ERS and ENVISAT C-band SAR data to characterize ground deformations. Remote Sens. 5, 3896–3917. https://doi.org/10.3390/rs5083896

del Ventisette, C., Solari, L., Raspini, F., Ciampalini, A., di Traglia, F., Moscatelli, M., Pagliaroli, A., Moretti, S., 2015. Use of PSInSAR data to map highly compressible soil layers. Geol. Acta 13, 309–323. https://doi.org/10.1344/GeologicaActa2015.13.4.4

DJI, 2021. URL https://www.dji.com/ - Last access: September 2021.

Donnini, M., Napolitano, E., Salvati, P., Ardizzone, F., Bucci, F., Fiorucci, F., Santangelo, M., Cardinali, M., Guzzetti, F., 2017. Impact of event landslides on road networks: a statistical analysis of two Italian case studies. Landslides 14, 1521–1535. https://doi.org/10.1007/s10346-017-0829-4

ENAC, 2021. URL https://www.enac.gov.it/sicurezza-aerea/droni - Last access: September 2021.

ESA, 2021. URL https://sentinels.copernicus.eu/web/sentinel/user-guides/sentinel-1-sar/product-overview/interferometry - Last access: September 2021.

Ezquerro, P., Del Soldato, M., Solari, L., Tomás, R., Raspini, F., Ceccatelli, M., Fernández-Merodo, J.A., Casagli, N., Herrera, G., 2020. Vulnerability Assessment of Buildings due to Land Subsidence using InSAR Data in the Ancient Historical City of Pistoia (Italy). Sensors 20, 2749. https://doi.org/10.3390/s20102749

Fell, R., Corominas, J., Bonnard, C., Cascini, L., Leroi, E., Savage, W.Z., 2008. Guidelines for landslide susceptibility, hazard and risk zoning for land use planning. Eng. Geol. 102, 85–98. https://doi.org/10.1016/j.enggeo.2008.03.022

Ferlisi, S., Marchese, A., Peduto, D., 2020a. Quantitative analysis of the risk to road networks exposed to slow-moving landslides: a case study in the Campania region (southern Italy). Landslides 2020. https://doi.org/10.1007/s10346-020-01482-8

Ferlisi, S., Nicodemo, G., Peduto, D., Negulescu, C., and Grand- jean, G., 2020b. Deterministic and probabilistic analyses of the 3D re- sponse of masonry buildings to imposed settlement troughs, GeoRisk, https://doi.org/10.1080/17499518.2019.1658880

Ferretti, A., Fumagalli, A., Novali, F., Prati, C., Rocca, F., Rucci, A., 2011. A new algorithm for processing interferometric data-stacks: SqueeSAR, in: IEEE Transactions on Geoscience and Remote Sensing. pp. 3460–3470. https://doi.org/10.1109/TGRS.2011.2124465

Ferretti, A., Monti-Guarnieri, A., Prati, C., Rocca, F., Massonet, D., 2007. InSAR Principles: Guidelines for SAR Interferometry Processing and Interpretation, European Space Agency.

Ferretti, A., Prati, C., Rocca, F., 2000. Nonlinear subsidence rate estimation using permanent scatterers in differential SAR interferometry, IEEE Transactions on Geoscience and Remote Sensing, 38(5), 2202–2212.

Ferretti, A., Prati, C., Rocca, F., 2001. Permanent scatterers in SAR interferometry. IEEE Trans. Geosci. Remote

Sens. 39, 8–20. https://doi.org/10.1109/36.898661

Fotopoulou, S.D., Pitilakis, K.D., 2013. Vulnerability assessment of reinforced concrete buildings subjected to seismically triggered slow-moving earth slides. Landslides 10, 563–582. https://doi.org/10.1007/s10346-012-0345-5

Franceschetti, G., Lanari, R. (1999), Synthetic Aperture Radar Processing. Boca Raton, FL: CRC Press.

Galli, M., Guzzetti, F., 2007. Landslide vulnerability criteria: A case study from Umbria, central Italy. Environ. Manage. 40, 649–664. https://doi.org/10.1007/s00267-006-0325-4

Gavilán, M., Balcones, D., Marcos, O., Llorca, D.F., Sotelo, M.A., Parra, I., Ocaña, M., Aliseda, P., Yarza, P., Amírola, A., 2011. Adaptive road crack detection system by pavement classification. Sensors. https://doi.org/10.3390/s111009628

George, K.P., Rajagopal, A.S., Lim, L.K., 1989. Models for predicting pavement deterioration. Transp. Res. Rec. 1–7.

Gharaibeh, N.G., Lindholm, D. (Brooke), 2014. A condition assessment method for roadside assets. Struct. Infrastruct. Eng. 10, 409–418. https://doi.org/10.1080/15732479.2012.757330

Giordan, D., Adams, M.S., Aicardi, I., Alicandro, M., Allasia, P., Baldo, M., De Berardinis, P., Dominici, D., Godone, D., Hobbs, P., Lechner, V., Niedzielski, T., Piras, M., Rotilio, M., Salvini, R., Segor, V., Sotier, B., Troilo, F., 2020. The use of unmanned aerial vehicles (UAVs) for engineering geology applications. Bull. Eng. Geol. Environ. 79, 3437–3481. https://doi.org/10.1007/s10064-020-01766-2

Greenwood, W.W., Lynch, J.P., Zekkos, D., 2019. Applications of UAVs in civil infrastructure. J. Infrastruct. Syst. 25, 1–21. https://doi.org/10.1061/(ASCE)IS.1943-555X.0000464

Guan, H., Li, J., Yu, Y., Chapman, M., Wang, C., 2015. Automated road information extraction from mobile laser scanning data. IEEE Trans. Intell. Transp. Syst. 16, 194–205. https://doi.org/10.1109/TITS.2014.2328589

Hackel, T., Wegner, J.D., Schindler, K., 2016. Contour detection in unstructured 3D point clouds, in: Proceedings of the IEEE Computer Society Conference on Computer Vision and Pattern Recognition. pp. 1610–1618. https://doi.org/10.1109/CVPR.2016.178

Hatmoko, J.U.D., Setiadji, B.H., Wibowo, M.A., 2019. Investigating causal factors of road damage: a case study. MATEC Web Conf. 258, 02007. https://doi.org/10.1051/matecconf/201925802007

Herrera, G., Fernández, J.A., Tomás, R., Cooksley, G., Mulas, J., 2009. Advanced interpretation of subsidence in Murcia (SE Spain) using A-DInSAR data - Modelling and validation. Nat. Hazards Earth Syst. Sci. 9, 647–661. https://doi.org/10.5194/nhess-9-647-2009

Herrera, G., Tomás, R., Monells, D., Centolanza, G., Mallorquí, J.J., Vicente, F., Navarro, V.D., Lopez-Sanchez, J.M., Sanabria, M., Cano, M., Mulas, J., 2010. Analysis of subsidence using TerraSAR-X data: Murcia case study. Eng. Geol. 116, 284–295. https://doi.org/10.1016/j.enggeo.2010.09.010

Hervieu, A., Soheilian, B., 2013. Semi-automatic road/pavement modeling using mobile laser scanning.

Ho Tong Minh, D., Hanssen, R., Rocca, F., 2020. Radar Interferometry: 20 Years of Development in Time Series Techniques and Future Perspectives. Remote Sens., 12, 1364. https://doi.org/10.3390/rs12091364

Hooper, A., Bekaert, D., Spaans, K., Arikan, M., 2012. Recent advances in SAR interferometry time series analysis for measuring crustal deformation. Tectonophysics 514–517, 1–13. https://doi.org/10.1016/j.tecto.2011.10.013

Hooper, A., Zebker, H., Segall, P., Kampes, B., 2004. A new method for measuring deformation on volcanoes and other natural terrains using InSAR persistent scatterers. Geophys. Res. Lett. 31, 1–5. https://doi.org/10.1029/2004GL021737

Hooper, A.J., 2008. A multi-temporal InSAR method incorporating both persistent scatterer and small baseline approaches. Geophys. Res. Lett. 35, 1–5. https://doi.org/10.1029/2008GL034654

Hu, B., Chen, J., Zhang, X., 2019. Monitoring the land subsidence area in a coastal urban area with InSAR and GNSS. Sensors (Switzerland). https://doi.org/10.3390/s19143181

ICAO, 2021. URL https://www.icao.int/Pages/default.aspx - Last access: September 2021.

Inzerillo, L., Di Mino, G., Roberts, R., 2018. Image-based 3D reconstruction using traditional and UAV datasets for analysis of road pavement distress. Autom. Constr. 96, 457–469. https://doi.org/10.1016/j.autcon.2018.10.010

Karila, K., Karjalainen, M., Hyyppä, J., Koskinen, J., Saaranen, V., Rouhiainen, P., 2013. A comparison of precise leveling and Persistent Scatterer SAR Interferometry for building subsidence rate measurement. ISPRS Int. J.

Geo-Information. https://doi.org/10.3390/ijgi2030797

Kim, H., Sim, S.H., Cho, S., 2015. Unmanned aerial vehicle (UAV)-powered concrete crack detection based on digital image processing. Int. Conf. Adv. Exp. Struct. Eng. 2015-Augus.

Kumar, P., Lewis, P., Mcelhinney, C.P., Rahman, A.A., 2015. An algorithm for automated estimation of road roughness from mobile laser scanning data. Photogramm. Rec. 30, 30–45. https://doi.org/10.1111/phor.12090

Lagomarsino, S, Giovinazzi, S., 2006. Macroseismic and mechanical models for the vulnerability and damage assessment of current buildings. Bull Earthq Eng 4(4):415–443.

Lissak, C., Bartsch, A., De Michele, M., Gomez, C., Maquaire, O., Raucoules, D., Roulland, T., 2020. Remote Sensing for Assessing Landslides and Associated Hazards. Surv. Geophys. https://doi.org/10.1007/s10712-020-09609-1

Maas, H.G., Vosselman, G., 1999. Two algorithms for extracting building models from raw laser altimetry data. ISPRS J. Photogramm. Remote Sens. 54, 153–163. https://doi.org/10.1016/S0924-2716(99)00004-0

Mansour, M.F., Morgenstern, N.R., Martin, C.D., 2011. Expected damage from displacement of slow-moving slides. Landslides 8, 117–131. https://doi.org/10.1007/s10346-010-0227-7

Martone, M., 2019. Onboard Quantization for Interferometric and Multichannel Synthetic Aperture Radar (SAR) Systems. Ph.D. Thesis. November 2019.

Mavrouli, O., Corominas, J., Ibarbia, I., Alonso, N., Jugo, I., Ruiz, J., Luzuriaga, S., Navarro, J.A., 2019. Integrated risk assessment due to slope instabilities in the roadway network of Gipuzkoa, Basque Country. Nat. Hazards Earth Syst. Sci. 19, 399–419. https://doi.org/10.5194/nhess-19-399-2019

Mavrouli, O., Fotopoulou, S., Pitilakis, K., Zuccaro, G., Corominas, J., Santo, A., Cacace, F., De Gregorio, D., Di Crescenzo, G., Foerster, E., Ulrich, T., 2014. Vulnerability assessment for reinforced concrete buildings exposed to landslides. Bull. Eng. Geol. Environ. 73, 265–289. https://doi.org/10.1007/s10064-014-0573-0

Mosconi, A., Bagliani, A., Marzonati, D., Cremonesi, A., Ferretti, A., Colombo, D., Novali, F., Tamburini, A., 2010. Use of Satellite Radar Data for Surface Deformation Monitoring: A Wrap-Up After 10 Years of Experimentation, SPE Annual Technical Conference and Exhibition held in Florence, Italy, 19-22 September 2010.

Nappo, N., Mavrouli, O., Nex, F., van Westen, C., Gambillara, R., Michetti, A.M., 2021b. Use of UAV-based photogrammetry products for semi-automatic detection and classification of asphalt road damage in landslide-affected areas. Eng. Geol. 294, 106363. https://doi.org/10.1016/j.enggeo.2021.106363

Nappo, N., Peduto, D., Mavrouli, O., van Westen, C.J., Gullà, G., 2019. Slow-moving landslides interacting with the road network: Analysis of damage using ancillary data, in situ surveys and multi-source monitoring data. Eng. Geol. 260, 105244. https://doi.org/10.1016/j.enggeo.2019.105244

Nappo, N., Peduto, D., Polcari, M., Livio, F., Ferrario, M.F., Comerci, V., Stramondo, S., Michetti, A.M., 2021a. Subsidence in Como historic centre (northern Italy): assessment of building vulnerability combining hydrogeological and stratigraphic features, Cosmo-SkyMed InSAR and damage data. Int. J. Disaster Risk Reduct. 56, 102115. https://doi.org/10.1016/j.ijdrr.2021.102115

Negulescu, C, Foerster, E., 2010. Parametric studies and quantitative assessment of the vulnerability of a RC frame building exposed to differential settlements. Nat Hazards Earth Syst Sci 10(9):1781–1792

Negulescu, C., Ulrich, T., Baills, A., Seyedi, D.M., 2014. Fragility curves for masonry structures submitted to permanent ground displacements and earthquakes. Nat. Hazards 74, 1461–1474. https://doi.org/10.1007/s11069-014-1253-x

Nex, F., Remondino, F., 2014. UAV for 3D mapping applications: A review. Appl. Geomatics. https://doi.org/10.1007/s12518-013-0120-x

Nicodemo, G., Peduto, D., Ferlisi, S., 2020. Building damage assessment and settlement monitoring in subsidence-affected urban areas: case study in the Netherlands. Proc. Int. Assoc. Hydrol. Sci. 382, 651–656. https://doi.org/10.5194/piahs-382-651-2020

Nicodemo, G., Peduto, D., Ferlisi, S., Gullà, G., Borrelli, L., Fornaro, G., Reale, D., 2017. Analysis of Building Vulnerability to Slow-Moving Landslides via A-DInSAR and Damage Survey Data. Adv. Cult. Living with Landslides 2, 899–907. https://doi.org/10.1007/978-3-319-53498-5_102

NOAA, 2021. URL https://oceanservice.noaa.gov/facts/remotesensing.html - Last access: September 2021.

Oliveira, H., Correia, P.L., 2013. Automatic road crack detection and characterization. IEEE Trans. Intell. Transp. Syst. 14, 155–168. https://doi.org/10.1109/TITS.2012.2208630

Ouyang, W., Xu, B., 2013. Pavement cracking measurements using 3D laser-scan images. Meas. Sci. Technol. https://doi.org/10.1088/0957-0233/24/10/105204

Ozdemir, U., Aktas, Y.O., Vuruskan, A., Dereli, Y., Tarhan, A.F., Demirbag, K., Erdem, A., Kalaycioglu, G.D., Ozkol, I., Inalhan, G., 2014. Design of a Commercial Hybrid VTOL UAV System. J. Intell. Robot. Syst. 74, 371–393. https://doi.org/10.1007/s10846-013-9900-0

Pawar, P.R., Mathew, A.T., Saraf, M.R., 2018. IRI (International Roughness Index): An Indicator of Vehicle Response, in: Materials Today: Proceedings. Elsevier Ltd, pp. 11738–11750. https://doi.org/10.1016/j.matpr.2018.02.143

Peduto, D., Cascini, L., Arena, L., Ferlisi, S., Fornaro, G., Reale, D., 2015. A general framework and related procedures for multiscale analyses of DInSAR data in subsiding urban areas. ISPRS J. Photogramm. Remote Sens. 105, 186–210. https://doi.org/10.1016/j.isprsjprs.2015.04.001

Peduto, D., Elia, F., Montuori, R., 2018. Probabilistic analysis of settlement-induced damage to bridges in the city of Amsterdam (The Netherlands). Transp. Geotech. 14, 169–182. https://doi.org/10.1016/j.trgeo.2018.01.002

Peduto, D., Ferlisi, S., Nicodemo, G., Reale, D., Pisciotta, G., Gullà, G., 2017a. Empirical fragility and vulnerability curves for buildings exposed to slow-moving landslides at medium and large-scales. Landslides 14, 1993–2007. https://doi.org/10.1007/s10346-017-0826-7

Peduto, D., Giangreco, C., Venmans, A.A.M., 2020. Differential settlements affecting transition zones between bridges and road embankments on soft soils: Numerical analysis of maintenance scenarios by multi-source monitoring data assimilation. Transp. Geotech. 24, 100369. https://doi.org/10.1016/j.trgeo.2020.100369

Peduto, D., Korff, M., Nicodemo, G., Marchese, A., Ferlisi, S., 2019. Empirical fragility curves for settlement-affected buildings: Analysis of different intensity parameters for seven hundred masonry buildings in The Netherlands. Soils Found. 59, 380–397. https://doi.org/10.1016/j.sandf.2018.12.009

Peduto, D., Nicodemo, G., Maccabiani, J., Ferlisi, S., 2017c. Multi-scale analysis of settlement-induced building damage using damage surveys and DInSAR data: A case study in The Netherlands. Eng. Geol. 218, 117–133. https://doi.org/10.1016/j.enggeo.2016.12.018

Pepe, A., Calò, F., 2017. A review of interferometric synthetic aperture RADAR (InSAR) multi-track approaches for the retrieval of Earth’s Surface displacements. Appl. Sci. 7. https://doi.org/10.3390/app7121264

Petrucci, O., Gullà, G., 2010. A simplified method for assessing landslide damage indices. Nat. Hazards 52, 539–560. https://doi.org/10.1007/s11069-009-9398-8

Postance, B., Hillier, J., Dijkstra, T., Dixon, N., 2017. Extending natural hazard impacts: An assessment of landslide disruptions on a national road transportation network. Environ. Res. Lett. 12. https://doi.org/10.1088/1748-9326/aa5555

Powell, L., Satheeshkumar, K.G., 2017. Automated road distress detection, in: Proceedings of IEEE International Conference on Emerging Technological Trends in Computing, Communications and Electrical Engineering, ICETT 2016. Institute of Electrical and Electronics Engineers Inc. https://doi.org/10.1109/ICETT.2016.7873662

Pratesi, F., Tapete, D., Del Ventisette, C., Moretti, S., 2016. Mapping interactions between geology, subsurface resource exploitation and urban development in transforming cities using InSAR Persistent Scatterers: Two decades of change in Florence, Italy. Appl. Geogr. 77, 20–37. https://doi.org/10.1016/j.apgeog.2016.09.017

Puan, O.C., Mustaffar, M., Ling, T.C., 2007. Automated pavement imaging program (apip) for pavement cracks classification and quantification, Malaysian Journal of Civil Engineering.

Ragnoli, A., De Blasiis, M., Di Benedetto, A., 2018. Pavement Distress Detection Methods: A Review. Infrastructures 3, 58. https://doi.org/10.3390/infrastructures3040058

Raspini, F., Bardi, F., Bianchini, S., Ciampalini, A., Del Ventisette, C., Farina, P., Ferrigno, F., Solari, L., Casagli, N., 2017. The contribution of satellite SAR-derived displacement measurements in landslide risk management practices. Nat. Hazards 86, 327–351. https://doi.org/10.1007/s11069-016-2691-4

Remondo, J., Bonachea, J., Cendrero, A., 2005. A statistical approach to landslide risk modelling at basin scale: from landslide susceptibility to quantitative risk assessment. Landslides 2:321–328

Remondino, F., Nocerino, E., Toschi, I., Menna, F., 2017. A critical review of automated photogrammetric processing of large datasets. https://doi.org/10.5194/isprs-archives-XLII-2-W5-591-2017

Saad, A.M., Tahar, K.N., 2019. Identification of rut and pothole by using multirotor unmanned aerial vehicle (UAV). Meas. J. Int. Meas. Confed. https://doi.org/10.1016/j.measurement.2019.01.093

Saeidi, A., Deck, O., Verdel, T., 2013. Comparison of Building Damage Assessment Methods for Risk Analysis in Mining Subsidence Regions. Geotech. Geol. Eng. 31, 1073–1088. https://doi.org/10.1007/s10706-013-9633-7

Saeidi, A., Deck, O., Verdel, T., 2009. Development of building vulnerability functions in subsidence regions from empirical methods. Eng. Struct. 31, 2275–2286. https://doi.org/10.1016/j.engstruct.2009.04.010

Schnebele, E., Tanyu, B.F., Cervone, G., Waters, N., 2015. Review of remote sensing methodologies for pavement management and assessment. Eur. Transp. Res. Rev. 7. https://doi.org/10.1007/s12544-015-0156-6

Skempton, A.W., MacDonald, D.H., 1956. The allowable settlements of buildings. Proc. Inst. Civ. Eng. https://doi.org/10.1680/ipeds.1956.12202

Solari, L., Ciampalini, A., Raspini, F., Bianchini, S., Moretti, S., 2016. PSInSAR analysis in the pisa urban area (Italy): A case study of subsidence related to stratigraphical factors and urbanization. Remote Sens. 8. https://doi.org/10.3390/rs8020120

Stocker, C., Bennet, R., Nex, F., Gerke, M., Zevenberg, J., 2017. Review of the current state of UAV regulations. Remote Sensing. 9(5), 459; https://doi.org/10.3390/rs9050459

Stramondo, S., Bozzano, F., Marra, F., Wegmuller, U., Cinti, F.R., Moro, M., Saroli, M., 2008. Subsidence induced by urbanisation in the city of Rome detected by advanced InSAR technique and geotechnical investigations. Remote Sens. Environ. 112, 3160–3172. https://doi.org/10.1016/j.rse.2008.03.008

Tan, Y., Li, Y., 2019. UAV photogrammetry-based 3D road distress detection. ISPRS Int. J. Geo-Information 8. https://doi.org/10.3390/ijgi8090409

Timoshenko, S., 1957. Strength of material-part I. D. van No- strand Co, London.

Tomás, R., Romero, R., Mulas, J., Marturià, J.J., Mallorquí, J.J., Lopez-Sanchez, J.M., Herrera, G., Gutiérrez, F., González, P.J., Fernández, J., Duque, S., Concha-Dimas, A., Cocksley, G., Castañeda, C., Carrasco, D., Blanco, P., 2014. Radar interferometry techniques for the study of ground subsidence phenomena: A review of practical issues through cases in Spain. Environ. Earth Sci. 71, 163–181. https://doi.org/10.1007/s12665-013-2422-z

TRE Altamira, 2021. URL https://site.tre-altamira.com/ - Last access: September 2021.

Uhlemann, S., Smith, A., Chambers, J., Dixon, N., Dijkstra, T., Haslam, E., Meldrum, P., Merritt, A., Gunn, D., Mackay, J., 2016. Assessment of ground-based monitoring techniques applied to landslide investigations. Geomorphology 253, 438–451. https://doi.org/10.1016/J.GEOMORPH.2015.10.027

Van Der Horst, B.B., Lindenbergh, R.C., Puister, S.W.J., 2019. Mobile laser scan data for road surface damage detection, in: International Archives of the Photogrammetry, Remote Sensing and Spatial Information Sciences - ISPRS Archives. https://doi.org/10.5194/isprs-archives-XLII-2-W13-1141-2019

van Westen, C.J., 2004. Geo-Information tools for Landslide Risk Assessment. An overview of recent developments.

van Westen, C.J., 2013. Remote Sensing and GIS for Natural Hazards Assessment and Disaster Risk Management. Treatise Geomorphol. 3, 259–298. https://doi.org/10.1016/B978-0-12-374739-6.00051-8

Vertical Technologies, 2021. URL https://www.deltaquad.com - Last access: September 2021.

Vosselman, G., & Maas, H. G. (Eds.), 2010. Airborne and terrestrial laser scanning. CRC Press.

Wang, Y.L., Shi, B., Zhang, T.L. et al. Introduction to an FBG-based inclinometer and its application to landslide monitoring. J Civil Struct Health Monit 5, 645–653 (2015). https://doi.org/10.1007/s13349-015-0129-4

Wang, W., Wang, M., Li, H., Zhao, H., Wang, K., He, C., Wang, J., Zheng, S., Chen, J., 2019. Pavement crack image acquisition methods and crack extraction algorithms: A review. In: Journal of Traffic and Transportation Engineering (English Edition) (Vol. 6, Issue 6, pp. 535–556). Periodical Offices of Chang- an University. https://doi.org/ 10.1016/j.jtte.2019.10.001

Wasowski, J., Bovenga, F., 2014. Investigating landslides and unstable slopes with satellite Multi Temporal Interferometry: Current issues and future perspectives. Eng. Geol. 174, 103–138. https://doi.org/10.1016/j.enggeo.2014.03.003

Weinmann, M., Jutzi, B., Mallet, C., 2013. Feature relevance assessment for the semantic interpretation of 3D point cloud data. ISPRS Ann. Photogramm. Remote Sens. Spat. Inf. Sci. 2, 313–318. https://doi.org/10.5194/isprsannals-II-5-W2-313-2013

Werner, C., Wegmüller, U., Strozzi, T., Wiesmann, A., 2003. Interferometric Point Target Analysis for Deformation Mapping, in: International Geoscience and Remote Sensing Symposium (IGARSS). pp. 4362–4364. https://doi.org/10.1109/igarss.2003.1295516

Wiebe, D., Cox, D., 2014. Application of fragility curves to estimate building damage and economic loss at a community scale: A case study of Seaside, Oregon. Nat. Hazards, 71, 2043–2061. doi:10.1007/s11069- 013-0995-1

Winter, M.G., 2019. Laboratory investigation of the impact force of debris flow on a passable structure, The XVII European Conference on Soil Mechanics and Geotechnical Engineering (XVII ECSMGE-2019). https://doi.org/10.32075/17ECSMGE-2019-1118

Winter, M.G., Shearer, B., Palmer, D., Peeling, D., Harmer, C., Sharpe, J., 2016. The Economic Impact of Landslides and Floods on the Road Network. Procedia Eng. 143, 1425–1434. https://doi.org/10.1016/j.proeng.2016.06.168

Zak, J., 2016. On laser scanning, pavement surface roughness and international roughness index in highway construction. https://doi.org/10.14311/ee.2016.294

Zhang, C., Elaksher, A., 2012. An unmanned aerial vehicle-based imaging system for 3D measurement of unpaved road surface distresses. Comput. Civ. Infrastruct. Eng. https://doi.org/10.1111/j.1467-8667.2011.00727.x

Zhang, L., Ng, A.M.Y., 2005. Probabilistic limiting tolerable displacements for serviceability limit state design of foundations. Geotechnique 55, 151–161. https://doi.org/10.1680/geot.2005.55.2.151

## *Chapter 3 – InSAR for multi-scale monitoring of subsidence: the case of Como (N Italy)*

Apuani, T., Cancelli, A., Cancelli, P., 2000. Hydrogeological and geotechnical investigations along the shoreline of the town of Como, Italy, in: D.P. Moore, O. Hungr (Eds.), “Engineering Geology and Environment” Proc. 8th. Cong, Intern. Assoc. Engineering Geology.

Bajni, G., Apuani, T., Beretta, G. Pietro, 2019. Hydro-geotechnical modelling of subsidence in the Como urban area. Eng. Geol. 257, 105144. https://doi.org/10.1016/j.enggeo.2019.105144

Beretta, G.P., Denti, E., Fumagalli, L., Sala, P., 1986. Note sull’idrogeologia delle città di Como e Lecco, Mem. Soc. Geol. Ital. 32, 235–251.

Bernoulli, D., Bertotti, G., Zingg, A., 1989. Northward thrusting of the gonfolite lombarda («South-Alpine molasse») onto the mesozoic sequence of the lombardian alps; implications for the deformation history of the southern alps, Eclogae Geol. Helv. 82 (3) (1989) 841–856.

Bini, A., 1987. L’apparato glaciale wurmiano di Como, Unpublished Ph. D. thesis, University of Milan, Italy.

Bini, A., 1993. Geologia del Quaternario e geomorfologia della Piana di Como, in: M. Uboldi (Ed.), Carta Archeologica Della Lombardia Vol. III, Franco Cosimo Panini, pp. 59–63.

Bini, A., 1996. La regolazione del Lago di Como: problemi e proposte. Atti del convegno. Villa Olmo, Como, 19 April 1996, Kiwanis International Europe.

Bini, A., Castelletti, L., 1986. Geologia e paleobotanica di un sedimento olocenico nel sottosuolo di piazza Roma a Como, Nat. Brescia. 23, 357–363.

Burland, J.B., Broms, B.B., De Mello, V.F.B., 1977. Behaviour of Foundations and Structures Comportement des Fondations et des Structures. State Art Rep. 363–400.

Caniggia, G., 1986. Lettura di una città: Como, p. 46.

Cascini, L., Fornaro, G., Peduto, D., 2010b. Advanced low- and full-resolution DInSAR map generation for slow-moving landslide analysis at different scales. Eng. Geol. 112, 29–42. https://doi.org/10.1016/j.enggeo.2010.01.003

Cascini, L., Peduto, D., Reale, D., Arena, L., Ferlisi, S., Verde, S., Fornaro, G., 2013. Detection and monitoring of facilities exposed to subsidence phenomena via past and current generation SAR sensors. J. Geophys. Eng. 10. https://doi.org/10.1088/1742-2132/10/6/064001

Castelletti, L., Orombelli, G., 1986. Una nuova data 14C per la storia della deglaciazione del bacino del Lago di Como, Geogr. Fis. Din. Quaternaria 9, 56–58.

Comerci, V., 2004. Evoluzione geologica e ambientale recente in aree subsidenti, esempio di studio nella citt`a di Como, Universit`a degli Studi dell'Insubria (Ph.D. Thesis).

Comerci, V., Capelletti, S., Michetti, A.M., Rossi, S., Serva, L., Vittori, E., 2007. Land subsidence and Late Glacial environmental evolution of the Como urban area (Northern Italy). Quat. Int. 173–174, 67–86. https://doi.org/10.1016/j.quaint.2007.06.014

Comune di Como, 1980. Relazione di sintesi della Commissione per lo Studio dei Fenomeni di Subsidenza, Documenti e Ricerche 34 (1980).

Costantini, M., 1998. A novel phase unwrapping method based on network programming, IEEE Trans. Geosci. Rem. Sens. 36 (1998) 813–821

Costantini, M., Falco, S., Malvarosa, F., Minati, F., 2008. A new method for identification and analysis of persistent scatterers in series of sar images. Int. Geosci. Remote Sens. Symp. 2. https://doi.org/10.1109/IGARSS.2008.4779025

Costantini, M., Falco, S., Malvarosa, F., Minati, F., Trillo, F., 2009. Method of persistent scatterer pairs (PSP) and high resolution SAR interferometry. Int. Geosci. Remote Sens. Symp. 3, III-904-III–907. https://doi.org/10.1109/IGARSS.2009.5417918

Del Ventisette, C., Ciampalini, A., Manunta, M., Calò, F., Paglia, L., Ardizzone, F., Mondini, A.C., Reichenbach, P., Mateos, R.M., Bianchini, S., Garcia, I., Füsi, B., Deák, Z.V., Rádi, K., Graniczny, M., Kowalski, Z., Piatkowska, A., Przylucka, M., Retzo, H., Strozzi, T., Colombo, D., Mora, O., Sánchez, F., Herrera, G., Moretti, S., Casagli, N., Guzzetti, F., 2013. Exploitation of large archives of ERS and ENVISAT C-band SAR data to characterize ground deformations. Remote Sens. 5, 3896–3917. https://doi.org/10.3390/rs5083896

Farrar, D.E.; Glauber, R.R. 1967. Multicollinearity in Regression Analysis: The Problem Revisited. Rev. Econ. Stat. 1967, 49, 92.

Ferrario, M.F., Bonadeo, L., Brunamonte, F., Livio, F., Martinelli, E., Michetti, A.M., Censi Neri, P., Chiessi, V., Comerci, V., Höbig, N., 2015a. Late Quaternary environmental evolution of the Como urban area (Northern Italy): A multidisciplinary tool for risk management and urban planning. Eng. Geol. 193, 384–401. https://doi.org/10.1016/j.enggeo.2015.05.013

Ferrario, M.F.; Brunamonte, F.; Caccia, A.; Livio, F.; Martinelli, E.; Mazzola, E.; Michetti, A.M.; Terrana, S., 2015b. Buried Landscapes: Geoarchaeology of the Roman Harbor of Como (N Italy). Alp. Mediterr. Quat., 28, 111–120.

Geoportale Regione Lombardia, 2021. URL http://www.geoportale.regione.lombardia.it/ - Last acces: September 2021.

Goldstein, R., Werner, C., 1998. Radar interferogram filtering for geophysical applications, Geophys, Res. Lett. 25 (1998) 4035–4038.

Krivoruchko, K., 2012. Empirical Bayesian Kriging, Esri, Redlands, CA, USA, 2012.

Livio, F., Berlusconi, A., Chunga, K., Michetti, A.M., Sileo, G., 2011. New stratigraphic and structural evidence for Late Pleistocene surface faulting along the Monte Olimpino Backthrust (Lombardia, N Italy). Rend. Online Soc. Geol. Ital. 14, 17–25. https://doi.org/10.3301/ROL.2011.03

Luraschi, G., 1987. Como romana: le mura. Como nell'antichità, Soc. Arch. Com., 103–112.

Martinelli, E., Castelletti, L., Ferrario, M.F., Livio, F., Michetti, A.M., 2019. Archeologia e indagini stratigrafiche per la ricostruzione della linea di costa e delle aree portuali della Como romana, Rivista archeologica dell'antica provincia e diocesi di Como 200.

M.A.T.T.M., 2010. Linee guida per l'analisi di dati interferometrici satellitari in aree soggette a dissesti idrogeologici, Versione1.0, Piano Straordinario di Telerilevamento Ambientale (PST-A), Lotto 2.

Michetti, A.M., 2014a. Como 075 Sheet of the Geological Map of Italy, 1:50.000 scale, Progetto Cartografia Geologica - CARG Project, ISPRA Servizio Geologico d'Italia. http://www.isprambiente.gov.it/Media/carg/75_COMO/Foglio.html

Michetti, A.M., Giardina, F., Livio, F., Mueller, K., Serva, L., Sileo, G., Rogledi, S., 2012. Active compressional tectonics, Quaternary capable faults, and the seismic landscape of the Po Plain (N Italy), Ann. Geophys.

Michetti, A.M., Livio, F., Pasquarè, F.A., Vezzoli, L., Bini, A., Bernoulli, D., Sciunnach, D., 2014b. Note Illustrative Della Carta Geologica d'Italia, Foglio 075, "Como", Progetto CARG, p. 206.

http://www.isprambiente.gov.it/Media/carg/note_i llustrative/75_Como.pdf

Nappo, N., Ferrario, M.F., Livio, F., Michetti, A.M., 2020. Regression Analysis of Subsidence in the Como Basin (Northern Italy): New Insights on Natural and Anthropic Drivers from InSAR Data. Remote Sens. 12, 2931. https://doi.org/10.3390/rs12182931

Nappo, N., Peduto, D., Polcari, M., Livio, F., Ferrario, M.F., Comerci, V., Stramondo, S., Michetti, A.M., 2021a. Subsidence in Como historic centre (northern Italy): assessment of building vulnerability combining hydrogeological and stratigraphic features, Cosmo-SkyMed InSAR and damage data. Int. J. Disaster Risk Reduct. 56, 102115. https://doi.org/10.1016/j.ijdrr.2021.102115

Nelder, J.A.; Wedderburn, R.W.M., 1972. Generalized Linear Models. J. R. Stat. Soc. Ser. A 1972, 135, 370–384.

Peduto, D., Cascini, L., Arena, L., Ferlisi, S., Fornaro, G., Reale, D., 2015. A general framework and related procedures for multiscale analyses of DInSAR data in subsiding urban areas. ISPRS J. Photogramm. Remote Sens. 105, 186–210. https://doi.org/10.1016/j.isprsjprs.2015.04.001

Peduto, D., Nicodemo, G., Maccabiani, J., Ferlisi, S., 2017c. Multi-scale analysis of settlement-induced building damage using damage surveys and DInSAR data: A case study in The Netherlands. Eng. Geol. 218, 117–133. https://doi.org/10.1016/j.enggeo.2016.12.018

Peduto, D., Korff, M., Nicodemo, G., Marchese, A., Ferlisi, S., 2019. Empirical fragility curves for settlement-affected buildings: Analysis of different intensity parameters for seven hundred masonry buildings in The Netherlands. Soils Found. 59, 380–397. https://doi.org/10.1016/j.sandf.2018.12.009

Polcari, M., 2019. Anthropogenic subsidence along railway and road infrastructures in Northern Italy highlighted by Cosmo-SkyMed satellite data. J. Appl. Remote Sens. 13, 1. https://doi.org/10.1117/1.jrs.13.024515

Rossi, S., Alberti, F., Felber, M., Bini, A., 1991. Evidenze di fluttuazioni glaciali würmiane nella Bassa valle della Breggia (Cernobbio, Como), Boll. Soc. Ticin. Sci. Nat. LXXIX, 25–47.

Sileo, G., Giardina, F., Livio, F., Michetti, A.M., Mueller, K., Vittori, E., 2007. Remarks on the quaternary tectonics of the Insubria region (lombardia north western Italy, and ticino, south eastern swizerland), Boll. Soc. Geol. It. - Italian Journal of Geoscience 126 (2), 411–425, 0037-8763.

SIT, 2021. URL https://www.comune.como.it/it/servizi/urbanisti ca/sit/ - Last access: September 2021.

Stramondo, S., Bozzano, F., Marra, F., Wegmuller, U., Cinti, F.R., Moro, M., Saroli, M., 2008. Subsidence induced by urbanisation in the city of Rome detected by advanced InSAR technique and geotechnical investigations. Remote Sens. Environ. 112, 3160–3172. https://doi.org/10.1016/j.rse.2008.03.008

Uboldi, M., 1993. Carta archeologica della Lombardia, in: Franco Cosimo Panini, Como. La città murata e la convalle.

Wackernagel, H., 1995. Ordinary kriging, in: Multivariate Geostatistics, Springer, Berlin/ Heidelberg, Germany, pp. 74–81.

Wegmuller, U., Werner, C., 1997. Gamma SAR processor and interferometry software, in: Proceedings of the ERS Symposium on Space at the Service of Our Environment, 1997, pp. 1687–1692. Florence, Italy, 14–21 March 1997; ESA Publications Division: Florence, Italy.

Werner, C., Wegmüller, U., Strozzi, T., Wiesmann, A., 2003. Interferometric Point Target Analysis for Deformation Mapping, in: International Geoscience and Remote Sensing Symposium (IGARSS). pp. 4362–4364. https://doi.org/10.1109/igarss.2003.1295516

Wood, S.N., 2010. Fast stable restricted maximum likelihood and marginal likelihood estimation of semiparametric generalized linear models. J. R. Stat. Soc. Ser. B (Stat. Methodol.) 2010, 73, 3–36.

Zhang, L., Ng, A.M.Y., 2005. Probabilistic limiting tolerable displacements for serviceability limit state design of foundations. Geotechnique 55, 151–161. https://doi.org/10.1680/geot.2005.55.2.151

## *Chapter 4 – UAV for road damage assessment in landslide areas: the Province of Como (N Italy)*

ANAS, 2004. I Quaderni tecnici per la salvaguardia delle infrastrutture V.

Bertotti, G., Siletto, G.B., Spalla, M.I., 1993. Deformation and metamorphism associated with crustal rifting: The

Permian to Liassic evolution of the Lake Lugano-Lake Como area (Southern Alps). Tectonophysics. https://doi.org/10.1016/0040-1951(93)90122-Z

Bini, A., 1996. La regolazione del Lago di Como: problemi e proposte. Atti del convegno. Villa Olmo, Como, 19 April 1996, Kiwanis International Europe.

Canny, J., 1986. A Computational Approach to Edge Detection. IEEE Trans. Pattern Anal. Mach. Intell. PAMI-8, 679–698. https://doi.org/10.1109/TPAMI.1986.4767851

Comune di Vercana, 2021. URL http://www.hlservizicloud.it/pgt/content/013239 - Last access: September 2021.

Cruden, D., Varnes, D., 1996. Landslides: Investigation and Mitigation. Chapter 3 - Landslide Types and Processes. Transp. Res. Board Spec. Rep.

Cubero-Fernandez, A., Rodriguez-Lozano, F.J., Villatoro, R., Olivares, J., Palomares, J.M., 2017. Efficient pavement crack detection and classification. Eurasip J. Image Video Process. 2017. https://doi.org/10.1186/s13640-017-0187-0

Douglas, D.H., Peucker, T.K., 1973. Algorithms for the reduction of the number of points required to represent a digitized line or its caricature. Cartogr. Int. J. Geogr. Inf. Geovisualization 10, 112–122. https://doi.org/10.3138/fm57-6770-u75u-7727

Geoportale Regione Lombardia, 2021. URL http://www.geoportale.regione.lombardia.it/ - Last acces: September 2021.

Hackel, T., Wegner, J.D., Schindler, K., 2016. Contour detection in unstructured 3D point clouds, in: Proceedings of the IEEE Computer Society Conference on Computer Vision and Pattern Recognition. pp. 1610–1618. https://doi.org/10.1109/CVPR.2016.178

Hatmoko, J.U.D., Setiadji, B.H., Wibowo, M.A., 2019. Investigating causal factors of road damage: a case study. MATEC Web Conf. 258, 02007. https://doi.org/10.1051/matecconf/201925802007

ISPRA, 2021. URL https://idrogeo.isprambiente.it/app/ - Last acces: September 2021.

Kumar, P., Lewis, P., Mcelhinney, C.P., Rahman, A.A., 2015. An algorithm for automated estimation of road roughness from mobile laser scanning data. Photogramm. Rec. 30, 30–45. https://doi.org/10.1111/phor.12090

Laubscher, H.P., 1985. Large-scale, thin-skinned thrusting in the southern Alps: Kinematic models. Bull. Geol. Soc. Am. https://doi.org/10.1130/0016-7606(1985) 96<710:LTTITS>2.0.CO;2

Maas, H.G., Vosselman, G., 1999. Two algorithms for extracting building models from raw laser altimetry data. ISPRS J. Photogramm. Remote Sens. 54, 153–163. https://doi.org/10.1016/S0924-2716(99)00004-0

Martin, S., Gambillara, R., Centurini, A., Terrana, S., Mazzucotelli, M., Figaroli, M., Polledrotti, I., 2004. Aggiornamento carta dei dissesti – Relazione finale. Convenzione tra la Provincia di Como e l'Universit`a degli Studi dell'Insubria per la realizzazione di attivit`a didattiche e di ricerca riguardanti l'assetto idrogeologico ed ambientale del territorio della Provincia di Como (Delibera n.345, n.58163 di protocollo del 23-12-2004) (Coordinatore scientifico).

Mavrouli, O., Corominas, J., Ibarbia, I., Alonso, N., Jugo, I., Ruiz, J., Luzuriaga, S., Navarro, J.A., 2019. Integrated risk assessment due to slope instabilities in the roadway network of Gipuzkoa, Basque Country. Nat. Hazards Earth Syst. Sci. 19, 399–419. https://doi.org/10.5194/nhess-19-399-2019

Michetti, A.M., 2014a. Como 075 Sheet of the Geological Map of Italy, 1:50.000 scale, Progetto Cartografia Geologica - CARG Project, ISPRA Servizio Geologico d'Italia. http://www.isprambiente.gov.it/Media/carg/75_COMO/Foglio.html

Michetti, A.M., Livio, F., Pasquarè, F.A., Vezzoli, L., Bini, A., Bernoulli, D., Sciunnach, D., 2014b. Note Illustrative Della Carta Geologica d'Italia, Foglio 075, "Como", Progetto CARG, p. 206. http://www.isprambiente.gov.it/Media/carg/note_i llustrative/75_Como.pdf

Nangeroni, G., 1969. Note geomorfologiche sui monti a occidente del Lario comasco. In: Atti Soc. It. Sc. Nat. e Museo Civ. St. Nat. Milano – 109/02: 97–184, 15-VI-1969.

Nappo, N., Mavrouli, O., Nex, F., van Westen, C., Gambillara, R., Michetti, A.M., 2021b. Use of UAV-based photogrammetry products for semi-automatic detection and classification of asphalt road damage in landslide-affected areas. Eng. Geol. 294, 106363. https://doi.org/10.1016/j.enggeo.2021.106363

Nappo, N., Peduto, D., Mavrouli, O., van Westen, C.J., Gullà, G., 2019. Slow-moving landslides interacting with the road network: Analysis of damage using ancillary data, in situ surveys and multi-source monitoring data.

Eng. Geol. 260, 105244. https://doi.org/10.1016/j.enggeo.2019.105244

Nex, F., Remondino, F., 2014. UAV for 3D mapping applications: A review. Appl. Geomatics. https://doi.org/10.1007/s12518-013-0120-x

Niemeyer, J., Mallet, C., Rottensteiner, F., Sörgel, U., 2012. Conditional random fields for the classification of lidar point clouds. ISPRS - Int. Arch. Photogramm. Remote Sens. Spat. Inf. Sci. XXXVIII-4/, 209–214. https://doi.org/10.5194/isprsarchives-xxxviii-4-w19-209-2011

Pracchi, R., 1954. Il quaternario nel Lario occidentale. Attit. Soc. It. Sci. Nat. XCIII, 111–178.

Ramer, U., 1972. An iterative procedure for the polygonal approximation of plane curves. Comput. Graph. Image Process. 1, 244–256. https://doi.org/10.1016/S0146-664X(72)80017-0

Servizio Geologico d'Italia ISPRA, 2021. URL http://sgi2.isprambiente.it/mapviewer/ - Last acces: September 2021.

Weinmann, M., Jutzi, B., Mallet, C., 2013. Feature relevance assessment for the semantic interpretation of 3D point cloud data. ISPRS Ann. Photogramm. Remote Sens. Spat. Inf. Sci. 2, 313–318. https://doi.org/10.5194/isprsannals-II-5-W2-313-2013

Yu, J., Chou, E.Y.J., Yau, J.T., 2006. Development of speed-related ride quality thresholds using international roughness index, in: Transportation Research Record. pp. 47–53. https://doi.org/10.3141/1974-08

## *Chapter 5 – Challenges in monitoring constructions in vulnerable areas*

Bozzano, F., Andreucci, A., Gaeta, M., Salucci, R., 2000. A geological model of the buried Tiber River valley beneath the historical centre of Rome. Bull. Eng. Geol. Env. 2000, p. 59:1-2

Bozzano, F., Caserta, A., Govoni, A., Marra, F., Martino, S., 2008. Static and dynamic characterization of alluvial deposits in the Tiber River Valley: New data for assessing potential ground motion in the City of Rome, JOURNAL OF GEOPHYSICAL RESEARCH, VOL. 113, B01303, doi:10.1029/2006JB004873

Di Carlo, F., Miano, A., Giannetti, I., Mele, A., Bonano, M., Lanari, R., Meda, A., Prota, A., 2021. On the integration of multi-temporal synthetic aperture radar interferometry products and historical surveys data for buildings structural monitoring. J. Civ. Struct. Heal. Monit. https://doi.org/10.1007/s13349-021-00518-4

DPC-ReLUIS, 2021. URL https://www.reluis.it/it/ - Last access: September 2021.

Ezquerro, P., Del Soldato, M., Solari, L., Tomás, R., Raspini, F., Ceccatelli, M., Fernández-Merodo, J.A., Casagli, N., Herrera, G., 2020. Vulnerability Assessment of Buildings due to Land Subsidence using InSAR Data in the Ancient Historical City of Pistoia (Italy). Sensors 20, 2749. https://doi.org/10.3390/s20102749

Funiciello, R., Giordano, G., 2008. La nuova Carta Geologica di Roma: litostratigrafia e organizzazione stratigrafica. In Funiciello, R. Praturlon, A., Giornado, G. (Ed), Memorie descrittive della Carta Geologica d'Italia, vol. 80/2008; Firenze: B.E.L.C.A. editore

Geoportal Nazionale, 2021. URL http://www.pcn.minambiente.it/mattm/ - Last access: September 2021.

Hanssen, R.F., 2001. Radar Interferometry: Data Interpretation and Error Analysis. In Number v. 2 in Remote Sensing and Digital Image Processing; Kluwer Academic: Dordrecht, The Netherlands; Boston, MA, USA, 2001.

Loli, M., Chatzidaki, A., Vamvatsikos, D., Gazetas, G., 2020. Seismic vulnerability of motorway bridge on active landslide. 17th World Conf. Earthq. Eng. 17WCEE.

Luberti, G.M., Marra, F., Florindo, F., 2017. A review of the stratigraphy of Rome (Italy) according to geocronologically and paleomagnetically constrained aggradational successions, glacioeustatic forcing and volcano-tectonic processes. Quaternary International, n°438(B), p. 40-67.

Marra, F., Rosa, C., 1995. Stratigrafia e assetto geologico dell'area romana. In Funiciello R. (Ed), La geologia di Roma. Il centro storico di Roma, Memorie descrittive della Carta Geologica d'Italia, n°50/1995, p. 49-118

Milli, S., Mancini, M., Moscatelli, M., Stigliano, F., Marini, M., Cavinato, G., 2016. From river to shelf, anatomy of a high-frequency depositional sequence: The Late Pleistocene to Holocene Tiber depositional sequence. Sedimentology © 2016 International Association of Sedimentologists, doi: 10.1111/sed.12277, p. 1-44

Montazeri, S., González, F.R., Zhu, X.X., 2018. Geocoding error correction for InSAR point clouds. Remote Sens. 10, 1–22. https://doi.org/10.3390/rs10101523

Nappo, N., Ferrario, M.F., Livio, F., Michetti, A.M., 2020. Regression Analysis of Subsidence in the Como Basin (Northern Italy): New Insights on Natural and Anthropic Drivers from InSAR Data. Remote Sens. 12, 2931. https://doi.org/10.3390/rs12182931

Nappo, N., Peduto, D., Polcari, M., Livio, F., Ferrario, M.F., Comerci, V., Stramondo, S., Michetti, A.M., 2021a. Subsidence in Como historic centre (northern Italy): assessment of building vulnerability combining hydrogeological and stratigraphic features, Cosmo-SkyMed InSAR and damage data. Int. J. Disaster Risk Reduct. 56, 102115. https://doi.org/10.1016/j.ijdrr.2021.102115

Nappo, N., Mavrouli, O., Nex, F., van Westen, C., Gambillara, R., Michetti, A.M., 2021b. Use of UAV-based photogrammetry products for semi-automatic detection and classification of asphalt road damage in landslide-affected areas. Eng. Geol. 294, 106363. https://doi.org/10.1016/j.enggeo.2021.106363

Parotto, M., 2008. Evoluzione paleogeografica dell'area romana: una breve sintesi. In Funiciello, R. Praturlon A., Giornado G. (Ed), Memorie descrittive della Carta Geologica d'Italia, vol. 80/2008; Firenze: B.E.L.C.A. editore, p. 25-38.

Peduto, D., Cascini, L., Arena, L., Ferlisi, S., Fornaro, G., Reale, D., 2015. A general framework and related procedures for multiscale analyses of DInSAR data in subsiding urban areas. ISPRS J. Photogramm. Remote Sens. 105, 186–210. https://doi.org/10.1016/j.isprsjprs.2015.04.001

Peduto, D., Nicodemo, G., Maccabiani, J., Ferlisi, S., 2017c. Multi-scale analysis of settlement-induced building damage using damage surveys and DInSAR data: A case study in The Netherlands. Eng. Geol. 218, 117–133. https://doi.org/10.1016/j.enggeo.2016.12.018

UNDRR, 2021. URL https://www.undrr.org/implementing-sendai-framework/what-sendai-framework - Last access: September 2021.

Ventriglia, U., 2002. Geologia del territorio del Comune di Roma. Roma, Cerbone editore

Zhang, L., Ng, A.M.Y., 2005. Probabilistic limiting tolerable displacements for serviceability limit state design of foundations. Geotechnique 55, 151–161. https://doi.org/10.1680/geot.2005.55.2.151

## *Chapter 6 – Conclusions*

Burland, J.B., Broms, B.B., De Mello, V.F.B., 1977. Behaviour of Foundations and Structures Comportement des Fondations et des Structures. State Art Rep. 363–400.

Canny, J., 1986. A Computational Approach to Edge Detection. IEEE Trans. Pattern Anal. Mach. Intell. PAMI-8, 679–698. https://doi.org/10.1109/TPAMI.1986.4767851

Cigna, F., Del Ventisette, C., Liguori, V., Casagli, N., 2011. Advanced radar-interpretation of InSAR time series for mapping and characterization of geological processes. Nat. Hazards Earth Syst. Sci. 11, 865–881. https://doi.org/10.5194/nhess-11-865-2011

Comerci, V., Capelletti, S., Michetti, A.M., Rossi, S., Serva, L., Vittori, E., 2007. Land subsidence and Late Glacial environmental evolution of the Como urban area (Northern Italy). Quat. Int. 173–174, 67–86. https://doi.org/10.1016/j.quaint.2007.06.014

Cubero-Fernandez, A., Rodriguez-Lozano, F.J., Villatoro, R., Olivares, J., Palomares, J.M., 2017. Efficient pavement crack detection and classification. Eurasip J. Image Video Process. 2017. https://doi.org/10.1186/s13640-017-0187-0

Del Ventisette, C., Ciampalini, A., Manunta, M., Calò, F., Paglia, L., Ardizzone, F., Mondini, A.C., Reichenbach, P., Mateos, R.M., Bianchini, S., Garcia, I., Füsi, B., Deák, Z.V., Rádi, K., Graniczny, M., Kowalski, Z., Piatkowska, A., Przylucka, M., Retzo, H., Strozzi, T., Colombo, D., Mora, O., Sánchez, F., Herrera, G., Moretti, S., Casagli, N., Guzzetti, F., 2013. Exploitation of large archives of ERS and ENVISAT C-band SAR data to characterize ground deformations. Remote Sens. 5, 3896–3917. https://doi.org/10.3390/rs5083896

ENAC, 2021. URL https://www.enac.gov.it/sicurezza-aerea/droni - Last access: September 2021.

Ferlisi, S., Marchese, A., Peduto, D., 2020a. Quantitative analysis of the risk to road networks exposed to slow-moving landslides: a case study in the Campania region (southern Italy). Landslides 2020. https://doi.org/10.1007/s10346-020-01482-8

Ferrario, M.F., Bonadeo, L., Brunamonte, F., Livio, F., Martinelli, E., Michetti, A.M., Censi Neri, P., Chiessi, V., Comerci, V., Höbig, N., 2015a. Late Quaternary environmental evolution of the Como urban area (Northern Italy): A multidisciplinary tool for risk management and urban planning. Eng. Geol. 193, 384–401. https://doi.org/10.1016/j.enggeo.2015.05.013

ICAO, 2021. URL https://www.icao.int/Pages/default.aspx - Last access: September 2021.

Kim, S.-W., Wdowinski, S., Dixon, T.H., Amelung, F., Kim, J.W., Won, J.-S., 2010. Measurements and predictions of subsidence induced by soil consolidation using persistent scatterer InSAR and a hyperbolic model. Geophys. Res. Lett. 37, n/a-n/a. https://doi.org/10.1029/2009GL041644

Livio, F., Berlusconi, A., Chunga, K., Michetti, A.M., Sileo, G., 2011. New stratigraphic and structural evidence for Late Pleistocene surface faulting along the Monte Olimpino Backthrust (Lombardia, N Italy). Rend. Online Soc. Geol. Ital. 14, 17–25. https://doi.org/10.3301/ROL.2011.03

Michetti, A.M., 2014a. Como 075 Sheet of the Geological Map of Italy, 1:50.000 scale, Progetto Cartografia Geologica - CARG Project, ISPRA Servizio Geologico d'Italia. http://www.isprambiente.gov.it/Media/carg/75_COMO/Foglio.html

Michetti, A.M., Livio, F., Pasquarè, F.A., Vezzoli, L., Bini, A., Bernoulli, D., Sciunnach, D., 2014b. Note Illustrative Della Carta Geologica d'Italia, Foglio 075, "Como", Progetto CARG, p. 206. http://www.isprambiente.gov.it/Media/carg/note_i llustrative/75_Como.pdf

Nappo, N., Ferrario, M.F., Livio, F., Michetti, A.M., 2020. Regression Analysis of Subsidence in the Como Basin (Northern Italy): New Insights on Natural and Anthropic Drivers from InSAR Data. Remote Sens. 12, 2931. https://doi.org/10.3390/rs12182931

Nappo, N., Mavrouli, O., Nex, F., van Westen, C., Gambillara, R., Michetti, A.M., 2021b. Use of UAV-based photogrammetry products for semi-automatic detection and classification of asphalt road damage in landslide-affected areas. Eng. Geol. 294, 106363. https://doi.org/10.1016/j.enggeo.2021.106363

Nappo, N., Peduto, D., Mavrouli, O., van Westen, C.J., Gullà, G., 2019. Slow-moving landslides interacting with the road network: Analysis of damage using ancillary data, in situ surveys and multi-source monitoring data. Eng. Geol. 260, 105244. https://doi.org/10.1016/j.enggeo.2019.105244

Nappo, N., Peduto, D., Polcari, M., Livio, F., Ferrario, M.F., Comerci, V., Stramondo, S., Michetti, A.M., 2021a. Subsidence in Como historic centre (northern Italy): assessment of building vulnerability combining hydrogeological and stratigraphic features, Cosmo-SkyMed InSAR and damage data. Int. J. Disaster Risk Reduct. 56, 102115. https://doi.org/10.1016/j.ijdrr.2021.102115

Peduto, D., Cascini, L., Arena, L., Ferlisi, S., Fornaro, G., Reale, D., 2015. A general framework and related procedures for multiscale analyses of DInSAR data in subsiding urban areas. ISPRS J. Photogramm. Remote Sens. 105, 186–210. https://doi.org/10.1016/j.isprsjprs.2015.04.001

Peduto, D., Korff, M., Nicodemo, G., Marchese, A., Ferlisi, S., 2019. Empirical fragility curves for settlement-affected buildings: Analysis of different intensity parameters for seven hundred masonry buildings in The Netherlands. Soils Found. 59, 380–397. https://doi.org/10.1016/j.sandf.2018.12.009

Peduto, D., Nicodemo, G., Maccabiani, J., Ferlisi, S., 2017c. Multi-scale analysis of settlement-induced building damage using damage surveys and DInSAR data: A case study in The Netherlands. Eng. Geol. 218, 117–133. https://doi.org/10.1016/j.enggeo.2016.12.018

Sileo, G., Giardina, F., Livio, F., Michetti, A.M., Mueller, K., Vittori, E., 2007. Remarks on the quaternary tectonics of the Insubria region (Lombardia north western Italy, and Ticino, south eastern Switzerland), Boll. Soc. Geol. It. - Italian Journal of Geoscience 126 (2), 411–425, 0037-8763.

Zhang, L., Ng, A.M.Y., 2005. Probabilistic limiting tolerable displacements for serviceability limit state design of foundations. Geotechnique 55, 151–161. https://doi.org/10.1680/geot.2005.55.2.151

# Acknowledgments

At the beginning of my journey, I dreamed to emerge as a scientist and hoped to achieve my objectives. Today, I can say that those dreams and hopes came true. And I wish to thank numerous people for encouraging and supporting me in various ways.

Foremost, I want to thank my supervisor Prof. Alessandro Maria Michetti for giving me a chance after countless rejections. Instead of being an issue, our different backgrounds became the strength of our collaboration. After all, a rock can be more than only a doorstopper!

My sincere gratitude goes to Dr. Olga Mavrouli for supervising my work in these years. The guidance and support that she gave me go beyond what I expected. "*It seems interesting but are you sure that you can do it?*" was her first comment to my proposal. For me, this was particularly motivating. Simply, thanks.

In addition to my supervisors, I wish to acknowledge my co-authors for the excellent work done together, as demonstrated by our publications. Thanks to Franz Livio and Maria Francesca Ferrario (University of Insubria) for both papers investigating the subsidence in the city of Como; Dario Peduto (University of Salerno), Marco Polcari (Istituto Nazionale di Geofisica e Vulcanologia), Valerio Comerci (Servizio Geologico d'Italia) and Salvatore Stramondo (INGV) for the investigations in the Como historic centre; Francesco Nex and Cees van Westen (University of Twente) and Roberto Gambillara (University of Insubria) for the extraordinary work on road damage detection in landslide areas.

Thanks to Prof. Norman Kerle (University of Twente) for involving me in the Horizon 2020 PANOPTIS Project (WP5), and Prof. Francesca Bozzano for involving me in the DPC-ReLUIS 2019-2021 Project (WP6).

I wish to thank my colleagues and friends and the whole ESA department from the University of Twente. Thanks to Jonathan, Zahedeh, Linda, Azin, Fiorenza, Biao, Nan, Sofia, Evelin,

Oscar, Fardad, Lina, Saman, Soban, Kartika, Yacob and Tingxuan for the funniest coffee breaks and dinners (before the COVID-19 pandemic) and the most enjoyable working days.

Thanks to Sergio, Carlos, Julia, Luis, Luiza, Paloma, Alejandro, Alejandra, Flavia, Javier and many more friends for the best parties and memories of Enschede. The time spent in The Netherlands with all of them was amazing despite the COVID-19 pandemic.

Special thanks go to Rafita who chose to be by my side and share this part of our lives. He tenderly supported and encouraged me (almost) every step of the way. The joy that he gives me is irreplaceable. And I could not wish for anything better.

Thanks to my parents and my sister Annalisa for supporting my decisions, both professional and personal. My grandparents and Vega are not here anymore, but I am sure they can see where I am today.

Last but not least, I wish to thank also myself, the most difficult person to live with.

Sincerely, *thanks*.